Mountain Wave Impact on Flight Conditions of High-Flying Aircraft

Martina Bramberger

München 2019

Mountain Wave Impact on Flight Conditions of High-Flying Aircraft

Martina Bramberger

Dissertation
an der Fakultät für Physik
der Ludwig–Maximilians–Universität
München

vorgelegt von
Martina Bramberger
aus Fürstenfeldbruck

München, den 25. Januar 2019

Erstgutachter: Prof. Dr. Markus Rapp
Zweitgutachter: Prof. Dr. Franz-Josef Lübken
Tag der mündlichen Prüfung: 20.05.2019

Das Leben ist bezaubernd. Man muss es nur durch die richtige Brille sehen.

—Alexandre Dumas
(1802-1870)

Zusammenfassung

Seitdem Segelflieger Gebirgswellen entdeckt haben, sind diese ein wohl-bekanntes Phänomen der Atmosphäre, weil sie die atmosphärische Strömung auf relativ kurzen horizontalen Skalen ($\lambda_h \approx 20\,\mathrm{km}$) maßgeblich beeinflussen. Das Ziel dieser Arbeit ist es, den Einfluss von Gebirgswellen auf hochfliegende Flugzeuge zu untersuchen(Fluglevel (FL) > 20000 ft (= FL200)). Deshalb werden zwei Fälle untersucht, in welchen Gebirgswellen den Flugzustand des Forschungsflugzeuges HALO (High Altitude LOng Range Research Aircraft) auf verschiedene Art beeinflussten.

In der ersten Fallstudie werden unerwartete Warnungen vor Strömungsabriss (stall) untersucht, welche während eines Forschungsfluges von HALO am 12. Januar 2016 in 12.5 km Höhe (FL410) über Italien auftraten. Am Ort des Zwischenfalls war die Stratosphäre geprägt von großen horizontalen Variationen in der Temperatur und der Komponente des Horizontalwindes entlang des Flugzeuges. An diesem Tag begünstigte die atmosphärische Grundströmung die Anregung und Ausbreitung von Gebirgswellen an und über den Apenninen, Italien. Diese Gebirgswellen hatten große vertikale Energieflüsse von $8\,\mathrm{W\,m^{-2}}$ und breiteten sich ohne nenneswerte Dissipation von der Troposphäre bis in die Stratosphäre aus.

In der zweiten Fallstudie trat starke Turbulenz bei einem Forschungsflug von HALO am 13. Oktober 2016 über Island auf. Bei diesem Ereignis erfuhr das Forschungsflugzeug Höhenänderungen von ca 50 m innerhalb von ca 15 s. Zusätzlich konnte die automatische Schubkontrolle von HALO die großen Gradienten im Horizontalwind nicht ausregeln, weshalb der Pilot dieses System abschalten musste. An diesem Tag breiteten sich die angeregten Gebirgswellen vertikal über Island aus. Im Höhenbereich des Turbulenzereignisses war die Atmosphäre durch eine starke negative Vertikalscherung des Horizontalwindes geprägt, welche das Brechen von Wellen begünstigt. Messungen und Simulationen von EULAG (Eulerian semi-Lagrangian fluid solver) legen nahe, dass HALO durch das Zentrum eines Wellenbrechungsgebietes flog.

Durch die Analyse von hoch aufgelösten in situ Messungen und Aufzeichnungen des 'Quick Access Recorder' ("Blackbox") von HALO konnte der Horizontalwind als maßgeblicher atmosphärischer Einfluss auf die Geschwindigkeit von hochfliegenden Flugzeugen für diesen Fall identifiziert werden. Desweiteren wurde herausgefunden, dass vertikal propagierende Gebirgswellen den Flugzustand eines hoch fliegenden Flugzeuges beeinflussen. Während Turbulenz eine anerkannte Gefahr für den Luftverkehr ist, zeigen die Fallstudien, dass nicht brechende, sich vertikal ausbreitende Gebirgswellen auch eine Gefahr darstellen, indem sie das Horizontalwindfeld auf Skalen modulieren, die durch das Avioniksystem nicht schnell genug ausgeregelt werden können. Dies kann auf der einen Seite zu einer Reduktion der Flugzeuggeschwindigkeit zu den minimal nötigen Geschwindigkeiten führen, um Strömungsabriss zu vermeiden oder auf der anderen Seite zu Variationen in der Flugzeuggeschwindigkeit, welche durch die automatische Schubkontrolle nicht ausgeregelt werden können.

Desweiteren werden in situ Messungen zu operationellen Analysen und Vorhersagen

des integrierten Vorhersagesystems (IFS) des europäischen Zentrums für mittelfristige Wettervorhersage (EZMW) verglichen. Dieser Vergleich zeigt, dass großskalige Strukturen sehr gut vorhergesagt wurden. Allerdings wurden die beobachteten Amplituden von Strukturen auf Skalen $< 5\,\mathrm{km}$ in allen meteorologischen Parametern unterschätzt. Die Anwendung des graphischen Turbulenz Guiding System (GTG) stellt eine Bereicherung dar, weil der Ort und die Stärke der maximal beobachteten Turbulenz korrekt vorhergesagt wurde. Allerdings konnte die beobachtete Intermittenz nicht reproduziert werden und es wurde eine klare Tendenz zur Überschätzung der Turbulenzstärke gefunden.

Abstract

Ever since their discovery by glider pilots, mountain waves (MWs) are a well known atmospheric process to affect aviation as they can significantly modulate the atmospheric flow field on relatively short scales ($\lambda_h \approx 20\,\mathrm{km}$). The goal of this thesis is to study the impact of such a flow field on high-flying aircraft (i.e. flight level (FL) $> 20.000\,\mathrm{ft} =$ FL200). For that reason, two cases were studied exemplarily where MWs affected flying conditions of the High Altitude LOng Range Research Aircraft, HALO in different ways.

In the first case stall warnings at FL 410 (12.5 km) occurred unexpectedly during a research flight of HALO over Italy on 12 January 2016. At the incident location, the stratosphere was characterized by large horizontal variations in the along-track wind speed and temperature. On this day, the general atmospheric circulation favored the excitation and vertical propagation of large-amplitude mountain waves at and above the Apennines, Italy. These mountain waves had achieved large vertical energy fluxes of $8\,\mathrm{W\,m^{-2}}$ and propagated without significant dissipation from the troposphere into the stratosphere.

Strong turbulence was encountered by HALO at FL 430 (13.8 km) on 13 October 2016 above Iceland which constitutes the second case study. In this event the turbulence caused altitude changes of about 50 m within about 15 s of the research aircraft. Additionally, the automatic thrust control of HALO could not control the large gradients in the horizontal wind speed and, consequently, the pilot had to deactivate this system. On that day, MWs were excited and propagated vertically above Iceland. In the altitude region of the turbulence encounter the atmosphere was characterized by a pronounced negative vertical shear of the horizontal wind. Here, in situ observations together with simulations of the Eulerian semi-Lagrangian fluid solver (EULAG) suggest that HALO was flying through the center of a breaking MW field.

First, the question whether aircraft speed is dominantly influenced by the temperature or the horizontal wind could be answered. Analysis of high-resolution in situ observations and recordings of HALO's Quick Access Recorder ('blackbox') suggests that it is the horizontal wind speed which dominantly impacts aircraft speed of high flying aircraft. Second, it was found that vertically propagating MWs can affect flight conditions of high-flying aircraft. While turbulence is a well-acknowledged hazard to aviation, the case studies reveal that non-breaking, vertically propagating mountain waves also pose a potential hazard by modulating the ambient along-track wind speed on scales for which the response time of the avionic system is too slow. This may lead on the one hand to a decrease of the aircraft speed towards the minimum needed stall speed or on the other hand to variations in the aircraft speed that cannot be controlled by the automatic thrust control.

Furthermore, in situ observations are compared to European Centre for Medium-Range Weather Forecasts (ECMWF) Integrated Forecast System (IFS) forecasts and operational analyses. This comparison revealed that large-scale structures are

predicted very well. However, on scales smaller than 5 km observed amplitudes of all meteorological parameters are underestimated. Here, the application of the Graphical Turbulence Guidance Tool (GTG) proved to be valuable for predicting the correct magnitude and location of the maximum encountered turbulence above Iceland. However, the observed intermittency could not be reproduced and a tendency to overpredict turbulence was found.

Publications

Parts of the introduction, methods and results presented in this thesis have been published in the following article:

M. Bramberger, A. Dörnbrack, H. Wilms, S. Gemsa, K. Raynor and R. Sharman, 2018:. Vertically Propagating Mountain Waves - A Hazard for High-Flying Aircraft?. *J. Appl. Meteor. Climatol.*, **57**, 1957-1975,doi:10.1175/JAMC-D-17-0340.1.

M.Bramberger conducted the analyses and wrote the paper, A. Dörnbrack supervised the work and provided ECMWF IFS operational analyses and forecasts, H. Wilms provided 3D EULAG simulations, S. Gemsa flew the aircraft and provided insight to Aerodynamics, K. Raynor provided QAR data and R. Sharman provided the GTG.

Contents

1 Introduction

1.1 Atmospheric impacts on high-flying aircraft

Tropospheric weather strongly influences aviation in different ways. At ground, high temperatures limit the take-off weights of airplanes (Coffel and Horton 2015). Thunderstorms together with lightning strikes can cause disruptions and delays in the operation of airports (Romps et al. 2014).

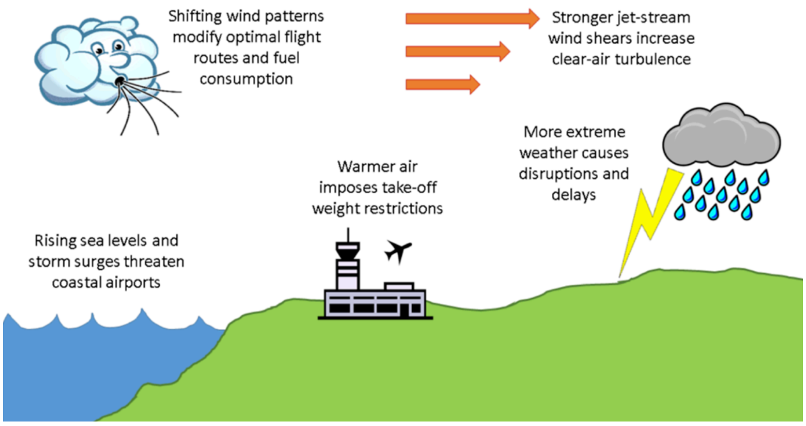

Figure 1.1: Schematic summarizing atmospheric impacts on aviation (Puempel and Williams 2016).

In the upper troposphere and lower stratosphere where most commercial aircraft fly, shifting wind patterns may modify optimal flight routes which in turn affect travel times (Karnauskas et al. 2015, Irvine et al. 2016, Kim et al. 2016, Williams 2016). Moreover, at these altitudes atmospheric turbulence is the major reason for injuries to passengers and crew (Sharman et al. 2012b, Tvaryanas 2003). In particular, unpredicted turbulence outside clouds can be hazardous as it is neither visible to pilots nor detectable by standard on-board radars (Sharman et al. 2012b). This kind of turbulence that is not connected to clouds and thunderstorms is referred to as Clear Air Turbulence (CAT).

Well-known generation processes of turbulence affecting aircraft at cruising altitudes comprise thunderstorms, strong wind shears related to upper-level fronts and jet streams, unbalanced flow, and breaking mountain waves (MWs) (e.g. Vinnichenko et al. 1980, Lester 1994, Wolff and Sharman 2008, Lane et al. 2012, Sharman et al. 2012b). Considering the generation process, turbulence directly related to breaking mountain waves is referred to as Mountain Wave Turbulence (MWT) (Sharman et al. 2012b).

Apart from clouds and the vicinity of thunderstorms, Wolff and Sharman (2008) identified regions susceptible to turbulence over the United States. Preferred areas for turbulence occurrence are complex terrains such as the Rocky Mountains where the source of turbulence could be attributed to mountain wave breaking. Other regions posing wave-induced hazards to aviation include e.g. the Alps (e.g. Jiang and Doyle 2004) and Greenland (e.g. Doyle et al. 2005, Ólafsson and Ágústsson 2009, Lane et al. 2009, Sharman et al. 2012a). Greenland is of particular importance as it is located underneath the highly frequented North Atlantic flight tracks connecting Europe and North America.

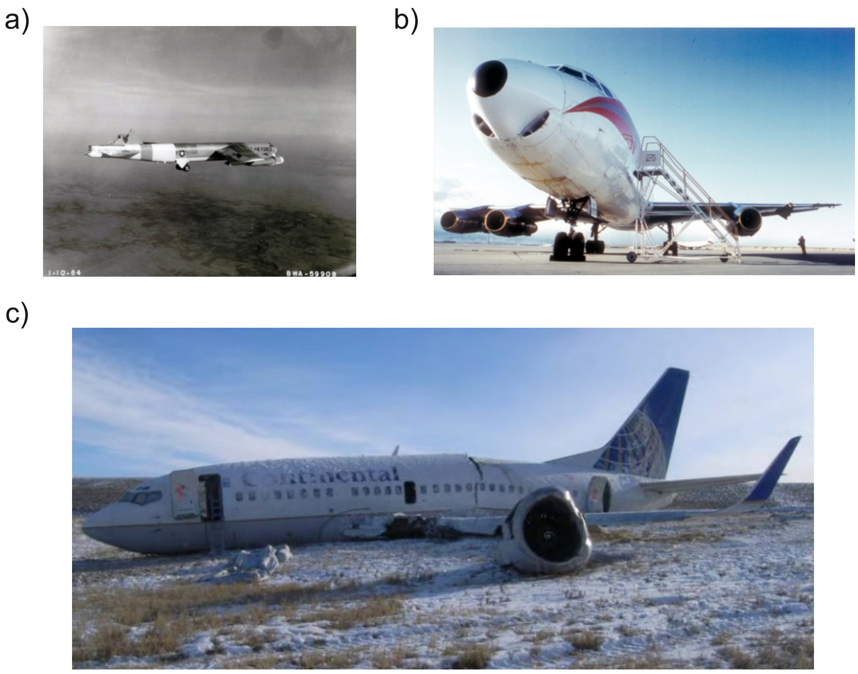

Figure 1.2: Examples on the effect of MWs on aircraft structure. (a) Loss of vertical fin of a B-52H Stratofortress aircraft (taken from `https://www.thisdayinaviation.com/10-january-1964/`). (b) DC-8 cargo aircraft lost one engine and parts of the right wing (taken from `https://ral.ucar.edu/sites/default/files/public/images/aap/turb1_lg.jpg`). (c) B737 accident at Denver Airport (taken from `https://aviationsafetynetwork.wordpress.com/tag/mountain-wave/`).

Frequently, incidents in aviation have been attributed to MWT. For instance on 10

January 1964 a B-52H Stratofortress aircraft flew at an altitude of about 4.4 km through an area characterized by a rotor associated with a MW and lateral shear due to flow around topography [1]. Gusts up to about 14 m s^{-1} during the incident were reported and in the course of the encounter the vertical fin was lost (see Fig. 1.2 a). Other examples of aviation incidents associated with MW activity comprise the severe turbulence encounter of a DC-8 cargo jet at 9.7 km above mean sea level (Clark et al. 2000, see Fig. 1.2 b) and significant crosswind encounter of a Boeing 737 jetliner during takeoff at the Denver International Airport (Keller et al. 2015, see Fig. 1.2 c). These examples demonstrate that MWT affect aviation at all flightlevels from ground up to the upper troposphere and lower stratosphere (UTLS) region.

1.2 Mountain Waves

The importance of MWs and the associated turbulence, not only to aviation safety but to the general atmospheric circulation from the boundary layer to the middle atmosphere through, e.g., the transport and deposition of momentum, is well established (e.g. Eliassen and Palm 1961, Fritts and Alexander 2003). As MWs can propagate horizontally and vertically over large distances they also couple the atmospheric layers between the lower, middle and upper atmosphere (Holton 1982, Fritts and Dunkerton 1985). Furthermore, the turbulence generated by MW breaking contributes to the redistribution of atmospheric constituents as e.g. water vapor, ozone and aerosols (e.g. Dörnbrack 1998, Heller et al. 2017).

Due to their acknowledged significance, numerous campaigns devoted to enhancing the scientific knowledge of mountain wave excitation, propagation, and dissipation have been conducted. Among these are the Momentum Budget over the Pyrénées experiment (PYREX; Bougeault et al. 1990, 1993), the Mesoscale Alpine Programme (MAP; Bougeault et al. 2001), the Terrain-induced Rotor EXperiment (T-REX; Grubišić et al. 2008), the Gravity Wave Life Cycle I (GW-LCYCLE I) campaign (Wagner et al. 2017), and the Deep Propagating gravity WAVe Experiment (DEEPWAVE) (Fritts et al. 2016). In the same spirit of the preceding field campaign, the Gravity Wave Life Cycle II (GW-LCYCLE II) experiment took place above Northern Scandinavia from January to March 2016 (special issue in Atmospheric Chemistry and Physics: Sources, propagation, dissipation and impact of gravity waves[2]).

However, what are MWs? In general, atmospheric gravity waves (GWs) are air parcel oscillations around their initial position. In a stably stratified atmosphere a restoring force acts on a displaced air parcel to return to its initial position (Lin 2007). Yet, inertia causes the air parcel to overshoot the initial position which therefore moves in

[1] See https://www.thisdayinaviation.com/10-january-1964/

[2] See https://www.atmos-chem-phys.net/special_issue899.html

the opposite direction of the initial displacement (Lin 2007). This oscillation produces a wave that propagates vertically away from its source region and the buoyancy force acts as restoring force (Lin 2007). If the Coriolis force acts as an additional restoring force also horizontal oscillations are generated and the resulting waves are called inertia-GWs (Lin 2007). Scales of the horizontal wavelength can reach 10 to 1000 km and values of their intrinsic frequency (i.e. the frequency observed when moving with the mean flow) range from the Brunt-Väisälä frequency to the inertial (Earth) frequency (e.g. Gill 1982, Nappo 2013). Generation mechanisms of atmospheric GWs in the troposphere comprise convection, jets and fronts, secondary generation as well as orography (e.g. Smith 1979, Fritts and Alexander 2003, Vadas et al. 2003, Plougonven and Zhang 2014). The gravity waves excited by orography are called MWs.

a)

b)

Figure 1.3: Visualizations of Mountain Waves by lenticularis clouds (a) above New Zealand and (b) Lake Comer.

The discovery of MWs dates back to 1933 when German glider pilots Hans Deutschmann and Wolf Hirth first flew into the ”Moazagotl” lenticularis cloud above the Hirschberg valley in Silesia (Dörnbrack et al. 2006). Observations of MW structures and their vertical extent are first published by Kuettner (1938). These observations motivated in the 1940s theoretical studies to describe MWs (Queney 1948, Scorer 1949).

Depending on the atmospheric background static stability, the horizontal wind and the horizontal scales of topography, different MW regimes are generated (Lin 2007). In this framework MWs belong to the evanescent regime when their amplitudes decay exponentially with altitude. These kind of MWs occur when atmospheric background conditions are characterized by relatively weak static stability accompanied by strong horizontal wind speeds, or topography that is narrower than some threshold (Lin 2007). Propagating MWs on the other hand are found under conditions where relatively strong static stability and weaker horizontal wind speed are present, or wider topography. The propagating regime can be further subdivided into the non-hydrostatic and hydrostatic regime. Hydrostatic MWs are generated if the buoyancy force and vertical pressure gradient force are almost in balance. Therefore, the vertical acceleration can be ignored for this kind of MW (Lin 2007). In contrast to non-hydrostatic MWs the associated disturbances are confined in the horizontal to the mountain and repeat themselves vertically with a wavelength of $\frac{2\pi U}{N}$, where U is the horizontal wind speed and N is the static stability (Lin 2007).

In principal, vertically propagating MWs are not confined to the troposphere and can propagate deeply into the middle atmosphere (Holton 1982, Fritts and Dunkerton 1985). However, if the background horizontal wind speed becomes equal to the groundbased phase speed a critical level prohibiting MW propagation evolves (Lin 2007). When approaching this layer, phase lines become horizontal and consequently isentropes overturn and static instability developes (Lin 2007, Markowski and Richardson 2010). Therefore, MWs become unstable and break, generating by that way turbulence in this region (e.g. Clark and Peltier 1984, Fritts and Alexander 2003, Lin 2007). As their groundbased phase speed is equal to zero, a critical layer for MWs is co-located with a reversal or change of direction of the background horizontal wind (e.g. Baines 1995, Lin 2007, Nappo 2013).

Apart from critical levels, also large amplitude MWs are considered to be prone to generating turbulence by wave steepening and overturning (e.g. Fritts and Alexander 2003, Sharman et al. 2012b). At ground, large amplitude MWs are generated by flow over high and steep topography (e.g. Long 1972, Smith 1977). For vertically propagating MWs increasing amplitudes are favored by the decreasing air density with altitude (e.g. Fritts and Alexander 2003, Lin 2007) and wind shear layers (Smith 1977, 1989). Either of these processes can act independently or synergistically to increase MW amplitudes (e.g. Fritts and Alexander 2003, Sharman et al. 2012b). Furthermore, overturning large amplitude MWs can also produce a ”wave-induced critical level” when the background horizontal wind and the induced perturbation of the horizontal wind cancel each other out (Peltier and Clark 1979, Clark and Peltier 1984). In nature, it is considered that more than one of the mentioned effects can act together in the generation of MWT (Clark et al. 2000, Sharman et al. 2012b).

A valuable source for MW observations are aircraft measurements. Therefore several field projects have employed aircraft to observe MWs over the last 40 years (Smith et al. 2008). While the spatial and temporal coverage of MW observation is superior in satellite, superpressure balloons and radiosonde measurements, aircraft transects provide most detailed MW observations as they capture a bigger part of the spectrum of the probed MWs (Smith et al. 2016). These high-resolution observations were utilized in physical studies to validate basic assumptions in linear wave theory on wave generation and propagation. In this manner aircraft measurements for example of the MAP campaign were used to validate the steady-state assumption applied in linear MW theory (Smith et al. 2007). Aircraft observations have also proven to be a valuable source for determining momentum fluxes (e.g. Lilly and Kennedy 1973, Smith et al. 2008, 2016). With the introduction of global positioning system (GPS) measurements for the T-REX campaign in 2006, static pressure perturbations could be derived for the first time from aircraft observations and in the course also the energy fluxes associated with MWs were obtained (Smith et al. 2008). With this data set the Eliassen Palm relationship was confirmed (Smith et al. 2008, 2016, Bramberger et al. 2017, Portele et al. 2018). While numerous observational studies on MW propagation exist, still direct observations of the breaking of MWs are sparse (Sharman et al. 2012b).

1.3 Mountain Wave and MWT Forecasting

Recently state-of-the-art Numerical Weather Prediction (NWP) models attained horizontal resolutions of less than 10 km. Thus, high-resolution global model data becomes a valuable source for detecting and predicting mountain waves. In that context recent increase of horizontal resolution of the integrated forecast system (IFS) of the European Centre for Medium-Range Weather Forecasts (ECMWF) led to a realistic simulation of wave-induced mesoscale temperature anomalies (Dörnbrack et al. 2017). Moreover, the remarkable agreement of the simulated wave structure in the IFS short-term forecast and the spaceborne observations of polar stratospheric clouds (Dörnbrack et al. 2017) indicates a fundamental trend: the finer resolution and increasing realism of operational NWP model outputs offers a valuable quantitative source for mesoscale flow components which were so far not accessible globally (Bauer et al. 2015).

However, while linear theory has been established for several decades and numerical models have been able to successfully reproduce MW characteristics, the prediction of MWs and the associated turbulence remains an outstanding question (Doyle et al. 2011, Sharman et al. 2012b).

In a multimodel study "relatively" low predictability especially of stratospheric MW breaking was found (Doyle et al. 2011). Although using the same initial states and a sophisticated set of different high-resolution numerical models with a horizontal resolution of 1 km, the results of these models showed marked differences (Doyle et al. 2011). These differences increased with the introduction of a larger mountain height. The found diversity of model results was attributed to differences in the dynamical cores of the numerical models. Therefore, application of a probabilistic approach for the prediction of timing and location of MW breaking and the associated turbulence was suggested.

To make up for the forecasting deficiencies of MW breaking and the consequent turbulence, current strategies for turbulence prediction and avoidance in aviation include (Lane et al. 2009, Kim et al. 2011):

1. avoidance of turbulent locations identified in Pilot Reports (PIREPs) of turbulence encounters
2. application of advisories (e.g. Airmen's Meteorological Information (AIRMET) Significant Meteorological Information (SIGMET)) or empirical forecasting techniques where satellite images are analyzed with respect to MW signatures to infer locations of enhanced MWT potential (Uhlenbrock et al. 2007).
3. use of local high-resolution numerical models that explicitly resolve aircraft-scale turbulence (Clark et al. 2000, Ólafsson and Ágústsson 2009, Lane et al. 2009, Kim and Chun 2010, Elvidge et al. 2017)
4. derivation of the atmospheric turbulence potential from gridded NWP output by using a sophisticated set of multiple turbulence diagnostics as is done in the Graphical Turbulence Guidance Tool (GTG) (Sharman et al. 2006, Sharman and Pearson 2017, Kim et al. 2018)

The GTG provides automated, aircraft-type independent turbulence forecasts for CAT and MWT at all flight levels from surface to the lower stratosphere (FL500) (Sharman et al. 2006, Sharman and Pearson 2017). In this framework, a "pragmatic" approach is used to forecast MWT where MWT diagnostics are calculated by a simple multiplication of the CAT prediction with a terrain-dependent quantity (Sharman and Pearson 2017).

1.4 Goals and Hypothesis

In the following, two case studies are presented where both of these deal with atmospheric impacts on flight conditions of high-flying aircraft. One case study analyzes a stall warning event of the High Altitude LOng Range Research Aircraft

(HALO) whereas the second study addresses a turbulence encounter of the research aircraft HALO and Service des Avions Francais Instrumentés pour la Recherche en Environnement (Safire) Falcon. Both encounters have in common that they took place above mountainous terrain when ambient atmospheric conditions favored the generation of MWs.

For the presented analyses a comprehensive data set is available comprising high-resolution in situ aircraft measurements, Quick Access Recorder (QAR) data of HALO, European Centre for Medium-Range Weather Forecasts (ECMWF) Integrated Forecast System (IFS) forecasts and operational analyses, GTG aviation turbulence forecasts, 2D and 3D high-resolution, idealized Eulerian semi-Lagrangian fluid solver (EULAG) simulations and lidar as well as radar measurements.

In general, important aircraft performance parameter comprise the lift, thrust and aircraft speed. All these parameters depend on the ambient distribution of temperature and wind in the atmosphere where it is well established that the lift and thrust depend on the air density and by that way also on temperature. As air density decreases exponentially with altitude it is strongly reduced at high altitudes. This reduction limits available lift and thrust which in turn restricts the aircraft's ability to respond to large changes in aircraft speed. By this way aircraft flying in the lower stratosphere at altitudes of about 13 km-14 km, as in the presented case studies, are especially sensitive to horizontal variations in temperature. In this altitude region aircraft speed is described by the Mach Number Ma. Fundamentally, Ma depends on the temperature. However, the measurement system of aircraft takes into account the relative speed of the aircraft to the ambient horizontal wind speed. In the following the question is addressed which of the two atmospheric state parameters affects aircraft speed the most. Therefore, the first hypothesis is:

- The horizontal wind speed is the dominant atmospheric parameter influencing aircraft speed and not the atmospheric temperature.

Breaking MWs and their associated turbulence are a well acknowledged hazard to aviation (e.g. Sharman et al. 2012b, Sharman and Pearson 2017). However, for vertically propagating MWs amplitudes increase with altitude due to the decreasing density (e.g. Fritts and Alexander 2003, Lin 2007). That way the modulation of the background temperature and wind field enhances with altitude. These induced variations could affect especially aircraft flying at high altitudes as the margin in the flight envelope to the minimum needed stall speed or maximum operating Ma reduces significantly. This leads to the following hypothesis:

- Propagating mountain waves can pose hazard for high-flying aircraft in addition to the well known turbulence caused by breaking mountain waves.

Recent progress in the horizontal resolution of state-of-the-art NWPs models lead to more realistic results in the simulation of wave-induced mesoscale temperature anomalies (Dörnbrack et al. 2017). In their study they concluded moreover that the finer resolution leads to increasing realism in the representation of mesoscale processes as e.g. atmospheric GWs. Yet, due to their model setup NWPs may still have deficiencies in capturing the non-linear part of the GW spectrum. Therefore, the third hypothesis is:

- Current forecast tools do not accurately predict the observed incidents even with a horizontal resolution of 8 km to 9 km.

With the data set at hand the goal of this thesis is on the one hand to identify atmospheric processes impacting high-flying aircraft in these two studies and, on the other hand to determine what atmospheric state parameter influences aircraft speed the most and on which scales. Furthermore, the predictability of the encountered events is validated.

In the following, theoretical principles regarding GW excitation and propagation, and aircraft aerodynamics are explained in chapter 2. Subsequently chapter 3 presents the data set together with applied methods and the results of the two case studies are given in chapter 4. Concluding, the results are discussed in chapter 5 and a summary together with conclusions is provided in chapter 6.

2 Theory

2.1 Gravity Wave Theory

Atmospheric GWs are oscillations of an air parcel around its equilibrium position (Fig. 2.1). The restoring force for these oscillations is the buoyancy force resulting from the adiabatic displacement in a stably stratified atmosphere. GWs are detectable by measurements as perturbations in the atmospheric state parameters as e.g., the three wind components and the temperature. In linear theory the fluctuations around the initial position are described as small perturbations from a background state (Fritts and Alexander 2003, Lin 2007). Therefor all parameters are decomposed by $X = \overline{X} + X'$ where X' refers to the perturbation from a background state $\overline{X}$.

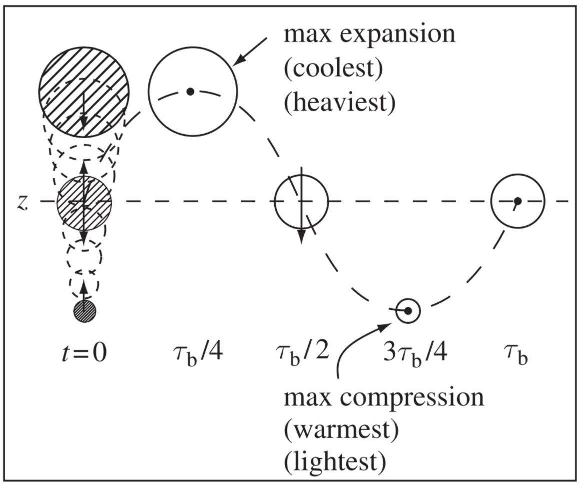

Figure 2.1: Vertical oscillation of an air parcel in a stably stratified atmosphere. The oscillation period τ_b can be derived by $\tau_b = 2\pi/N$ with the Brunt-Väisälä frequency N. Taken from (Lin 2007).

A general mathematical description of atmospheric GWs can be derived from the linearized form of the fundamental fluid equations:

$$\frac{du'}{dt} + w\frac{\partial \bar{u}}{\partial z} - fv' + \frac{\partial}{\partial x}\left(\frac{p'}{\bar{\rho}}\right) = 0, \tag{2.1}$$

$$\frac{dv'}{dt} + w\frac{\partial \bar{v}}{\partial z} + fu' + \frac{\partial}{\partial y}\left(\frac{p'}{\bar{\rho}}\right) = 0, \tag{2.2}$$

$$\frac{dw'}{dt} + \frac{\partial}{\partial z}\left(\frac{p'}{\bar{\rho}}\right) - \frac{1}{H}\left(\frac{p'}{\bar{\rho}}\right) + g\frac{\rho'}{\bar{\rho}} = 0, \tag{2.3}$$

$$\frac{d}{dt}\left(\frac{\theta'}{\bar{\theta}}\right) + w'\frac{N^2}{g} = 0, \tag{2.4}$$

$$\frac{d}{dt}\left(\frac{\rho'}{\bar{\rho}}\right) + \frac{\partial u'}{\partial x} + \frac{\partial v'}{\partial y} + \frac{\partial w'}{\partial z} - \frac{w'}{H} = 0, \tag{2.5}$$

$$\frac{1}{a^2}\left(\frac{p'}{\bar{\rho}}\right) - \frac{\rho'}{\bar{\rho}} = \frac{\theta'}{\bar{\theta}}, \tag{2.6}$$

with the time t, air density ρ, pressure p, the speed of sound a, Earth's acceleration g, the scale height H and the zonal, meridional and vertical wind components u, v, w as well as the Coriolis parameter $f = 2\Omega sin\phi$ (where Ω is the Earth rotation rate and ϕ is the latitude). Here (and in the following), the primed quantities are perturbations to a mean background state (indicated by overbars) of the atmosphere and the time derivative d/dt in its linearized form is given by

$$\frac{d}{dt} = \frac{\partial}{\partial t} + \bar{u}\frac{\partial}{\partial x} + \bar{v}\frac{\partial}{\partial y} \tag{2.7}$$

(Fritts and Alexander 2003).

N denotes the Brunt-Väisälä frequency and can be derived from

$$N = \sqrt{\frac{g}{\theta}\frac{\partial \theta}{\partial z}} \tag{2.8}$$

with the potential temperature θ given by

$$\theta = T\left(\frac{p_0}{p}\right)^{\kappa} \tag{2.9}$$

where κ denotes the ratio of the ideal gas constant R and the specific heat at constant pressure ($\kappa = R/c_p$), p_0 refers to the pressure at reference level z_0 ($p_0 = p(z_0)$) and T is the temperature (Nappo 2013).

Fundamental properties describing wave motions are e.g. the wave frequency, wave number, phase speed, group velocity and the dispersion relationship (Lin 2007). The horizontal and vertical wavenumbers (k, l, m) are defined by the spatial wavelength (λ_x, λ_y, λ_z) via $k = \frac{2\pi}{\lambda_x}$, $l = \frac{2\pi}{\lambda_y}$ and $m = \frac{2\pi}{\lambda_z}$. In this context, a wave can be characterized by its amplitude A and phase. Monochromatic wave-perturbation relations are given by

$$u' = A_u \exp\left[i(kx + ly + mz - \omega t) + \frac{z}{2H}\right], \tag{2.10}$$

$$v' = A_v \exp\left[i(kx + ly + mz - \omega t) + \frac{z}{2H}\right], \tag{2.11}$$

$$w' = A_w \exp\left[i(kx + ly + mz - \omega t) + \frac{z}{2H}\right], \tag{2.12}$$

$$\frac{\theta'}{\bar{\theta}} = A_\theta \exp\left[i(kx + ly + mz - \omega t) + \frac{z}{2H}\right], \tag{2.13}$$

where $\omega = \Omega + ku + lv$ is the ground based frequency which is the Doppler shifted (by the background wind) intrinsic wave frequency Ω (Fritts and Alexander 2003). Here, the phase is given by the sum $kx + ly + mz - \omega t$ and A_u, A_v, A_w, A_θ are the respective amplitudes.

In the context of linearly propagating GWs the dispersion relation links the wave frequency to the wave number (Fritts and Alexander 2003, Lin 2007) and is given by

$$\Omega^2 = \frac{N^2(k^2 + l^2) + f^2\left(m^2 + \frac{1}{4H^2}\right)}{k^2 + l^2 + m^2 + \frac{1}{4H^2}}. \tag{2.14}$$

Lines of constant phase within a wave (e.g. crest or trough), propagate through the atmosphere with the so-called phase speed in the direction of the wavenumber vector (Lin 2007). The phase speed relative to ground for an environment with constant wind is determined by

$$c_{px} = \frac{\omega}{k}; \qquad c_{py} = \frac{\omega}{l}; \qquad c_{pz} = \frac{\omega}{m}. \tag{2.15}$$

In the atmosphere GWs occur in form of wave packets (e.g. Markowski and Richardson 2010). This means that atmospheric GWs consist of a superposition of multiple wave components with slightly different wavelengths (Lin 2007, Markowski and Richardson 2010). If this wavepacket is nondispersive then the envelope of these individual waves (wave group) propagates through the atmosphere with the group velocity (Fig. 2.2). The group velocity is given by

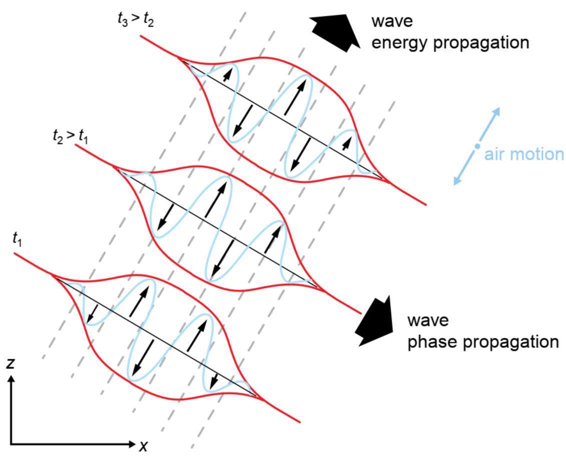

Figure 2.2: Schematic of the relationship between wavefronts, phase speed, and group speed (wave energy propagation) for a vertically upwards propagating gravity wave. Taken from Markowski and Richardson (2010) which was adapted from Lin (2007).

$$c_{gx} = \frac{\partial \omega}{\partial k} = \frac{k(N^2 - \Omega)}{\Omega(k^2 + l^2 + m^2 + \frac{1}{4H^2})} + \bar{u}, \tag{2.16}$$

$$c_{gy} = \frac{\partial \omega}{\partial l} = \frac{l(N^2 - \Omega)}{\Omega(k^2 + l^2 + m^2 + \frac{1}{4H^2})} + \bar{v}, \tag{2.17}$$

$$c_{gz} = \frac{\partial \omega}{\partial m} = \frac{-m(\Omega^2 - f^2)}{\Omega(k^2 + l^2 + m^2 + \frac{1}{4H^2})}. \tag{2.18}$$

(Fritts and Alexander 2003). Furthermore, the group velocity describes the energy transport of atmospheric GWs which is perpendicular to the wave vector (see Fig. 2.2).

For nondispersive GWs the different wavelengths in a wave packet have the same phase speed meaning that the phase speed is independent of wave number (Lin 2007). The opposite is valid for dispersive GWs and consequently these waves loose their initial coherent shape when propagating through the atmosphere as each wavelength is propagating with a different phase speed.

It is possible to derive the Taylor Goldstein equation by combining equations (2.1) - (2.6) to one single equation. For two-dimensional (x,z), linear, non-rotating, inviscid Boussinesq flow with varying background wind U and Brunt-Väisälä frequency N this equation is given by

$$\frac{\partial^2 \hat{w}}{\partial z^2} + m^2(z)\hat{w} = 0 \tag{2.19}$$

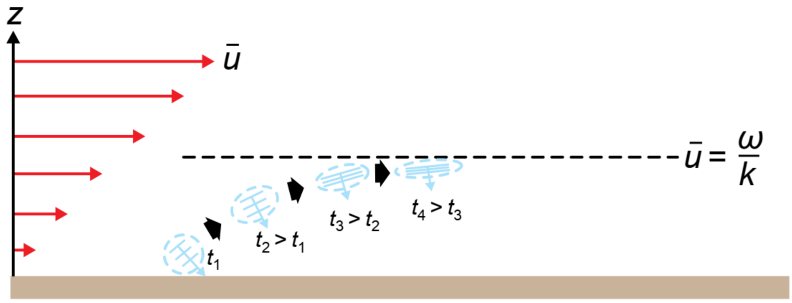

Figure 2.3: Schematic of a critical level (dashed line) and its impact on GW propagation (wave packets are shown in light blue). The red arrows refer to increasing background horizontal wind speed with altitude. Taken from Markowski and Richardson (2010) which was adapted from Lin (2007).

where $\hat{w} = A_w \cdot \exp(-z/2H)$ (e.g., Eq. (2.36) in Nappo 2013) and the vertical wavenumber m is determined by

$$m^2(z) = \frac{N^2}{(U - c_{ph})^2} + \frac{1}{(U - c_{ph})} \frac{\partial^2 U}{\partial z^2} - k^2. \tag{2.20}$$

For the condition that the background horizontal wind speed $U(z)$ is equal to the horizontal phase speed ($U(z) = c_{ph}$) the Taylor-Goldstein equation (Eq. 2.19) has a singularity. Physically this means that in atmospheric layers for which this condition is true, a critical level evolves prohibiting the upward propagation of GWs as they are breaking (Fig. 2.3). Therefore the flow in this region is highly non-linear and characterized by strong turbulent mixing (Lin 2007). Consequently, linear theory is not suitable to describe the atmospheric flow in the vicinity of these levels. Because observed GWs often consist of different wave modes propagating at different phase speeds a layer of critical levels can be formed, i.e. the critical layer (Lin 2007).

A similar process was found between an altitude of 15 km to 20 km, in the lower stratosphere, where the background horizontal wind field is often characterised by strong negative vertical shear leading to low magnitudes of the horizontal wind speed (Kruse et al. 2016). In this region, Kruse et al. (2016) found a layer where the low horizontal wind speeds promote wave steepening and nonlinear attenuation through GW breaking (see Fig. 2.4). By this way this layer controls the deep vertical propagation of MWs through it and is therefore named the 'valve layer'. However, an important condition for the attenuation of MWs in this layer is the magnitude of the incident wave amplitude as large-amplitude waves are more likely to break down than small-amplitude ones (Kruse et al. 2016).

The orographically forced MWs are due to their source mechanism stationary and therefore their phase speed equals zero. Moreover, the Taylor Goldstein equation for

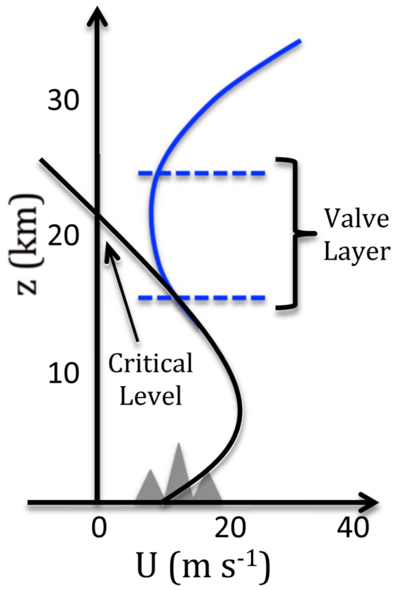

Figure 2.4: Schematic of a valve layer in the lower stratosphere. The black line shows the vertical profile of zonal wind speed with a critical level while the blue line refers to a zonal wind profile with a weak-wind valve layer. Taken from Kruse et al. (2016).

MWs has an evanescent solution if the horizontal wavenumber is larger than the Scorer parameter

$$\ell^2(z) = \frac{N^2}{U^2} - \frac{\frac{\partial^2 U}{\partial z^2}}{U}. \tag{2.21}$$

which is derived from Eq. 2.19 with $c_{ph} = 0$ and has the unit of wavenumber. A propagating solution is found if the horizontal wavenumber is smaller than ℓ. By this way the Scorer parameter is a useful method to determine the altitude levels MWs of a certain horizontal scale can reach.

However, with the Scorer parameter also insight can be gained whether trapping of MWs occurs between two atmospheric layers. If the Scorer parameter decreases strongly with altitude from a lower layer with high stability and an upper layer with lower stability it divides the atmosphere into two regions. MWs become trapped between those two layers if their Scorer parameter is larger than the Scorer parameter of the lower layer and smaller than the one of the upper layer, respectively ($\ell_{lower} > \ell > \ell_{upper}$). This means that at the lower boundary they are propagating while they become evanescent at the upper boundary (Markowski and Richardson 2010).

In their study Eliassen and Palm (1961) found that the vertical flux of wave energy varies with height in proportion to the background wind. This is in contrast to the vertical flux of horizontal momentum which is constant with altitude for linearly upwards propagating MWs. By assuming nonresonant, vertically propagating and non-dissipating internal gravity waves in a steady flow with no critical level, the Eliassen-Palm relation can be used to test linearity of observed vertically propagating MWs. This relation is given by

$$EF_z = -(\bar{u}MF_x + \bar{v}MF_y) \tag{2.22}$$

where MF_x and MF_y are the zonal and meridional components of the vertical momentum flux vector and EF_z is the vertical energy flux, respectively. $\bar{u}$ and $\bar{v}$ are the zonal and meridional components of the horizontal background wind. The product on the right hand side of horizontal wind speed and vertical flux of horizontal momentum will be referred to as UMF in the turbulence case study. For more details on how to calculate the momentum fluxes in particular from aircraft in situ measurements see Sec. 3.1.3.

2.2 Aerodynamics

To understand the way an autopilot reacts to changes in the atmosphere a short introduction to some aerodynamic aspects is given in the following.

In aerodynamics important equations comprise (among others) the continuity equation (Eq. 2.23), Euler's equation (Eq. 2.24) and the Bernoulli equation (Eq. 2.25) given by

$$\dot{m} = \rho A V \Rightarrow \rho_1 A_1 V_1 = \rho_2 A_2 V_2, \tag{2.23}$$

$$-dp = \rho V dV, \tag{2.24}$$

$$p_{s1} + \frac{1}{2}\rho V_1^2 = p_{s2} + \frac{1}{2}\rho V_2^2 = p_t \tag{2.25}$$

where $\dot{m}$ is the mass flow rate, ρ_1 and ρ_2 are the densities at locations 1 and 2,respectively. A_1 and A_2 are the areas at the two locations while V_1 and V_2 are the flow velocities at the respective locations. p_s denotes the static pressure.

Assuming weightless, frictionless, inviscid flow along a streamline, in aerodynamics Euler's equation (Eq. 2.24) is a statement of Newton's second law. In this framework the only remaining force is the pressure imbalance along a streamline which is equal to the mass of the fluid multiplied by the rate of change of its velocity V (Brandt 2004). With this equation any change of flow velocity is related to a change of pressure along a streamline (Brandt 2004, Corda 2017).

The Bernoulli equation derives from Euler's equation under the assumption of inviscid, incompressible flow where body forces are negligible (Brandt 2004). In this concept p_s is the static pressure and the second term $\frac{1}{2}\rho v^2$ determines the dynamic pressure. As shown in Eq. 2.25 the total pressure p_t is the sum of the dynamic and static pressures. Along a streamline, the total pressure is assumed to be constant (Brandt 2004).

An application of the Bernoulli equation is the measurement of airspeed via a Pitot-Static tube (Fig. 2.5).

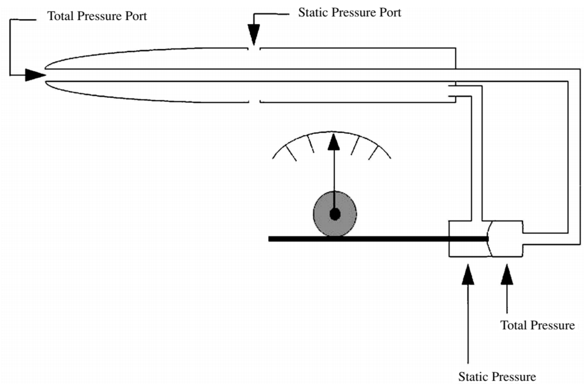

Figure 2.5: Schematic of the Pitot-Static tube which is used to measure aircraft speed. Taken from Brandt (2004)

This device consists of a Pitot tube, a static port and a system to measure the differential pressure (i.e. difference between total and static pressure). Here, the Pitot tube is placed with its opening perpendicular to the aircraft-surrounding airflow (Brandt 2004). At the opposite end the Pitot tube is blocked and therefore air cannot flow in the tube which leads to a stagnation point at the entrance of this tube (Brandt 2004). The velocity of the flow at this point is equal to zero and through Eq. 2.25 the p_t is equal to p_s. By this way the Pitot tube measures the total pressure and transmits it to the aircraft system.

The static port on the other side is oriented parallel to the streamlines of the flowfield with the intention that no stagnation developes and the measurement is as close as possible to the static pressure of the surrounding airflow (Brandt 2004).

2.2.1 Aircraft Speeds

Depending on the flow regime in which the aircraft is moving the true airspeed v_T is calculated in different ways (Corda 2017).

TAS in Subsonic Incompressible Flow

Solving Eq. 2.25 for the velocity yields with

$$v_T = \sqrt{2\left(\frac{p_t - p_s}{\rho}\right)} \tag{2.26}$$

the True Airspeed (TAS) of an aircraft in subsonic incompressible flows. It requires the measurement of p_t and p_s as well as ρ (via temperature). However, the applicability of Eq. 2.26 is limited to flows with $Ma \lesssim 0.3$ or airspeeds $\lesssim 100\,\mathrm{m\ s^{-1}}$ (Corda 2017).

TAS in Subsonic Compressible Flow

With increasing Ma ($Ma > 0.3$) the incompressibility assumption of the flow is no longer valid. However, the isentropic assumption is still true as no shock waves form in this kind of flow. In this flow regime Ma is calculated by

$$Ma = \sqrt{\frac{2}{\gamma - 1}\left[\left(\frac{p_t - p_s}{p_s} + 1\right)^{\frac{\gamma-1}{\gamma}} - 1\right]}, \tag{2.27}$$

where γ is the ratio of specific heats (Corda 2017). As Ma is also the ratio of aircraft speed and speed of sound a, TAS (v_T) is calculated in this flow regime by

$$v_T = a * Ma = \sqrt{\frac{2\gamma}{\gamma - 1}\left(\frac{p_s}{\rho}\right)\left[\left(\frac{p_t - p_s}{p_s} + 1\right)^{\frac{\gamma-1}{\gamma}} - 1\right]}. \tag{2.28}$$

As indicated by Eq. 2.28, the TAS depends on the measurement of the pressure difference, of the static pressure and temperature. The latter one is needed to obtain the air density. Therefore three independent devices are necessary to obtain a correct TAS (Corda 2017).

More Aircraft Speeds - ICeT

However, so far TAS indicators have a tendency to be difficult to calibrate and have had accuracy and reliability issues (Corda 2017). Therefore simplifactions are necessary in order to obtain correct speed measurements. To simplify the measurements, the assumption is made that the air density is independent of altitude and thus equal to the value at standard sealevel (ρ_{SL}). The aircraft speed calculated in this manner is called the Equivalent Airspeed (EAS) and is given by

$$v_E = v_T\sqrt{\frac{\rho}{\rho_{SL}}} = \sqrt{\frac{2\gamma}{\gamma-1}\left(\frac{p_s}{\rho_{SL}}\right)\left[\left(\frac{p_t-p_s}{p_s}+1\right)^{\frac{\gamma-1}{\gamma}}-1\right]}. \tag{2.29}$$

The EAS can also be used to calculate structural loads scale, to determine altitude independent stall speeds or landing approach speed (Corda 2017).

Further simplifaction involves the assumption that also the static pressure is independent of altitude and equal to the pressure at standard sealevel (p_{SL}). This airspeed is called Calibrated Airspeed (CAS) and is calculated with

$$v_C = \sqrt{\frac{2\gamma}{\gamma-1}\left(\frac{p_{SL}}{\rho_{SL}}\right)\left[\left(\frac{p_t-p_s}{p_{SL}}+1\right)^{\frac{\gamma-1}{\gamma}}-1\right]}. \tag{2.30}$$

The only remaining unknown in Eq. 2.30 is the pressure difference which can be obtained with the Pitot-static tube. From a measurement point of view this instrument is more reliable as less accuracy issues are present and fewer calibration is necessary (Corda 2017).

Airspeed indicators are often designed to use the CAS (Corda 2017) as given in Eq. 2.30. But the Indicated Airspeed (IAS) itself is not equal to the CAS due to instrument errors Δv_{instr} (Corda 2017). It is therefore given by

$$v_I = v_C - \Delta v_{instr}. \tag{2.31}$$

Pilots refer to the different aircraft speeds with the phrase "ICeT" where I is the indicated airspeed, C stands for the calibrated airspeed, e for the equivalent airspeed and T to the true airspeed, respectively.

For flying at high altitudes and high airspeeds the autopilot of HALO is programmed to fly at constant Ma as given by Eq. 2.27 for flight levels (FLs) higher than about FL 180. In this equation the airspeed depends on the pressure difference of the total and static pressure. Thus it can be derived with the Bernoulli equation that the aircraft speed is directly proportional to the relative speed (v_{rel}) between the aircraft and the horizontal wind speed in the direction along the aircraft. For subsonic, compressible flow this relation is given via the compressible Bernoulli equation

$$p_t - p_s = \frac{1}{2}\rho v_{rel}^2\left(\frac{\gamma-1}{\gamma}\right). \tag{2.32}$$

The ground-relative speed (v_G) of an aircraft is either determined by a GPS system or it is derived from wind measurements. In the latter case it is the difference of TAS and horizontal wind speed ($v_G = v_T - v_{wind}$).

2.2.2 Lift

Airfoils generate lift due to the pressure difference between the airfoil's upper and lower surfaces. As the flow speed is increased on the upper surface, the static pressure reduces in this area and becomes lower than the pressure on the lower surface (Corda 2017). Lift, L, can be calculated by

$$L = \frac{1}{2}\rho V_\infty^2 C_L A \tag{2.33}$$

with the air density ρ, the lift coefficient C_L, freestream velocity V_∞ and a reference area A.

2.2.3 Thrust

In principle, thrust is the force that moves an aircraft through the air and is used to overcome the drag of an airplane. It is a reaction force that can be described with Newton's second and third laws. An aircraft engine generates thrust by adding energy to a mass flow. When the mass flow exits the engine it's velocity is higher than that of the flow entering at the inlet of the engine. As the air accelerates to the rear, the reaction force, thrust, is directed toward the front. The thrust Thr of an engine can be calculated with

$$Thr = \dot{m}(V_{Ex} - V_\infty) = \rho A V (V_{Ex} - V_\infty) \tag{2.34}$$

where V_{Ex} is the velocity of the exhaust, V_∞ is the freestream velocity. $\dot{m}$ determines the mass flow rate through the engine and can also be expressed by air density ρ, the area A and the mass flow velocity V (Brandt 2004).

2.2.4 Angle of Attack

The Angle of Attack (AOA) (α) is the angle between the chord line of an airfoil and the freestream direction. Figure 2.6 visualizes the angle of attack of an airfoil.

If the AOA equals zero, the pressure above and below a symmetrical airfoil is equal and consequently no lift is generated (see Fig.2.6 a). Increasing the AOA leads to a

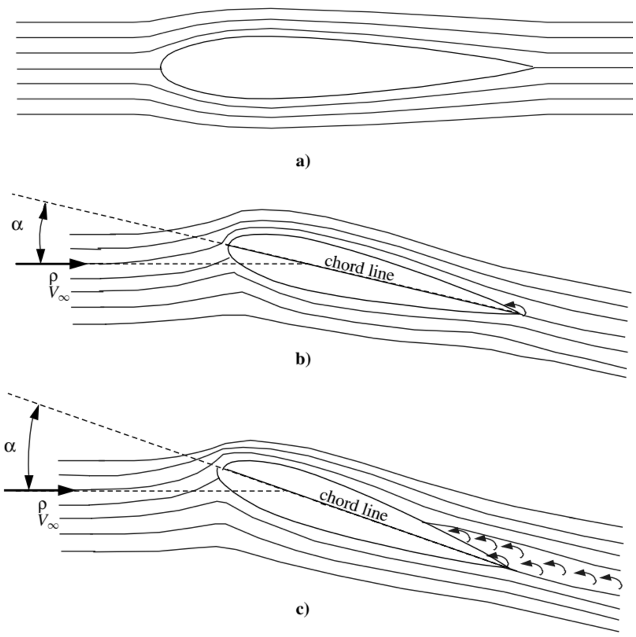

Figure 2.6: Schematic of the angle of attack (α) of an airfoil and its impact on the flow around the airfoil. (a) airfoil at zero α, (b) α for straight flying conditions and (c) developing stall for large α. Taken from Brandt (2004), their figure 3.22.

pressure difference above and below the airfoil which in turn produces lift. However, if the AOA is increased above a certain threshold, flow separation occurs (see small eddies in Fig.2.6 c) which could lead to stall on the airfoil.

2.2.5 Flight Envelope

Figure 2.7 shows the principle schematic for a flight envelope for flight levels above FL250 of an aircraft.

In this altitude versus aircraft-speed diagram, aircraft design together with the ambient density allow safe flights only inside an envelope limited by the aerodynamic lift (lower limit) and the airspeed (upper limit), respectively (Fig. 2.7).

The lift limit is on the left side of the flight envelope and it also gives the minimum, level-flight airspeed which is defined as the stall speed (Corda 2017). If the aircraft speed is reduced below the stall speed, the aircraft's wings cannot produce enough lift to balance the weight, as the flow over the wings separates and, consequently, the aircraft stalls.

The upper speed limit is given by the right branch in the flight envelope and is called maximum operating Ma. In this case, the maximum available thrust of the engines and

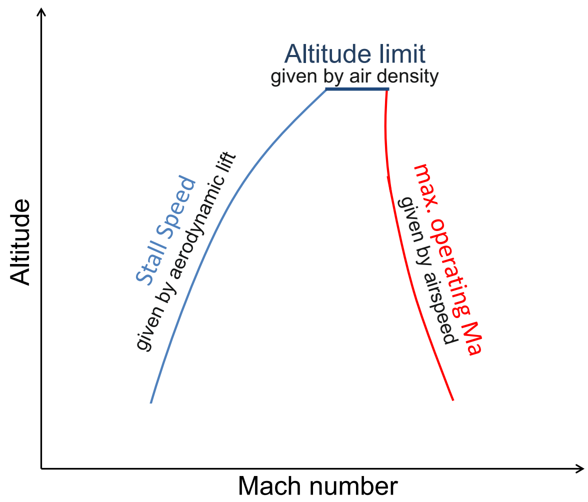

Figure 2.7: Schematic flight envelope at flight levels higher than FL250.

aerodynamic aspects contribute to this limit (Corda 2017). As air density decreases with increasing altitude, the available thrust is reduced with increasing flight levels (Brandt 2004). From an aerodynamic point of view, shock waves can evolve over the wing which on the one hand destroy the lift due to flow separation and on the other hand could cause controllability issues depending on their position with respect to the wing (Mach tuck). These shock waves form at transonic flow speeds over the wings ($Ma \approx 1$). As Ma is indirectly proportional to the speed of sound, which in turn depends on the air temperature, the Ma at which shock waves form, decreases with increasing altitudes.

For high-flying aircraft such as e.g. HALO, the stall speed and the maximum operating Ma nearly converge at the maximum possible flight altitude, a region which is called "coffin corner" by pilots (Corda 2017). However, the actual flown Ma does not only depend on the ambient temperature, but also on the horizontal wind speed in the along-track direction through Equations 2.27 and 2.32. That way, aircraft flying in proximity of the "coffin corner" might be easily affected by sudden and unexpected temperature and/or horizontal wind variations which could bring the aircraft speed close to the stall speed or the maximum operating Ma.

3 Data and Methods

In this chapter the used numerical and observational datasets are introduced. Additionally the methods how mountain wave fluxes and turbulence parameters are derived from in situ measurements are presented.

3.1 Measurements

3.1.1 Campaigns

The observational data set used was accumulated during two campaigns: the Life Cycle of Gravity Waves (GW-LCYCLE) II campaign and North Atlantic Waveguide and Downstream Impact Experiment (NAWDEX).

The GW-LCYCLE II experiment took place in Northern Scandinavia from January to March 2016 (special issue in Atmospheric Chemistry and Physics: Sources, propagation, dissipation and impact of gravity waves[3]). The goal of this campaign was the exploration of the complete life cycle of gravity waves from their excitation and propagation to their dissipation.

To reach this goal complementing ground-based and airborne measurement techniques were combined. Here, ground-based observations comprised radiosondes, lidars, radars and airglow imagers at different sites around northern Scandinavia as e.g. Kiruna and Sodankylä (see Fig. 3.1). Airborne observations were conducted with two different aircraft operating from Kiruna: the German Aerospace Center (DLR) Falcon and the German HALO. Different sensors were mounted on these aircraft as e.g. a five-hole sonde on the noseboom, downward-looking wind lidar, an airglow imager and the especially developed Gimballed Limb Observer for Radiance Imaging of the Atmosphere (GLORIA) system. Complementing the different measurements, additional numerical modeling was employed to gain deeper insight in the involved processes.

In contrast to the GW-LCYCLE II experiment, the NAWDEX campaign did not focus on GWs. In this campaign the center of attention was to improve weather prediction through enhancing the understanding of diabatic processes and their impact on Rossby

[3]See https://www.atmos-chem-phys.net/special_issue899.html

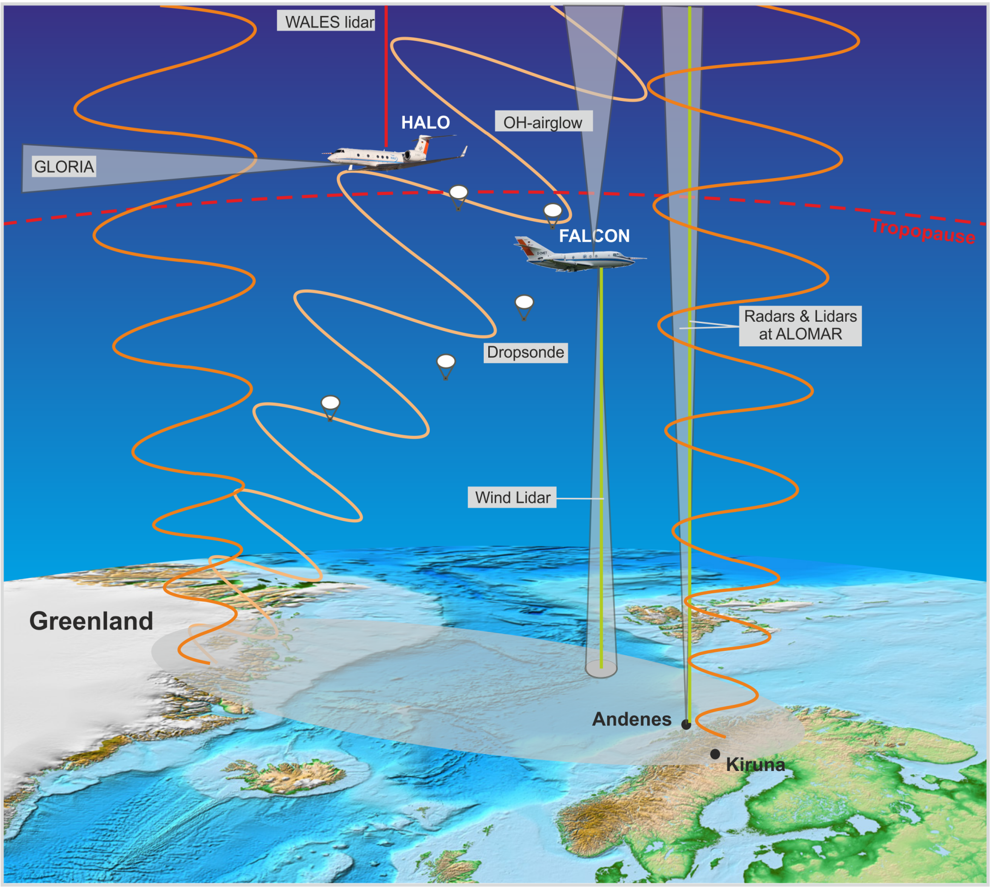

Figure 3.1: Overview on the covered area and the different measurement techniques employed during the GW-LCYCLE II campaign (Picture taken from `https://romic.iap-kborn.de/fileadmin/user_upload/Projekte/GW_LCYCLE/romic_DLR_5.png` on 8 October 2018).

wave propagation and downstream development of weather systems (Schäfler et al. 2018). Therefore this campaign was stationed in Iceland and the geographic research area covered the North Atlantic region north of 45° N and extended from eastern Canada to northern Europe (Fig 3.2). NAWDEX took place from September to mid October 2016.

This campaign also employed complementary airborne and ground-based measurements. Ground-based measurements enclosed radars, lidars and radiosonde observations (Schäfler et al. 2018). For NAWDEX a vast amount of radiosonde observations was available from 40 different stations in 14 countries as e.g eastern Canada, France, Iceland, Norway and the United Kingdom. Part of these radiosondes were supplied by the European Meteorological Services Network (EUMETNET).

Airborne observations were conducted by four different aircraft, DLR Falcon, the

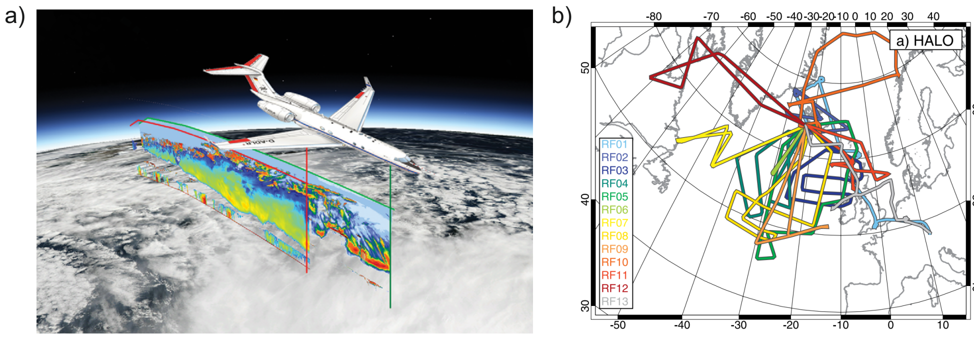

Figure 3.2: Overview of the different measurement techniques employed during the NAWDEX campaign on HALO (a) and the area covered by HALO research flights (b). Picture adapted from Schäfler et al. (2018).

German HALO, French Falcon from Safire and the British Facility for Airborne Atmospheric Measurements (FAAM) BAe 146. Except for the FAAM all aircraft were operating from Keflavik, Iceland. For this campaign HALO was equipped among others with a five-hole sonde in the noseboom, downward-looking radar and lidar systems and a dropsonde dispenser (Schäfler et al. 2018). Two downward-looking wind lidars were mounted on Falcon and the instrumentation on Safire and FAAM included dropsonde dispensers as well as lidars and radars (see Fig 3.2).

3.1.2 3D Wind Measurement on HALO

An important part of this work constitute in situ wind measurements of the research aircraft HALO. Therefore these measurements are introduced in more detail.

HALO in situ 3D wind measurements are obtained with a five-hole sonde mounted in HALO's noseboom (Fig. 3.3). The idea with a noseboom is to probe the "free" atmosphere in a state where it is not disturbed and deflected by the aicraft. That way unperturbed wind measurements are possible.

The five-hole sonde obtains a 3D wind vector field by measuring the total pressure in hole number 1 (see Fig. 3.4), the differential pressure in the other four holes and a static pressure port (nr 6 in Fig. 3.4). Via calibration the differential pressure between hole 4 and 5 as well as 2 and 3 can be converted to an AOA and angle of sideslip, respectively (Calmer et al. 2018). Via Bernoulli's equation (Eq. 2.25) the total pressure and the static pressure obtained from the static pressure port yield the air speed in a probe-relative coordinate system (Calmer et al. 2018). In order to obtain the wind speed, this air speed must be converted into an Earth-fixed coordinate system using an inertial navigation system. For HALO the system used to obtain the 3D wind measurements is called the Basic HALO Measurement and Sensor System (BAHAMAS)

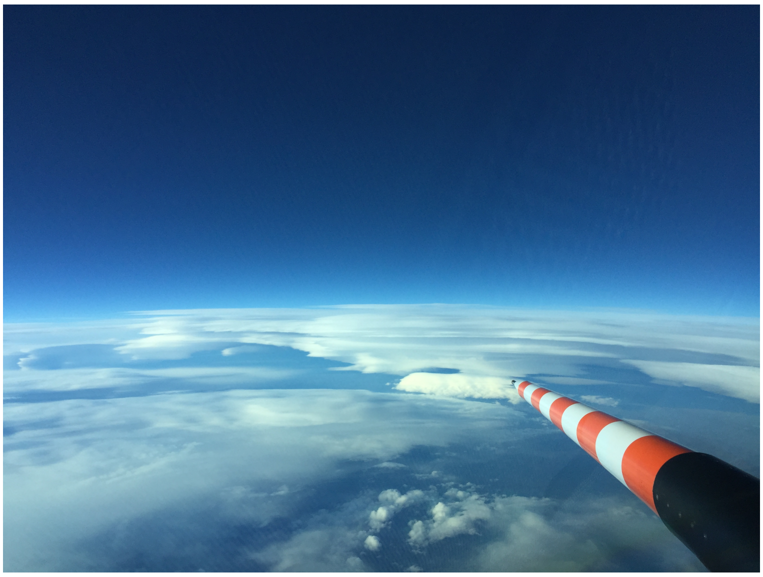

Figure 3.3: Photograph of HALO's noseboom during RF10 of NAWDEX (picture taken by Steffen Gemsa).

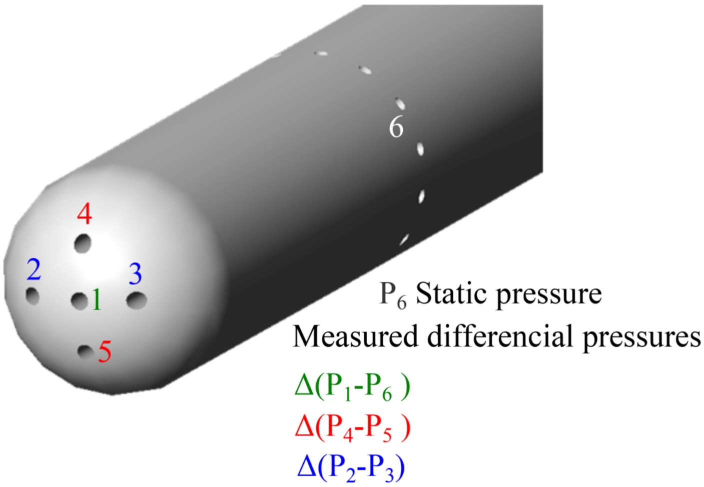

Figure 3.4: Schematic of a 5-Hole sonde as it is mounted in HALO's noseboom (picture adapted from Calmer et al. (2018).

(Giez et al. 2016). The acquisition frequency of this system is 1000 Hz, and data are averaged to 10 Hz for the case study analyses. The measurement uncertainties are given in Table 3.2 and were calculated with the procedure described in Mallaun et al. (2015).

Table 3.1: Overview on the measurements uncertainties for different parameters of HALO in situ measurements.

	Measurement uncertainty
static pressure	30 Pa
static temperature	0.5 K
horizontal wind	$0.5\,\mathrm{m\,s^{-1}}$
vertical wind (w)	$0.3\,\mathrm{m\,s^{-1}}$

3.1.3 Mountain Wave Energy- and Momentum-Fluxes

The BAHAMAS does not only provide measurements of all three wind components, but also observations of pressure and temperature (Giez et al. 2016). For the case studies data sampled at 10 Hz with a horizontal resolution of about 50 m are available. These in situ measurements at flight level are used to calculate local values of the vertical energy flux EF_z and the vertical fluxes of horizontal momentum MF_x and MF_y applying two different approaches. One method calculates leg-integrated values of MF_x, and MF_y by

$$MF_x = \frac{\overline{\rho}}{s}\int_0^s u'w'ds \qquad MF_y = \frac{\overline{\rho}}{s}\int_0^s v'w'ds \tag{3.1}$$

in units of Pa and of EF_z by

$$EF_z = \frac{1}{s}\int_0^s p'w'ds, \tag{3.2}$$

in units of $\mathrm{W\,m^{-2}}$ according to Smith et al. (2008). Here, $\overline{\rho}$ denotes the mean density along the leg, s the length of the leg and p', u', v', w' are the perturbations of the pressure, and the zonal, meridional and vertical wind components, respectively. The zonal and meridional components of the vertical momentum flux vector $\overrightarrow{MF}$ are given by MF_x and MF_y.

The pressure p used for calculating EF_z was hydrostatically corrected; for further information see Smith et al. (2008, 2016). The perturbation quantities u', v', w', and p'

are calculated from the flight level data u, v, w, and p by subtracting linear least-square fits (Bramberger et al. 2017). This approach removes large-scale gradients, e.g. when HALO is crossing synoptic-scale weather systems. These fluxes will be referred to as leg-integrated fluxes.

The second approach is used to access the spatial variability of the energy and momentum fluxes along the flight leg. For this purpose, the flight leg is subdivided into smaller sublegs with a length of 88 km and for each of these sublegs the fluxes are calculated individually using the equations 3.1 and 3.2. In the following these fluxes are referred to as subleg-integrated fluxes. The averages of the subleg integrated momentum and energy fluxes differ from the leg-integrated fluxes since different scales are captured by the two methods and different linear fits are subtracted from the flight level data.

For the study of the turbulence encounter above Iceland EF_z and UMF are determined for different scale ranges. This was done to analyze whether the linearity of MW propagation depends on the respective scale. For this analysis the fluxes are calculated by

$$EF_z = \overline{p'w'}, \tag{3.3}$$

$$EF_{zM} = -\rho(\overline{u} \cdot \overline{u'w'} + \overline{v} \cdot \overline{v'w'}), \tag{3.4}$$

$$HF = c_p\rho \cdot \overline{\theta'w'}, \tag{3.5}$$

where the overbars represent a moving average over 10 km and $\overline{u}$ and $\overline{v}$ are the mean zonal and meridional wind speeds over the complete flight leg. The vertical heat flux HF is calculated with the perturbation of the potential temperature θ and the specific heat at constant pressure $c_p = 1004\,\mathrm{J\,K^{-1}\,kg^{-1}}$. Note that the scales are separated using wavelets. The reconstructed signals comprise on the one hand horizontal wavelengths (λ_h) ≤ 5 km for the turbulent range and on the other hand 20 km to 70 km for the propagating MW range.

3.1.4 Wavelet analysis of Mountain Waves

The spectral analysis of the energy fluxes of the observed mountain waves is based on wavelet spectra (Torrence and Compo 1998). Following Woods and Smith (2010), the Morlet wavelet of order 6 is used as mother wavelet and the cospectra of the energy-, momentum- and heatfluxes are calculated by

$$\widetilde{EF}_n(s_j) = \Re\{\tilde{P}_n(s_j)\tilde{W}_n^*(s_j)\} \tag{3.6}$$

$$\widetilde{MF}_{xn}(s_j) = \Re\{\tilde{U}_n(s_j)\tilde{W}_n^*(s_j)\} \tag{3.7}$$

$$\widetilde{HF}_n(s_j) = \Re\{\tilde{T}_n(s_j)\tilde{W}_n^*(s_j)\} \tag{3.8}$$

where an appropriate scaling of $\tilde{P}_n(s_j)$ and $\tilde{W}_n(s_j)$ assures that the unit of $\widetilde{EF}_n(s_j)$ is $\mathrm{W\,m^{-2}}$ (Bramberger et al. 2017) and $\Re$ denotes the real part. Here, $\widetilde{HF}_n(s_j)$ is the cospectrum of the heatflux. The quantities $\tilde{P}_n(s_j)$, $\tilde{T}_n(s_j)$ and $\tilde{U}_n(s_j)$ are the wavelet transforms of p', u' and the perturbation of the temperature t' at spatial index n for the wavelet scale s_j at wavenumber index j. $\tilde{W}_n^*(s_j)$ denotes the complex conjugate of the wavelet transform of w'. Further details on the spectral analysis are given in Bramberger et al. (2017).

3.1.5 Turbulence Parameters TKE and EDR

To characterize atmospheric turbulence two different parameters are derived from the in situ measurements at flight level: the turbulent kinetic energy (TKE) and the cube root of the energy dissipation rate ($\epsilon^{1/3}$), which is commonly referred to as eddy dissipation rate (EDR). The parameter EDR is particularly useful as it can be related to aircraft-specific loads enabling calibration of EDR to different aircraft types in terms of aircraft response (MacCready 1964, Cornman et al. 1995, Sharman et al. 2014, Cornman 2016). Furthermore, EDR is the International Civil Aviation Organization (ICAO 2001) standard for aviation turbulence reporting. The ICAO document also provides estimates of 'light', 'moderate', 'severe', 'extreme' turbulence intensity thresholds for a medium-weight class aircraft. Turbulence thresholds used for HALO in the Iceland case study follow the suggestions of Sharman et al. (2014).

Note that the horizontal wind components were transformed into an aircraft coordinate system for the calculation of TKE and EDR in order to be consistent with former studies as e.g. Strauss et al. (2015). Thus, for this analysis u_{ac} refers to the longitudinal (along-track) and v_{ac} to the transverse (cross-track) horizontal wind component with respect to the aircraft.

The TKE per unit mass is calculated by $TKE = (\sigma^2_{u_{ac}} + \sigma^2_{v_{ac}} + \sigma^2_w)/2$ i.e., as half the sum of the variances of the wind fluctuations along the leg. For our analysis the TKE is calculated for different subleg lengths ranging between about 20 km and 4 km.

The calculation of EDR is based on Strauss et al. (2015) who used the inertial dissipation technique (IDT; Champagne 1978, Piper and Lundquist 2004, Večenaj et al. 2012), a method that takes into account the Kolmogorov form of the turbulent energy spectrum. In this framework, the spectral energy density S_i for the respective component of the wind velocity vector $u_i = \{u_{ac}, v_{ac}, w\}$ is given by

$$S_i(k) = \alpha_i \epsilon^{2/3} k^{-5/3} \tag{3.9}$$

where k is the wavenumber, i is the index of the respective component of the wind velocity vector and $\alpha_i = \{0.53, 0.707, 0.707\}$ are the Kolmogorov constants (Oncley et al. 1996, Piper and Lundquist 2004, Strauss et al. 2015). With the help of equation 3.9, the EDR can be computed from the spectrum of each wind velocity component u_i by

$$EDR_i = \epsilon_i^{1/3} = \left(\frac{\overline{S_i(k) k^{5/3}}}{\alpha_i} \right)^{1/2} . \tag{3.10}$$

In contrast to Strauss et al. (2015) who used sublegs of 2 km, the complete flight leg is divided into longer sublegs with a length of 4 km as the 10 Hz sampling frequency of our data set is lower than the data resolution in their study (25 Hz). Applying Welch's method (Welch 1967), each of these 4 km sublegs is subdivided into 3 overlapping segments for the stall warning study in section 4.1. For the study regarding the strong turbulence encounter in section 4.2 the mean is taken over three overlapping 4 km segments. (This was done in the course of code validation with the National Center for Atmospheric Research (NCAR)). For both methods the data are linearly detrended on the respective segments, a Tukey window is applied, and the spectral energy density is calculated with a fast Fourier transform. Note, the quantity S_i used to calculate EDR according to equation 3.10 is an arithmetic mean of the spectral energy densities over these three overlapping segments which is denoted by the overbar. Furthermore, we define a fixed frequency range within which EDR is calculated. For the stall warning event this range is between 0.1 Hz and 2 Hz while for the turbulence case study above Iceland the range could be extended to 3.5 Hz. This fixed frequency range is a compromise between taking into account as much data as possible with less variance in the spectral slope but excluding artifacts that could be due to aliasing, digital noise or other sources. For the stall warning event, the mean spectral slope in this frequency range for the spectral energy density of the vertical wind is -1.33 with a variance of 0.46. During the turbulence encounter this slope is -1.41 with a variance of 0.21, respectively.

With the EDR_i of each wind velocity component u_i we estimate a mean EDR, $\overline{EDR}$. Following Strauss et al. (2015) a geometric mean given by

$$\overline{EDR} = \sqrt[3]{EDR_{u_{ac}} + EDR_{v_{ac}} + EDR_w)} \tag{3.11}$$

is used.

3.2 Numerical Models

To complement and gain further insight in the atmospheric processes involved, numerical models are taken into account. These models comprise the ECMWF, GTG and EULAG.

3.2.1 ECMWF

To describe the synoptic situation during the research flights, hourly short-term forecasts and six-hourly operational analyses of the deterministic high-resolution IFS runs are combined to generate a continuous data set for the two flights. The IFS model is a global, hydrostatic, semi-implicit, semi-Lagrangian NWP model. For the stall warning case 12 January 2016, the high-resolution analyses and forecasts of the pre-operational IFS cycle 41r2[4] are used. For NAWDEX this cycle was operational and is, therefore, also employed in the case study regarding the turbulence encounter of HALO (see Sec. 4.2).

The horizontal resolution of all different operational applications using the IFS were increased when the IFS cycle 41r1 ($\Delta x \approx 16$ km) was replaced by cycle 41r2 on 8 March 2016 (Hólm et al. 2016). The corresponding high-resolution analyses and forecasts are computed on a cubic octahedral grid with $\Delta x \approx 9$ km while the spectral truncation remained at wavenumber 1279 ($\mathrm{T_{Co}}1279$, Malardel and Wedi 2016)[5]. Other sources for the gain in effective resolution are the reduced numerical filtering in the model and the preparation of physiographic data at the surface. During January 2016, the IFS cycle 41r2 was running pre-operationally in parallel and all data were archived at the ECMWF.

In the vertical, 137 levels range from the model top at a pressure level of 0.01 hPa (≈ 80 km altitude) down to the surface (≈ 10 m altitude). In the lower stratosphere, the vertical resolution is about 500 m. For the stall warning study (Sec. 4.1) two data sets with different spectral resolutions are retrieved and interpolated on the same regular $0.125° \times 0.125°$ latitude/longitude grid. For presenting the high-resolution fields, the highest available spectral resolution of $\mathrm{T_{Co}}1279$ is used.

3.2.2 GTG

Turbulence forecasts of the GTG are calculated from the operational IFS short-term forecasts. The way the GTG is designed, it depends on the scale of the input NWP, and cannot actually resolve turbulence.

Instead, the GTG uses an ensemble of many different CAT diagnostics describing different physical processes under the assumption that a downscale cascade from the larger resolved scales to the aircraft scales exists. All the different diagnostic quantities are projected to one common, aircraft type-independent forecast parameter, the EDR (see Appendix A.2 for a list of the employed diagnostics).

[4]See https://www.ecmwf.int/en/forecasts/documentation-and-support/changes-ecmwf-model for the detailed documentation of the specific IFS cycles.

[5]see Wedi (2014), Malardel and Wedi (2016) for more explanation about linear and cubic grids

There are two GTG turbulence forecast products: EDR predictions of CAT and MWT, respectively. For these forecasts the term CAT is used in a more general way and includes any diagnostic that successfully identifies large spatial gradients of atmospheric state parameters, regardless of their generation mechanism or their location with respect to clouds. Thus, the CAT diagnostic also includes other sources apart from Kelvin-Helmholtz instabilities such as e.g. convective systems. To forecast MWT, the GTG multiplies the CAT diagnostics with a parameter related to the terrain height and low-level wind speed. A detailed description of the GTG and its statistical forecast skill can be found in Sharman et al. (2006) and Sharman and Pearson (2017).

3.2.3 EULAG

EULAG (Prusa et al. 2008) [6] is a multi-scale computational model for the simulation of flows at different scales. It solves the anelastic equations (Prusa et al. 2008) and the equation for the TKE (Sorbjan 1996) in terrain-following coordinates. For the following studies, this model was used to analyze in principal the physical processes leading to the respective incidents. Due to the idealized approach of these simulations, it cannot be expected to find a one by one agreement between the in situ measurements and the simulations. For the two studies this model was set up in two different ways. For the study of the stall warning event EULAG is configured as a 3D model, while for the turbulence encounter above Iceland a 2D setup is used.

Table 3.2: Overview on the different EULAG setups for the case studies.

	Stall warning case study	Turbulence encounter
nx,ny,nz	336x240x76	3456x1x251
δx, δy, δz, δt	2.5 km, 2.5 km, 500 m, 5 s	200 m, - , 100 m, 2 s
topography	ETOPO 1	ECMWF
subgrid model	TKE	ILES

In the analysis of the stall warning event EULAG was setup to assess the magnitude of mountain wave-induced perturbations above the Apennine mountains. For this reason high-resolution, quasi-realistic numerical simulations with EULAG were employed. Here, a time period was selected after a quasi steady-state of the numerical integrations was achieved.

The computational grid is centered around the stall warning event (see Fig. 4.1) and comprises 336 x 240 x 76 grid points in zonal, meridional, and vertical dimension,

[6] http://www2.mmm.ucar.edu/eulag/

respectively. The horizontal resolution is 2.5 km, the vertical resolution is 500 m and the time step is 5 s. The topography is the global relief model (ETOPO1)[7] (Amante and Eakins 2009) (see Fig. 4.1) with a horizontal resolution of 1-arc minute, which is linearly interpolated onto the computational grid of EULAG.

The initial and boundary conditions of horizontal wind speed and potential temperature are given by single profiles of each, extracted from ECMWF spectrally truncated data up to wavenumber 21 (T21). These profiles are a zonal mean from 10°E to 11.5°E taken upstream of the stall warning event at 42°N and 0600 UTC. Figure 4.4 shows the horizontal wind profile which was used as input for EULAG. The initialization with a single, hydrostatically balanced state neglects large-scale meridional gradients such as the change in tropopause altitude (see Fig. 4.3 c and d). However, all perturbations can be attributed to the applied forcing of the flow across the Apennines. In the following and in the context of the EULAG simulations, perturbations are defined as the deviation from the initial conditions. The goal of this analysis is to understand whether vertically propagating mountain waves can induce wind and temperature perturbations at flight level and on horizontal scales comparable to the observations.

To analyze the generation mechanism of the strong turbulence encountered above Iceland (see Sec. 4.2), a 2D configuration of EULAG is employed where subgrid scale motions are treated via an implicit large eddy simulation (ILES) approach (Grinstein et al. 2007). For this case study a fine grid spacing is necessary to resolve the breaking of MWs and the associated turbulence. Therefore, a 2D setup was chosen to limit computational demands. Here, the computational grid is centered at the turbulence encounter and consists of 3456 x 251 data-points in the horizontal and vertical, respectively. The resolution is in the horizontal 200 m and 100 m in the vertical and the time step is 2 s. Viscosity and Coriolis force are disregarded in the applied setup. The sponge layer covers laterally 50 km and vertically the uppermost 8 km of the simulation domain with an absorber time scale of 200 s in the horizontal direction and 180 s in the vertical direction, respectively. Initial and boundary conditions are taken from ECMWF operational analysis at 12 UTC at an upstream position close to the coast of Iceland. Furthermore, the topography is taken from ECMWF and is interpolated onto the flight track. As for the stall warning case study again, perturbations are defined as the deviation from the initial conditions.

[7] See https://www.ngdc.noaa.gov/mgg/global/

4 Results

The results are presented in the following order. First a stall warning event of the research aircraft HALO on its transfer flight to Kiruna during the GW-LCYCLE II campaign is presented. This study is followed by a second study of a turbulence encounter of HALO above Iceland during the NAWDEX campaign.

4.1 Stall Warning Event

The results presented in this chapter have been published in Bramberger et al. (2018).

During its extended transfer flight to the operational base, the High Altitude and Long Range Research Aircraft (HALO) encountered a series of stall warnings above the Apennines, Italy on 12 January 2016. HALO flew from north to south at an altitude of 12.5 km (height above WGS84 ellipsoid), which was on that day at a FL of 410 kft (FL410, see Fig. 4.1). The pilots expected calm stratospheric flying conditions when, after a significant loss of the actual flown Mach number (Ma) within approximately 10 to 20 s, several stall warnings were issued by the autopilot system. Simultaneously, large variations in the along-track wind speed and static air temperature were observed. The flight situation was mitigated by the pilots who descended to a lower flight level.

Regarding the stall-warning event, we raise the following questions: Are the observed along-track variations in the meridional wind component and temperature responsible for initiating of the stall-warning event? Are these variations induced by mesoscale processes as propagating mountain waves or are they due to large-scale meteorological processes? Are the observed fluctuations accurately reproduced by high-resolution IFS forecasts and analyses? Which dominating processes can be identified based on higher-resolved mesoscale numerical simulations? Does the GTG predict mountain-wave induced turbulence associated with the forecasted fluctuations? Since HALO was equipped with a scientific payload, various high-quality sensors can be used to quantify the turbulence as well as the energy contained in the mountain waves. This opens the possibility to compare predicted energy dissipation rates with observed ones.

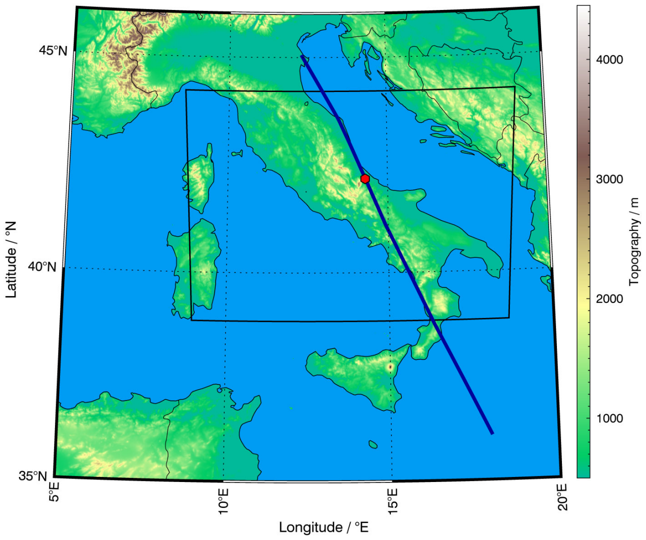

Figure 4.1: Flight track above Italy in blue. The red symbol shows the location of the stall warnings and the black box displays the computational domain of the EULAG simulations. Flight direction was from north to south. The topography is the global relief model ETOPO1 and was also used in the high-resolution numerical simulations.

4.1.1 Flight Incident

This section describes the sequence of events leading to several stall warnings based on the QAR and the BAHAMAS system of HALO (Fig. 4.2). During the incident the heading of the aircraft was 170° and therefore the meridional component of the horizontal wind is analysed.

HALO took off from Oberpfaffenhofen (48.08° N, 11.28° E) at 0755 UTC. The cruising altitude of the southbound leg on FL410 was reached over the Central Alps after about 30 min. To understand the sequence of events leading to the stall warning event, the initial situation of the aircraft and the changes in the atmospheric background conditions along the flight track are of major importance.

At about 0850 UTC, HALO was flying through an area with gradually decreasing static air temperature. The lower atmospheric temperature increased the air density, which in turn increased the lift of the wings and eventually the thrust of the engines (see sections 2.2.2 and 2.2.3). By this way, the aircraft accelerated and the autopilot reduced the angle of attack to keep the aircraft at constant speed. This means that HALO was already in an accelerated state (Fig. 4.2 point a) when it entered a region with large along-track gradients in both the static air temperature and meridional wind speeds.

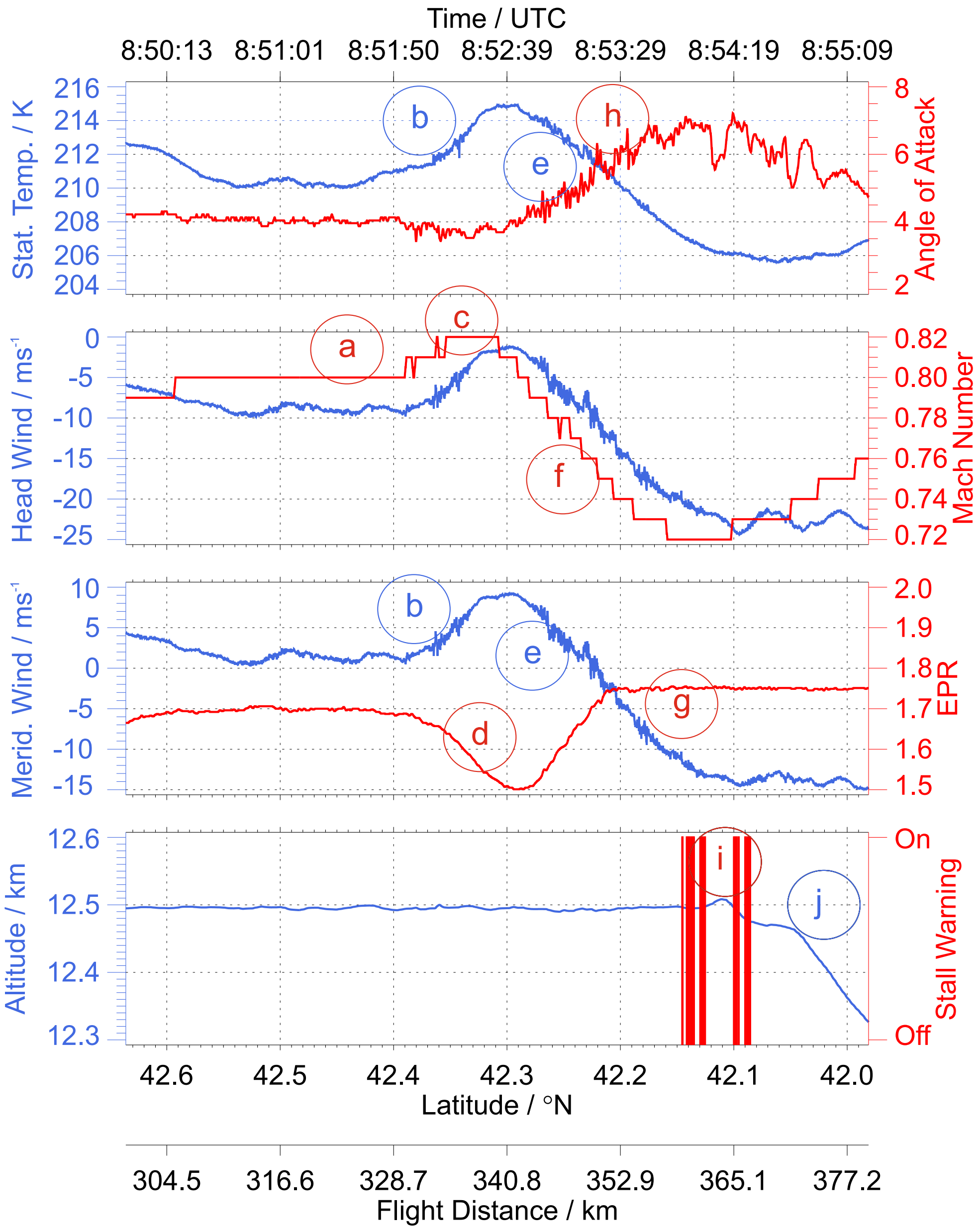

Figure 4.2: Sequence of events as recorded by HALO's Quick Access Recorder (QAR) and the BAHAMAS system. The top panel shows the static air temperature (blue) and the angle of attack (red). In the second panel the head wind (blue) and Mach number (red) are presented and the third panel shows the meridional wind (blue) and the engine power ratio (EPR, red). In the bottom panel the flight altitude (blue) and stall warning (red) are presented. The numbering (a)-(j) refers to the sequence of events leading to the stall warnings as mentioned in the text. QAR data comprises the angle of attack, Ma, EPR and stall-warning. BAHAMAS data include temperature, altitude, meridional- and head wind. (BAHAMAS data was kindly provided by Christian Mallaun and QAR was kindly provided by Kevin Raynor.)

While the angle of attack was being reduced, the atmospheric temperature increased by about 5 K at 0852 UTC (Fig. 4.2 point b) which reduced the air-density and, thus, the lift and thrust. At the same time, the meridional wind increased by about $8\,\mathrm{m\,s^{-1}}$ reducing the tailwind (negative headwind) from about $10\,\mathrm{m\,s^{-1}}$ to $2\,\mathrm{m\,s^{-1}}$ in this segment of the flight. As the actual flown Ma is proportional to the relative speed of the aircraft to the air (see Sec. 2.2.1), this increased the Ma to values larger than the appointed aircraft speed (Fig. 4.2 point c). Consequently, HALO's autothrottle reduced the thrust of the engines to decelerate the aircraft (Fig. 4.2 point d).

During the deceleration of the aircraft, the ambient atmospheric conditions changed again with a decrease in temperature by 9 K and a reduction in the meridional wind of about $20\,\mathrm{m\,s^{-1}}$ (Fig. 4.2 point e). The decrease of the meridional wind not only reduced its value but also changed the direction from southerly to northerly and consequently the magnitude of the tailwind of the aircraft increased by $20\,\mathrm{m\,s^{-1}}$. The reduced thrust together with the increased tailwind decelerated HALO gradually by 0.1 Ma within about 1.5 minutes thus reducing the margin to the stall speed (Fig. 4.2 point f). HALO's autothrottle adjusted to the situation and accelerated fully to the maximum engine power ratio (EPR) of 1.6 (Fig. 4.2 point g). However, this measure alone was not sufficient to regain the appointed aircraft speed due to the low air-density at this altitude and the time lag of the autothrottle system. As the auto pilot is programmed to preserve the flight altitude, it continued to increase the angle of attack to raise the lift of the aircraft (Fig. 4.2 point h). In the end, the angle of attack was large enough that flow could separate over the wings and the autopilot issued several stall warnings (Fig. 4.2 point i). The pilots mitigated the situation by switching off the autopilot and descending to a lower flight level in order to regain safe flight conditions (Fig. 4.2 point j). During this incident the pilots reported only light turbulence.

As documented above, the observed variations of ambient wind and temperature can explain the aircraft behaviour and the reactions of the autopilot system. These variations occurred at spatial scales of less than 100 km raising the question which processes did cause these changes in ambient conditions.

4.1.2 Meteorological Situation

On 12 January 2016, the day of the flight incident, north-westerly near-surface winds were present in the Mediterranean region (Fig. 4.3 a, b). This direction of the low-level flow was almost perfectly normal to the mean terrain crests. Flow channeling over the French Alps enhanced the horizontal winds over Corsica and Tuscany to speeds exceeding $10\,\mathrm{m\,s^{-1}}$. Thus, the direction and strength of the surface flow provided favorable low-level forcing conditions for the excitation of mountain waves in this region.

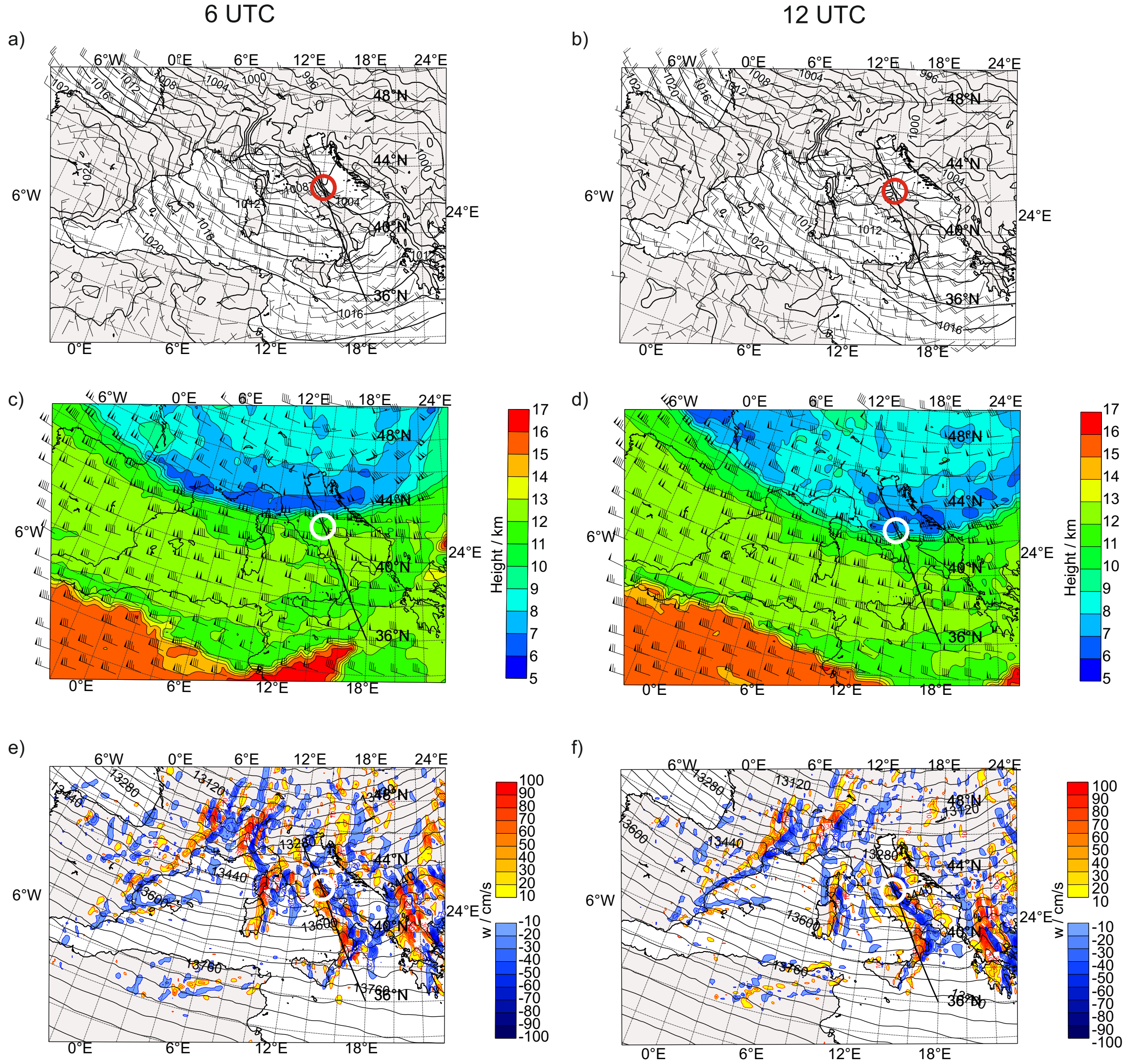

Figure 4.3: IFS cycle 41r2 analyses (a, b) of the mean sea level pressure (hPa, black lines) and the 10 m horizontal wind (m/s, barbs), (c, d) height of the dynamical tropopause (km, color shading) and the horizontal wind at the tropopause (cm/s, barbs), (e, f) and the vertical wind (cm/s, color shading) and geopotential height (m, solid lines) at 150 hPa valid for 06 UTC (a, c, e) and 12 UTC (b, d, f). The straight black lines show the flight track of HALO's transfer flight and the circles indicate the position of the stall-warning event. Flight direction was from north to south.

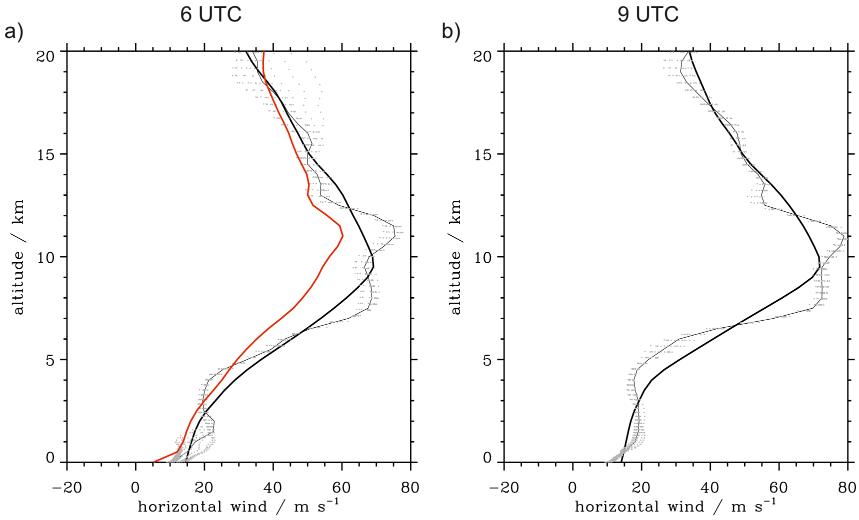

Figure 4.4: Vertical profiles of the horizontal wind speed at 42°N for 0600 UTC (a) and 0900 UTC (b) based on IFS cycle 41r2 forecasts. Thin lines are calculated on the 500 m vertical grid points and the thick lines are the vertical mean over a 10 km boxcar average. The gray dots show the variability between 10°E and 11.5°E. The red profile at 06 UTC shows the T21 profile calculated on the 500 m vertical grid points used to initialize EULAG.

In the upper troposphere, a large-scale trough was located above Northern Italy and mid-Europe leading to a sharp north-south gradient of the height of the dynamical tropopause (Fig. 4.3 c, d). An elongated tropopause fold together with the strong polar front jet ($U \approx 80\,\mathrm{m\,s^{-1}}$) extended zonally from Southern France to Italy along about 42 °N. During the flight of HALO, this meteorological system propagated slowly south-eastward. Thus, HALO's flight track at FL410 passed from the stratosphere in the north, across the tropopause over Northern Italy into the troposphere above Southern Italy (Fig. 4.3 c, d).

The alignment of lower tropospheric winds and of the polar front jet favored the vertical propagation of the excited mountain waves in two ways: first, the background horizontal wind speed increased with altitude (Fig. 4.4) and, second, there was very little directional shear up to the lower stratosphere. That way, no critical layer attenuated the propagation of mountain waves by non-linear processes such as wave breaking. Between 0600 UTC and 0900 UTC maximum wind speeds increased only slightly from $76\,\mathrm{m\,s^{-1}}$ to $78\,\mathrm{m\,s^{-1}}$. Assuming a mean (from surface to the tropopause level) background wind of approximately $30\,\mathrm{m\,s^{-1}}$ it takes hydrostatic mountain waves with $\lambda_h \approx 50\,\mathrm{km}$ about 0.75 hours to propagate from the surface to an altitude of 15 km. Therefore, background conditions for the vertical propagation of hydrostatic mountain waves into the lower stratosphere can be assumed steady within this time

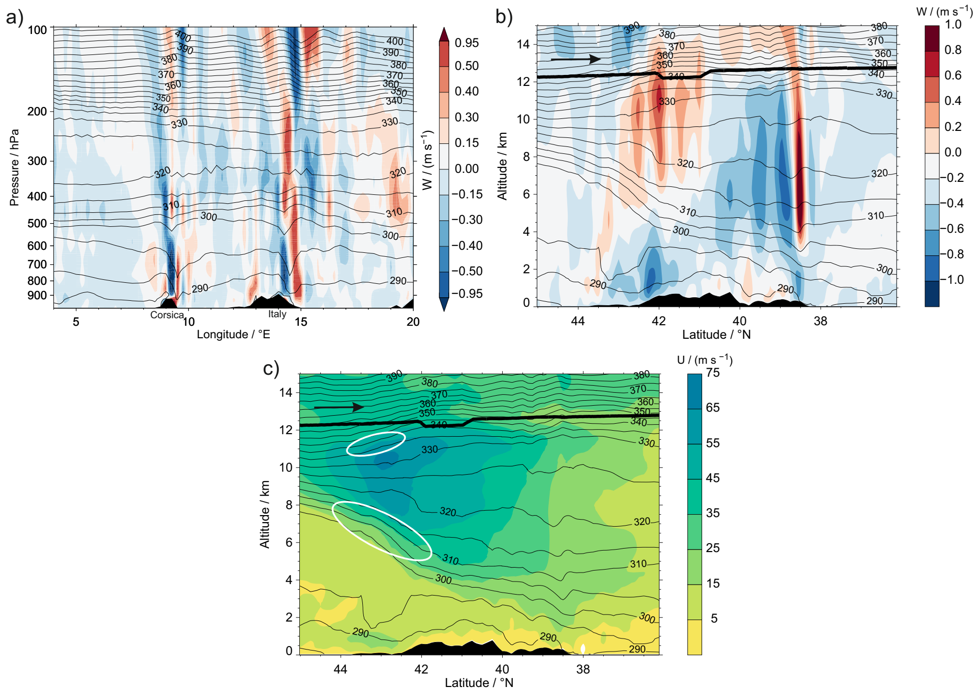

Figure 4.5: Vertical cross-sections of the vertical wind along 42 °N (a) and along the flight track (b). The horizontal wind along the flight track is shown in (c). The white circles highlight regions with largest vertical shear. The thin black contour lines are the isentropic surfaces in K with an increment of 5 K and the black shaded regions correspond to the surface terrain. The straight black lines in (b) and (c) show HALO's flight track and the black arrow indicates the flight direction. Plot (a) is valid at 12 UTC. Data in (b) and (c) were interpolated both in time and horizontal space to the flight track.

frame.

High-resolution IFS analyses of the vertical wind reveal coherent waves at the 150 hPa pressure level over the French Alps, Corsica, and the Apennines, respectively (Fig. 4.3 e, f). These wave patterns are stationary with respect to the particular mountain ranges. Due to their stationary character and the hydrostatic design of the IFS, they can be attributed to vertically propagating hydrostatic mountain waves. Correspondingly, undulations of the geopotential height as depicted in Fig. 4.3 e, f are related to these mountain waves. Simulated mountain wave amplitudes of the vertical wind decrease from about 1 m s^{-1} to about 0.5 m s^{-1} from 06 UTC to 12 UTC. According to these high-resolution IFS analyses, HALO first encountered a downdraft related to the mountain waves. Further south above the Apennines, it entered an updraft. Both wave encounters happened laterally with respect to the phaseline of the mountain waves, i.e. almost perpendicular to the mean wind.

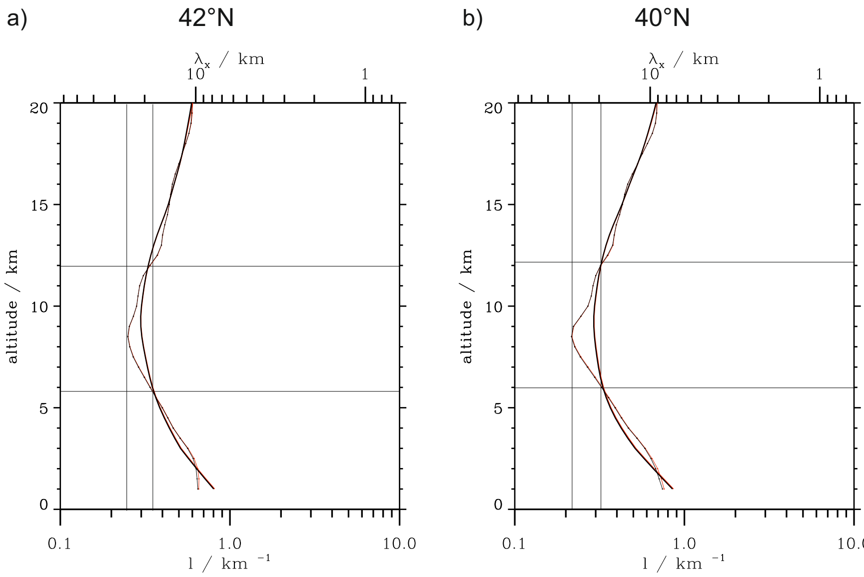

Figure 4.6: Vertical profiles of the Scorer parameter based on ECMWF T21 forecasts at 42°N (a) and 40°N (b) for 0900 UTC. Thin lines with dots are calculated on the 500 m vertical grid points and the thick lines are the vertical mean over a 10 km boxcar average. Red profiles are calculated with the zonal wind component only (u) and the black profile with the horizontal wind ($U = \sqrt{u^2 + v^2}$).

In order to better understand the structure of the mountain waves, panels a and b of Figure 4.5 juxtapose vertical cross sections along 42 °N and along the flight track. Both panels span the same vertical range. Figure 4.5 a reveals hydrostatic mountain waves above Corsica and Italy: phase lines are located directly above the obstacles and extend from the troposphere to the stratosphere indicating vertical propagation for these mountain waves. The cross-section in Fig.4.5 b shows adjacent down- and updrafts extending along HALO's flight track related to these mountain waves.

Temporal and spatial interpolation to the flighttrack reveals that the temperature decreased gradually from about 213 K to 210 K during the stall warning event (see Fig. 4.7). Also, the meridional wind speed decreased by about 9 m s^{-1} and, additionally, changed its direction from a southerly to northerly direction.

Analysis of the Scorer parameter indicates that gravity waves with horizontal wavelengths λ_h larger than ≈25 km at 42°N are able to propagate freely through the troposphere up to the lower stratosphere (Fig.4.6). Further to the south at 40°N, λ_h increases and only gravity waves with scales larger than 29 km are non-resonant. The vertical profiles of the Scorer parameter further suggest that gravity waves with 18 km $\lesssim \lambda_h \lesssim$ 29 km are trapped in a layer between 6 km and 12 km altitude. All gravity waves with $\lambda_h <$ 18 km seem to be evanescent in the troposphere and should not be able to reach the tropopause. Between 0600 UTC and 0900 UTC, the background conditions for gravity wave propagation remain steady (not shown).

The polar front jet is not only a favorable guide for the vertical propagation of the mountain waves, upper-level fronts are also regions known to generate turbulence due to strong vertical shear of horizontal wind (Dutton 1969, Delay and Dutton 1971, Kennedy and Shapiro 1975, Shapiro 1976). Therefore, the position of HALO's flight track relative to the polar front jet is depicted by a vertical cross-section along the flight track (Fig. 4.5 c). With a flight altitude of about 12 km, HALO was well above the jet streak of the polar front jet and also outside the regions containing the largest vertical shear. Pilot‘s reports about merely light turbulence are a further indication that HALO was outside the regions of CAT generation related to upper-level fronts.

4.1.3 Mountain Wave Characteristics

Knowing the meteorological situation we can attribute the regular shape of the up- and downdrafts in the in-situ wind measurements to the mountain wave activity above the Apennines (Fig. 4.7). Strong gradients are present in all parameters in the area of the stall warning event (gray shading in Fig. 4.7). In this region peak-to-peak amplitudes in the measured vertical wind reach $4\,\mathrm{m\,s^{-1}}$ and in the meridional wind up to about $23\,\mathrm{m\,s^{-1}}$. Also the temperature measurement reveals pronounced peak-to-peak amplitudes with values up to 9 K during the stall warning event. Analysis of the phase relations especially of the vertical wind and temperature in the area of the stall warning event, reveals that these are not perfectly following linear wave theory. In this area, the larger scale pattern of the vertical wind is superimposed by small scale structures. This might be due to turbulence induced by non-linear processes, e.g., by breaking mountain waves. South of the stall warning event, observed amplitudes are less pronounced in all parameters when HALO was flying almost along the phase lines of the mountain waves. Between 39°N and 38°N, again increased, isolated peaks are revealed in all parameters with peak-to-peak amplitudes up to about 6 K in the temperature and $10\,\mathrm{m\,s^{-1}}$ in the meridional and zonal wind component, respectively. In the vertical wind peak-to-peak amplitudes of up to $4\,\mathrm{m\,s^{-1}}$ were observed.

The IFS data interpolated in time and space to the flight track reproduce the large scale pattern along the flight track very well in all observed parameters. However, the small-scale structures and the sharp spatial gradients, especially, in the stall event area, were not captured by the IFS. This discrepancy indicates that the IFS underestimates the amplitudes and horizontal wavelengths of the vertically propagating mountain waves.

For this study, the fluxes defined in Eqs. 3.1 and 3.2 are only calculated after the stall warning event, south of 40.7° N, when stable flight conditions were re-established. This was done in order to include as many mountain wave scales as possible in our analysis

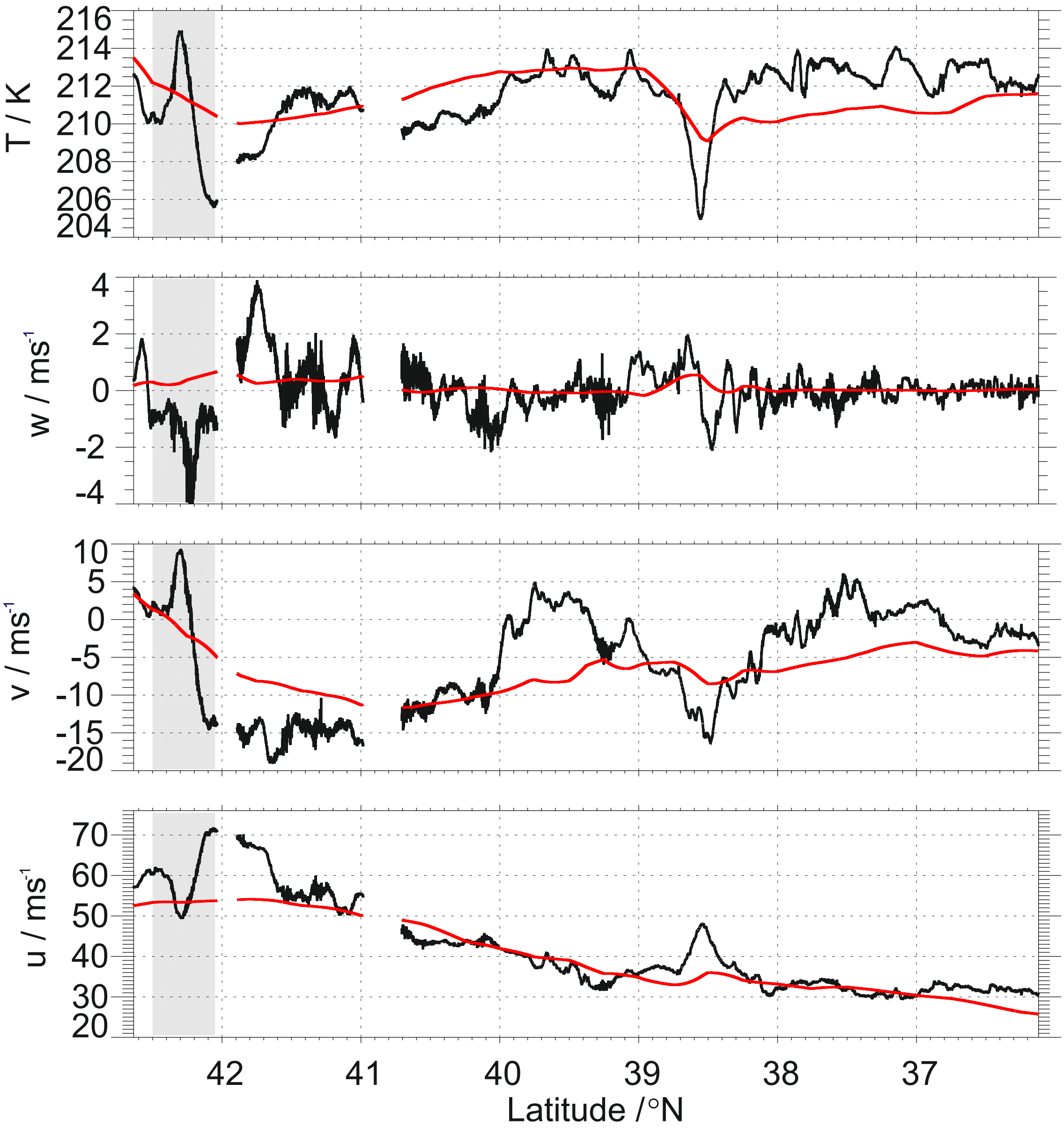

Figure 4.7: In-situ measurements (black) and IFS cycle 41r2 forecasts (red) of: temperature (upper panel), vertical wind (second panel from top), meridional wind (third panel from top) and zonal wind (bottom panel). IFS forecasts have been interpolated both in time and space to the flight track. The gray shading highlights the area of the stall-warning event and the gaps are related to the altitude changes due to the stall warning event.

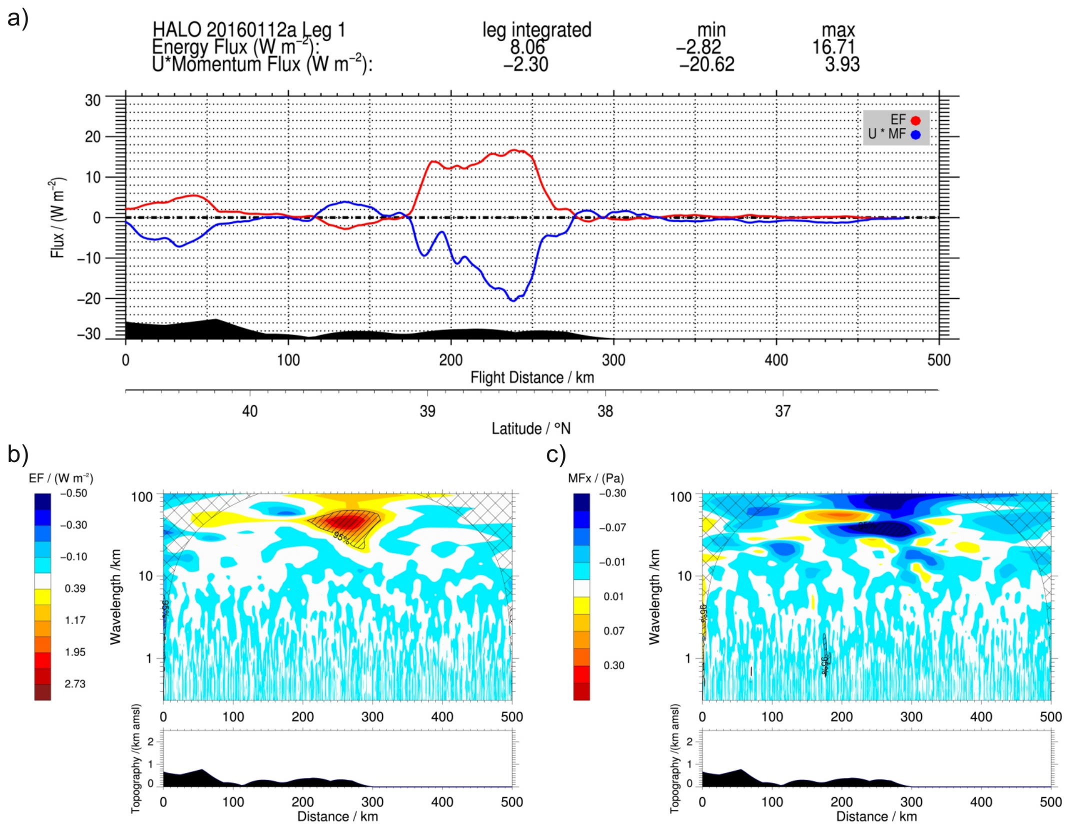

Figure 4.8: Subleg-integrated vertical energy flux (red) and subleg-integrated energy flux derived from horizontal momentum fluxes (blue) along the flight leg after the stall-warning event (a). Co-spectra of vertical energy flux (EF_z, b) and zonal momentum flux (MF_x, c) along the same leg segment.

as the horizontal distance of the stall warning event would have limited the maximum observable horizontal wavelength.

An analysis of the vertical energy flux EF_z based on the in-situ measurements along the flight track south of the stall warning event reveals upward propagating mountain waves with a local maximum of 18.1 W m^{-2} and a leg-integrated value of $EF_z \approx 8$ W m^{-2} (Fig. 4.8 a). The wavelet analysis of EF_z shows that the horizontal scales λ_h of the dominant flux-carrying waves range between 20 km and about 65 km (Fig. 4.8 b). Consistent with the upward energy transport and thus the Eliassen-Palm relation (Eq. 2.22), the energy flux calculated by the scalar product of horizontal wind and the momentum fluxes is mostly negative with a minimum value of -23.3 W m^{-2} and a leg-integrated value of -2.3 W m^{-2} (Fig. 4.8 a). As the ambient horizontal wind is mainly zonally oriented, we present the spectral analysis of the zonal momentum flux MF_x. Horizontal wavelengths for the dominant fluxes range from $\lambda_h \approx 30$ km to about 65 km (Fig. 4.8 c) in agreement with predictions of the Scorer parameter and are associated with westward (negative) zonal momentum fluxes. In order to oppose strong downwind advection by the mean ambient flow, mountain waves need to propagate upwind through the atmosphere (Smith et al. 2016). Our analysis reveals this horizontal upwind propagation with the negative zonal momentum fluxes, thus, suggesting westward propagating mountain waves that are balancing the mean flow.

In order to check if the observed mountain waves at flight level can be described by linear theory, the Eliassen-Palm relation (Eq. 2.22) is applied. The subleg-integrated fluxes of both the EF_z and EF_{zM} are qualitatively well anti-correlated for the portion of the flight leg south of the stall-warning event (starting at 40.7 °N in Fig. 4.8 a). However, between 40.7 °N and 38.5 °N magnitudes of EF_z and EF_{zM} differ up to about $4\,\mathrm{W\,m^{-2}}$ in the mean. For the leg-integrated fluxes the values are off by a factor of 3.5. That way, both the subleg-integrated and the leg-integrated fluxes point to either wave trapping or non-linear processes, e.g. as wave-breaking. Furthermore, the spectral analysis (Fig.4.8 b,c) reveals that the anti-correlation of the fluxes according to the Eliassen-Palm relation is only valid for horizontal wavelengths $\lambda_h \gtrsim 30$ km implying again that modes with $\lambda_h < 30$ km are either trapped or involved in non-linear processes.

4.1.4 Turbulence Measurements and Forecasts

In-situ Turbulence Analysis

Along-track profiles of TKE derived from in-situ wind measurements as described in Sec. 3.1.5 are shown in Fig. 4.9 a. Here, we show TKE calculated for sublegs ranging between 20 km and 4 km to analyze how much of the variances due to mesoscale motions have been removed by assuming a 4 km window. As expected, the TKE contained in larger scales (subleg length of ≈ 20 km) is greater than in the smaller scales (4 km). Furthermore, the small difference in TKE values of $0.03\,\mathrm{m^2\,s^{-2}}$ between the 8 km and 4 km subleg lengths (in the gray-shaded part) suggests that the largest contributions to the variance due to mesoscale perturbations are removed around this scale. Here, we perform the turbulence analysis with the 4 km subleg lengths as we are mostly interested in turbulent scales between about 300 m and 1 km which affect aircraft the most (MacCready 1964, Vinnichenko et al. 1980, Hoblit 1988, Sharman et al. 2014).

In the northern part of the leg and before the stall events almost no TKE is contained in the 4 km subleg lengths. Further south, TKE values increased to about $0.35\,\mathrm{m^2\,s^{-2}}$ when HALO entered the region of the stall-warning event (gray-shaded area in Fig. 4.9 a). South of the stall-warning event, TKE values increased only little up to $0.4\,\mathrm{m^2\,s^{-2}}$ and decreased afterwards. These TKE values are smaller than the nominal threshold value of $0.6\,\mathrm{m^2\,s^{-2}}$ used by Strauss et al. (2015) to indicate light turbulence .

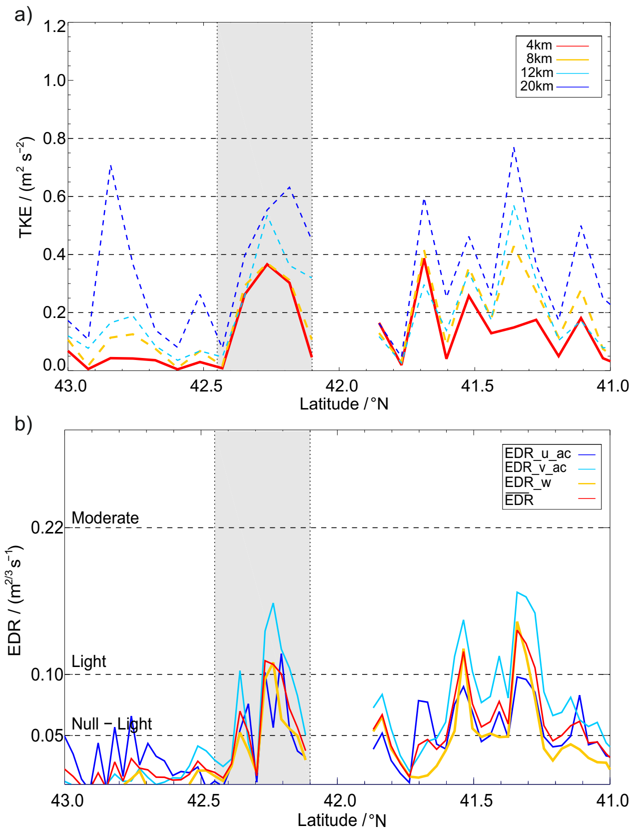

Figure 4.9: Turbulent kinetic energy (TKE) calculated for different subleg lengths (a). Eddy dissipation rate (EDR) for the three wind components and the log-mean of all wind components ($\overline{EDR}$) (b). The gray shading highlights the area of the stall-warning event and the gap in the data is related to the descent after the stall-warning event.

Furthermore, the inspection of the EDR_i-profiles (calculated from in-situ measurements) for 4 km subleg lengths reveals a similar structure as the TKE profile shown above: almost no turbulence in the northern part of the leg and increasing turbulence in the updraft region of the mountain wave and within the elongated mesoscale temperature anomaly (Fig. 4.9b). The individual EDR_i values show scatter around the geometric-mean $\overline{EDR}$ which could come from, e.g., anisotropic turbulence due to stratification of the atmosphere or uncertainties due to deviations from the -5/3 Kolmogorov slope. In contrast to Strauss et al. (2015), our analysis reveals that the transverse $EDR_{v_{ac}}$ component is in the mean by a factor of 1.3 larger than the longitudinal $EDR_{u_{ac}}$. Overall, in accordance with the small TKE values the computed EDR-values indicate only light turbulence during this flight segment confirming the pilot reports. Turbulence thresholds used in this study are for a medium-size aircraft, which might be a little high for a light aircraft such as HALO (Sharman et al. 2014).

Turbulence Forecast

For our study turbulence forecasts of the GTG are compared to the in-situ aircraft data. To be consistent with previous studies (e.g. Sharman et al. 2014, Sharman and Pearson 2017), only the EDR derived from vertical wind measurements is taken into account. Moreover, as seen in Fig. 4.9b, the EDR_w values mostly fall in the same turbulence category as the $\overline{EDR}$.

Above Italy, the GTG predicts light to moderate turbulence connected to the strong polar front jet and mountain wave activity (Fig. 4.10a-b). In particular in the region of the stall-warning event, moderate turbulence is forecasted. Compared to the in-situ measured EDR, the forecasted EDR values are higher (see Fig. 4.10c) and the spatial structure is less intermittent. The mean difference between the EDR for CAT only and the measured EDR is with $0.14\,\mathrm{m^{2/3}\,s^{-1}}$ slightly larger than the mean difference between EDR for MWT and the measured EDR of $0.13\,\mathrm{m^{2/3}\,s^{-1}}$. This result reflects the tendency of overpredicting by the GTG as was also found in Sharman and Pearson (2017). However, particularly above Southern Italy, the measured EDRs are mostly in the same turbulence-severity category ('light') as the predicted EDRs.

4.1.5 High-resolution Numerical Simulations

Simulations with the non-hydrostatic model EULAG are used to study the magnitude of mountain wave-induced gradients in the region of the stall warning event and were kindly provided by Henrike Wilms. These simulations reveal coherent, stationary structures in the perturbations of the potential temperature as well as the meridional and vertical wind fields above Italy (Fig. 4.11a,b,c). The simulations also indicate that mountain waves with larger horizontal wavelengths dominate the meridional wind and temperature perturbations, while smaller-scale mountain waves prevail in the vertical wind. Amplitudes in the meridional wind field are about $9\,\mathrm{m\,s^{-1}}$ and about $4\,\mathrm{m\,s^{-1}}$ in the vertical wind speed. The perturbations of the potential temperature reach values of up to 7 K.

In the region of the stall warning event (Fig. 4.11, black circle), short-scale fluctuations with large amplitudes are present in all three parameters. The profiles in Fig. 4.12 show a decrease in the meridional wind speed from about $10\,\mathrm{m\,s^{-1}}$ to $-8\,\mathrm{m\,s^{-1}}$ within a horizontal distance of approximately 40 km at the altitude range of the flight track. The distance between the maximum and minimum values in the meridional direction is larger by about 10 km compared to the observations. The peak-to-peak amplitude, on the other hand, is with $18\,\mathrm{m\,s^{-1}}$ slightly smaller than the observed one of about $23\,\mathrm{m\,s^{-1}}$ but higher than the amplitude provided by the IFS forecasts. The potential temperature decreases in the same area by about 10 K.

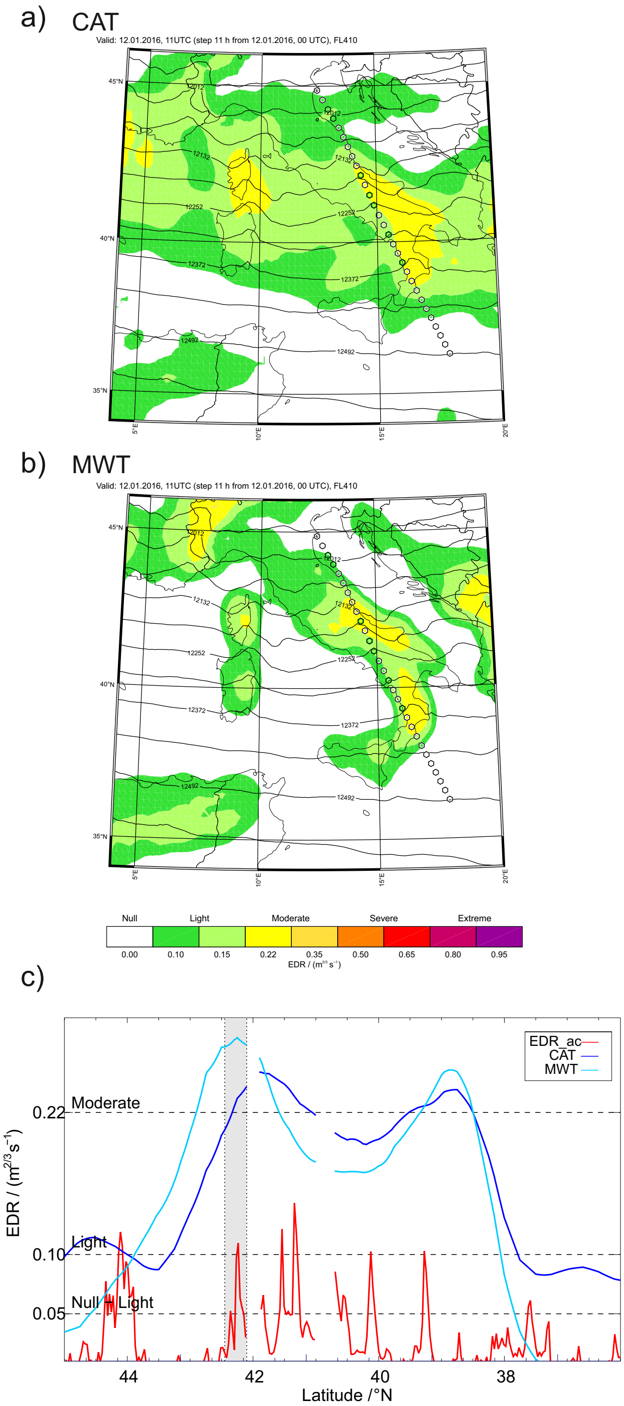

Figure 4.10: GTG turbulence forecasts regarding CAT (a) and MWT (b) at FL410 together with the geopotential height (m, black solid lines). The line of circles shows the color-coded severity of turbulence resulting from the maximum value over ten EDRs calculated from in-situ vertical wind measurements along the flight leg. (c) shows a comparison of EDR derived from vertical wind measurements and GTG forecasts interpolated to the flight track in space and time along the flight leg.

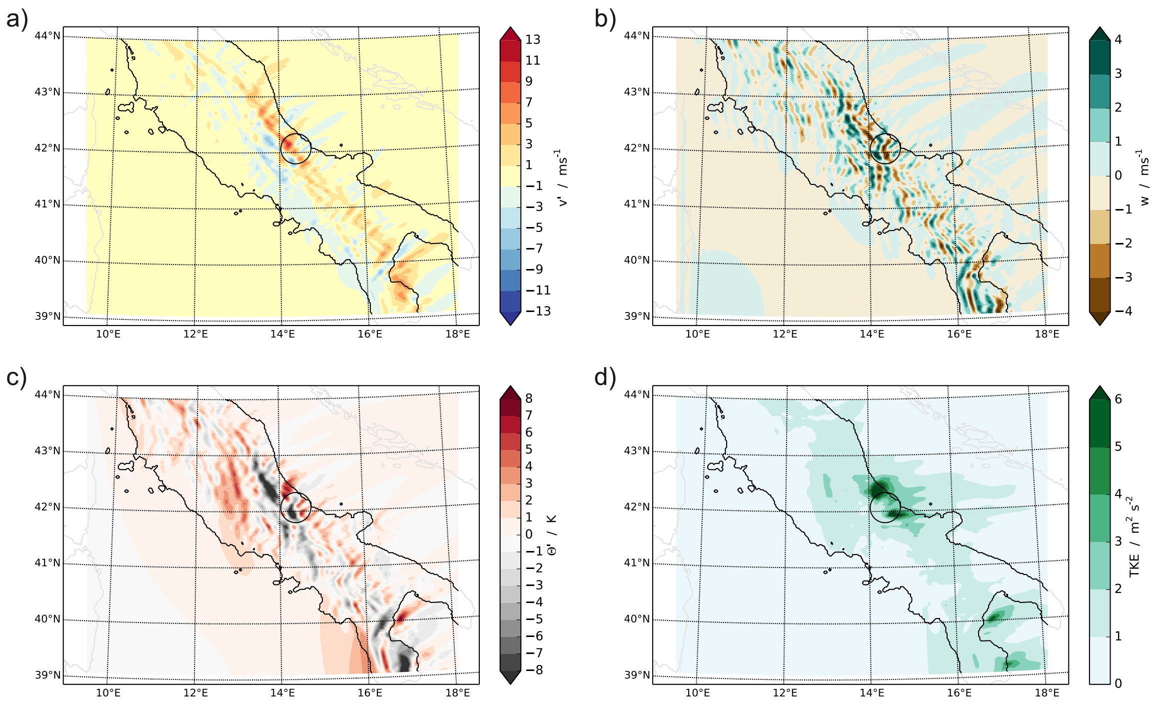

Figure 4.11: Meridional wind perturbations (a), vertical wind (b), temperature perturbations (c) and TKE (d) as simulated by EULAG at 12.5 km altitude. The black circle indicates the position of the stall warning event with a radius of 30 km.

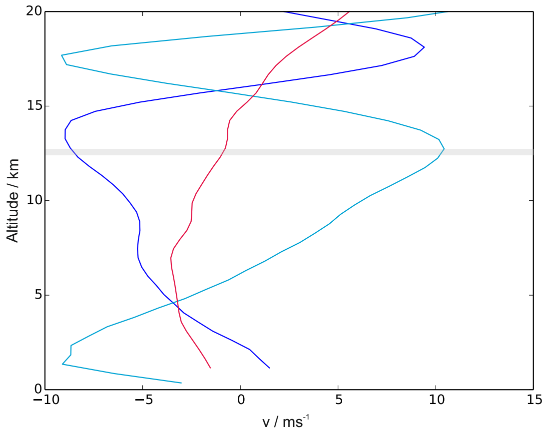

Figure 4.12: Vertical profiles of the meridional wind at the positions of the maximum or minimum meridional wind perturbation within the black circle shown in Fig. 4.11(blue). The red line shows the background meridional wind profile and the gray shading highlights the altitude of the flight track. The spatial horizontal distance between the blue profiles is about 40 km.

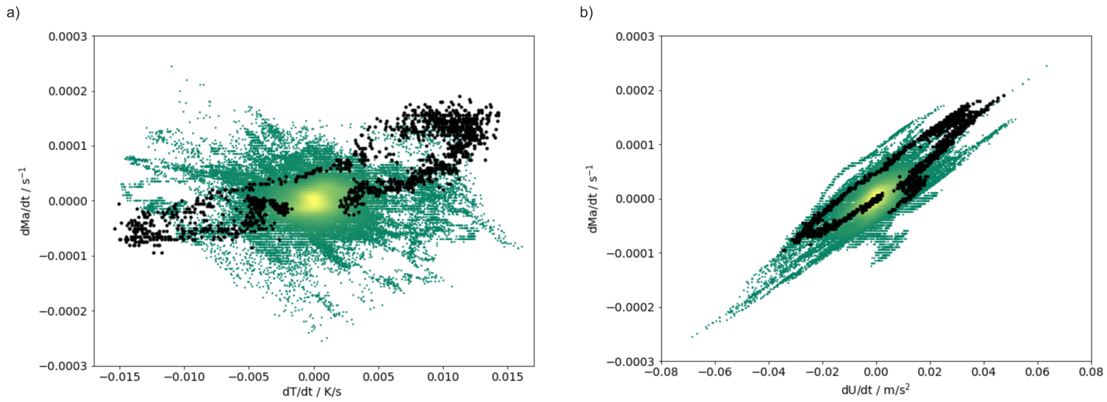

Figure 4.13: Correlation of changes in the flown Mach number to changes in the temperature (a) and the horizontal wind along the flight track (b). Color coding refers to density of points (bright color: high density, darker color: less density). Black dots refer to values during the stall warning event. The presented data are HALO in-situ measurements taken from two separate flights under different conditions.

Enhanced TKE (Fig. 4.11 d) suggests partial breaking of smaller scale mountain waves above Italy.

4.1.6 Impact of Temperature and Horizontal Wind on Aircraft Velocity

A closer inspection of Fig. 4.2 reveals a high correlation of atmospheric temperature and flown Ma. Indeed, based on the fundamental definition of Ma as ratio of aircraft velocity and speed of sound, where the speed of sound has a temperature dependence, temperature modulations could be interpreted as main driver for changes in Ma. However, a different way to compute Ma is given by Eq. 2.27.

To answer the question which atmospheric parameter dominantly impacts aircraft speed, the correlations between the changes of measured temperature and horizontal wind speed with changes of Ma are calculated for the two presented flights. In total a number of 66402 data points is taken into account for this analysis.

Fig. 4.13 shows the correlation between changes in aircraft speed (Ma) and changes in temperature (a) and along-track wind speed (b), respectively. The black dots refer to data points during the stall warning event. Even though there is a clear correlation between changes in Ma and changes in temperature during the stall warning event, it is a rare coincidence, as in general there is no correlation. This is reflected in the low magnitude of 0.056 of the correlation coefficient (including all data points). Instead, changes in the Ma are related to changes in the along-track horizontal wind speed. Here, the magnitude of the correlation coefficient is 0.621, respectively.

4.1.7 Discussion and Conclusion

This case study reveals that mountain-wave induced variations of ambient along-track wind and temperature were responsible for the initiation of the encountered stall warning event encountered by the research aircraft HALO. With the knowledge of atmospheric background conditions, it was possible to reconstruct the aircraft's behaviour and the reactions of the autopilot system.

Strong northwesterly surface flow excited vertically propagating mountain waves above the Apennines. Due to the zonal alignment of the polar front jet with the low-level winds, these mountain waves could propagate vertically into the stratosphere without significant dissipation and attained large amplitudes at FL410. Mountain-wave induced meridional wind perturbations with comparable amplitudes in high-resolution EULAG simulations occur in the same area as the observed ones. The associated decrease of meridional wind by about $23\,\mathrm{m\,s^{-1}}$ (as seen in in-situ data) translated into a loss of about 0.1 Ma in aircraft speed. At this time, HALO flew in the stratosphere at about 12.5 km altitude, an altitude region where the margin to the stall speed in the coffin corner is small. Although the decreasing temperature increased the density and thus the lift and thrust of the aircraft, this change was not large enough to compensate the effect of the along-track wind component on aircraft speed. Therefore, the deceleration of the aircraft through the sudden and strong change in the along-track wind reduced the margin to the stall speed making it necessary to accelerate the aircraft by means of full engine thrust and increased angle of attack. However, engine thrust is limited by the generally rather low air density at these altitudes and several stall warnings occurred. A descent to a lower flight level was the only measure to regain stable flight conditions.

Generally, high-resolution IFS forecasts reproduce the large-scale flow in the vicinity of the observations, especially in the meridional wind speed and the temperature (Fig. 4.7). However, the observed perturbations in all presented parameters could not be reproduced in the area of the stall warning event because of inadequate resolution. Therefore, the forecasts also underestimate the gradients in this region compared to the measured ones by ~18% of the observation for the temperature and by ~6% of the meridional wind, respectively. That way, the comparison suggests that large-scale structures, as e.g. an upper-level front, resolved in the IFS are not the dominant source of the observed strong gradients during the stall warning event. Their largest gradients occurred at lower altitudes. High-resolution numerical simulations with EULAG, on the other hand, could reproduce the reversal of the direction and the decrease of the meridional wind speed with a similar magnitude as the observations. Therefore, we attribute the observed changes in ambient atmospheric conditions leading to the stall warning event mainly to vertically propagating mountain waves above the Apennines.

The presence of significant mountain wave activity is established by large leg-averaged vertical energy flux of $EF_z \approx 8\,\mathrm{W\,m^{-2}}$ derived from the high-quality in-situ measurements of HALO. During the DEEPWAVE campaign, only four out of 26 research flights at stratospheric altitudes show EF_z values exceeding $5\,\mathrm{W\,m^{-2}}$ (Smith et al. 2016). During the GW-LCYCLE I campaign, Wagner et al. (2017) found only one leg with $EF_z > 5\,\mathrm{W\,m^{-2}}$. The majority of the flux-carrying horizontal wavelengths range between $\lambda_h \approx 20\,\mathrm{km}$ and about 65 km. Interestingly, this range lies in the intermediate scale (as defined by Smith et al. (2016)) which was the dominant scale in strong mountain wave cases during the DEEPWAVE campaign (Smith et al. 2016). Hence, the comparison to former gravity wave campaigns such as DEEPWAVE and GW-LCYCLE I suggests that the encountered mountain wave event on 12 January 2016 was an unusually strong event.

For $\lambda_h > 30\,\mathrm{km}$, the Scorer parameter indicates freely propagating mountain waves and a nearly linear character can be attributed to those waves as additionally the Eliassen-Palm relation is fulfilled in these scales. It was the favorable zonal alignment of the low-level forcing to the wave guide of the polar front jet which was responsible for the nearly linear vertical wave propagation.

However, our mountain wave analysis indicates that not all wave modes propagated without dissipation through the atmosphere. Especially the Scorer parameter suggests that waves with $\lambda_h \lesssim 29\,\mathrm{km}$ are either trapped or evanescent (Fig 4.6). This contributes to the fact that the Eliassen-Palm relation is not completely fulfilled for leg-averaged fluxes. The scale analysis additionally points at either trapped or partially breaking mountain waves by showing anti-correlated fluxes only for $\lambda_h > 30\,\mathrm{km}$. In the in-situ measurements, particularly the vertical wind speed is superimposed by small-scale structures. Together with the production of TKE in the EULAG simulations, the observations indicate the presence of turbulence. The GTG forecasts moderate turbulence regarding both CAT and MWT, but with slightly larger EDR values for the MWT in the region of the stall warning event. As HALO's flight track was located outside the region of strongest shear in the polar front jet and the TKE in EULAG is related to non-linear processes in the mountain wave field, we attribute the observed light turbulence to breaking mountain waves or other small-scale instabilities.

Due to the processes described above, our case study reveals that stratospheric mountain waves pose a serious hazard, in particular to modern, high-flying aircraft. The mountain waves generate mesoscale stratospheric horizontal wind and temperature anomalies resulting in large horizontal gradients of these parameters. If aircraft fly through them they encounter a sequence of accelerating and decelerating anomalies. Depending on its type, the aircraft's speed changes due to the modulation of the horizontal wind field and incidents such as the one described in this study might occur. So far, turbulence is considered among the major hazards for commercial air traffic flying between 8 and 14 km altitudes (e.g. Lane et al. 2009, Sharman et al. 2012b, Williams 2017). Therefore, it is only natural to draw the attention to breaking mountain waves and their induced turbulence. Thus, e.g. in a former field campaign flight planning for the ER-2 aircraft focused on the forecast of mountain waves turbulence which means whenever laminar mountain waves were present, the aircraft was allowed to fly (Eckermann et al. 2006). Yet, the present study shows that turbulence did not play a major role in the creation of the strong horizontal meridional wind and temperature gradients leading to the stall warnings but was instead entirely attributable to vertically propagating near-laminar mountain wave oscillations alone. This is an important aspect for flight planning especially of high-flying aircraft such as e.g. the ER-2 or the Global Hawk.

Accumulated anecdotal experience of SWISS pilots Fusina, Fabian and Gerber, Martin suggests that encounters like the one described in this study, are not uncommon above mountainous terrain. Also at higher altitudes ($\approx$ 20 km) encounters with propagating mountain waves were reported by the ER-2 aircraft and caused e.g. vertical displacements of about 1.5 km (Bacmeister et al. 1990, Chan et al. 1993, Leutbecher and Volkert 2000). However, due to its design, the ER-2 is highly susceptible to changes in the ambient atmosphere. Today, the common flight level for commercial air traffic is at FL 380 where the margin in the coffin corner is larger than in the analyzed event. But with the projected increase in passenger numbers in the next 20 years (IATA 2017), flight level altitudes might increase due to increased air traffic density. This in turn would on the one hand reduce the margin in the coffin corner for aircraft. On the other hand, an increase in mountain wave amplitudes can be expected due to the decreasing density with altitude which could lead to stronger gradients in temperature or the horizontal wind and thus stronger impacting an aircraft flying at FL430 than one flying at FL380. As global flight routes like e.g. the North-Atlantic tracks often lead across mountainous terrain, we suggest to include information on propagating mountain waves in the flight planning process or in the significant weather charts.

4.2 Turbulence Encounter of HALO during NAWDEX

The multi-purpose research flight number 10 (RF10) on 13 October 2016 during the NAWDEX campaign took HALO along the edge of an upper-level ridge from Iceland, across Spitsbergen to Norway and back to Iceland. This flight was designed to observe several atmospheric phenomena as e.g. CAT, tropopause structure and MWs. Therefore, the flight also included two legs above Iceland where one was intended to follow a satellite overpass and the other to observe MWs. Those two flight legs were coordinated with the French research aircraft Falcon from Safire.

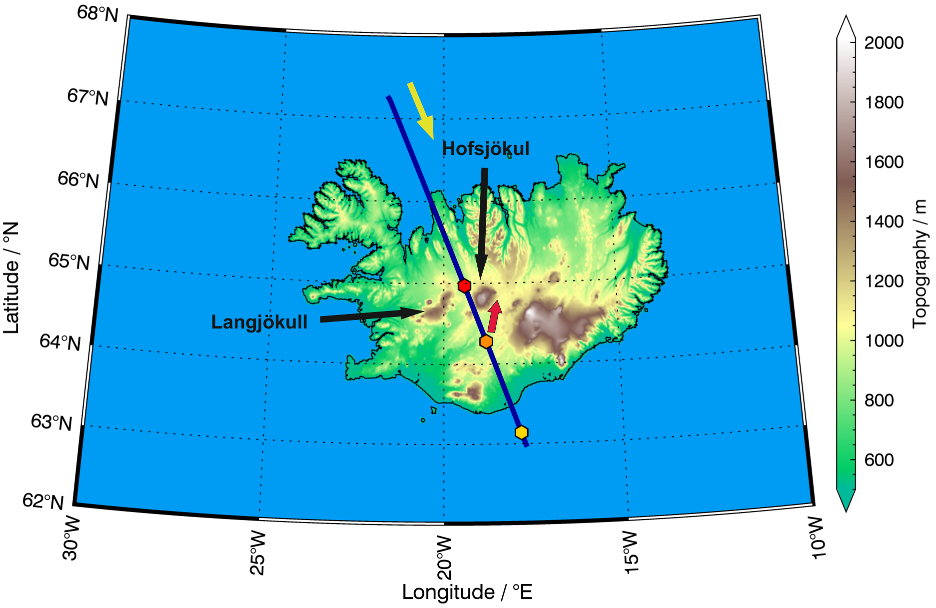

Figure 4.14: HALO's flight track above Iceland. Red dot shows the position of the turbulence encounter, the orange dot refers to the position where the photograph (Fig. 4.15) is taken and the yellow dot indicates the position of the upstream profiles. The yellow arrow indicates the flight direction from north to south and the red arrow the approximate viewing direction of the photograph (Fig. 4.15), respectively. The French Falcon flew nearly simultaneously along the same track at an altitude of 11.8 km (2 km underneath HALO).

However, during it's first passage over Iceland (on it's way to the planned MW-leg, Fig. 4.14), HALO encountered "strong" turbulence above Iceland. Consequently, due to flight safety reasons the intended MW-leg was skipped and HALO returned to Keflavik afterwards. Regarding the incident the commanding pilot, Steffen Gemsa, reported:
"*So we are on the flight over Iceland, coming from the North, at flight level 430. The turbulences were so strong that I had to deactivate the automatic thrust control as it could not handle the rapid speed changes. Partly we would have needed full thrust in order to keep the necessary speed yet at altitudes like this thrust is limited. [...] We experienced altitude changes of plus/minus 100 ft. The fasten seat belt sign was on, but nobody would stand up voluntarily.*"

First analysis of the pictures taken by the pilots in the cockpit reveals multiple cloud systems above Iceland (Fig. 4.15). On the one hand lenticularis clouds are visible and on the other hand also cumuli clouds can be detected in the picture. These cloud structures can be attributed to different atmospheric processes as e.g. convection or MWs.

Figure 4.15: Photograph taken from HALO's cockpit after turbulence encounter above Iceland. (Picture taken by Steffen Gemsa)

In the following, the analysis of this case study is presented where the subsequent questions are addressed: What atmospheric process caused the encountered turbulence event? Is a 2D setup of idealized EULAG simulations sufficient to study the generation mechanism of this turbulence event? How well was this event predicted by ECMWF/GTG? How did the research aircraft react to this event? How strong was the encountered turbulence?

4.2.1 Ambient conditions for MW excitation and propagation

ECMWF operational forecasts and analysis

On 13 October 2016, a surface low pressure system was present east of Greenland together with a pronounced surface high pressure system above and north of Scandinavia (see Fig. 4.16 a). As Iceland was located underneath the low-level jet between these low and high pressure systems, strong horizontal surface winds up to about $15\,\mathrm{m\,s^{-1}}$ were present with a south-south-easterly (SSE) direction. This wind direction was almost perpendicular to the main mountain ridges of Iceland (i.e. Vatnajökull, Langjökull and Hofsjökull) and favored the excitation of mountain waves (MWs). Consequently the geopotential height undulates above Iceland due to the mountain wave activity. Between

12 UTC and 18 UTC the meteorological situation remains nearly stationary and the horizontal wind speed decreases slightly by about $2\,\mathrm{m\,s^{-1}}$ (see Fig. 4.16 b). However, the horizontal wind direction veers anti-clockwise and becomes more south-easterly.

In the upper troposphere, the meteorological situation was similar to the surface with a low pressure system west of Iceland and a high pressure system to the east (see Fig. 4.16 c). However, the upper-level trough is more elongated and stretches from Greenland towards south-east to the North Atlantic. The ridge, on the other hand, is located more to the north, right between Scandinavia and Iceland. Therefore, also the polar front jet was located above Iceland with almost the same direction as the surface jet with wind-speeds up to about $55\,\mathrm{m\,s^{-1}}$. The research aircraft HALO flew along this jet from north-west to south-east with a flight direction that was nearly aligned but opposite to the mean wind direction. During the afternoon, horizontal wind speeds decreased from about $40\,\mathrm{m\,s^{-1}}$ to $30\,\mathrm{m\,s^{-1}}$ in the upper troposphere above Iceland as the polar front jet propagated further to the west with the ridge extending further west (see Fig. 4.16 d).

Throughout the troposphere, horizontal wind speeds were mostly $\geq 15\,\mathrm{m\,s^{-1}}$ (see Fig. 4.17 a) and Fig. 4.18 b) and almost no directional shear was present due to the mentioned alignment of the two jets. That way, vertical propagation of MWs is generally supported by the background horizontal wind profile as their ground-based phase speed is equal to zero and therefore no critical layer ($U = 0\,\mathrm{m\,s^{-1}}$) can attenuate propagating MWs in the troposphere and tropopause by non-linear processes. These MWs are visible in the vertical wind speed as stationary, coherent structures of up- and downdrafts with amplitudes of about $1\,\mathrm{m\,s^{-1}}$ (Fig. 4.16 e, f), especially, in the area of Langjökull and Hofsjökull. A cross-section along the flight track reveals that these MWs are able to propagate up to the tropopause region at an altitude of about 11.5 km (Fig. 4.17 b).

Above the tropopause, in the lower stratosphere, the horizontal wind speed decreases by about $10\,\mathrm{m\,s^{-1}}\,/\,\mathrm{km}$ to values smaller than $10\,\mathrm{m\,s^{-1}}$ (Fig. 4.18 b). These small horizontal winds increase the potential for MW breaking due to convective instability as the wave-induced wind perturbation become comparable to the background wind. Indeed, steepening isentropes in the ECMWF forecasts indicate convective instabilities due to breaking mountain waves in the lower stratosphere where HALO's flight track was located. Consequently, amplitudes in the vertical wind speed decrease by about $0.65\,\mathrm{m\,s^{-1}}$ in this region characterized by the strong negative vertical shear in the horizontal wind (Fig. 4.18 b). Further upwards the forecasts suggest that all MWs are attenuated and, therefore, no significant amplitudes are present in the vertical wind field. This preliminary MW analysis is based on the results of the hydrostatic IFS operational analyses. These analyses cannot resolve convective instabilities or any other non-hydrostatic effect on the small-scale vertical wind. However, the hydrostatic response of vertically propagating MWs and the potential of MW breaking is a robust feature of the IFS data around this time.

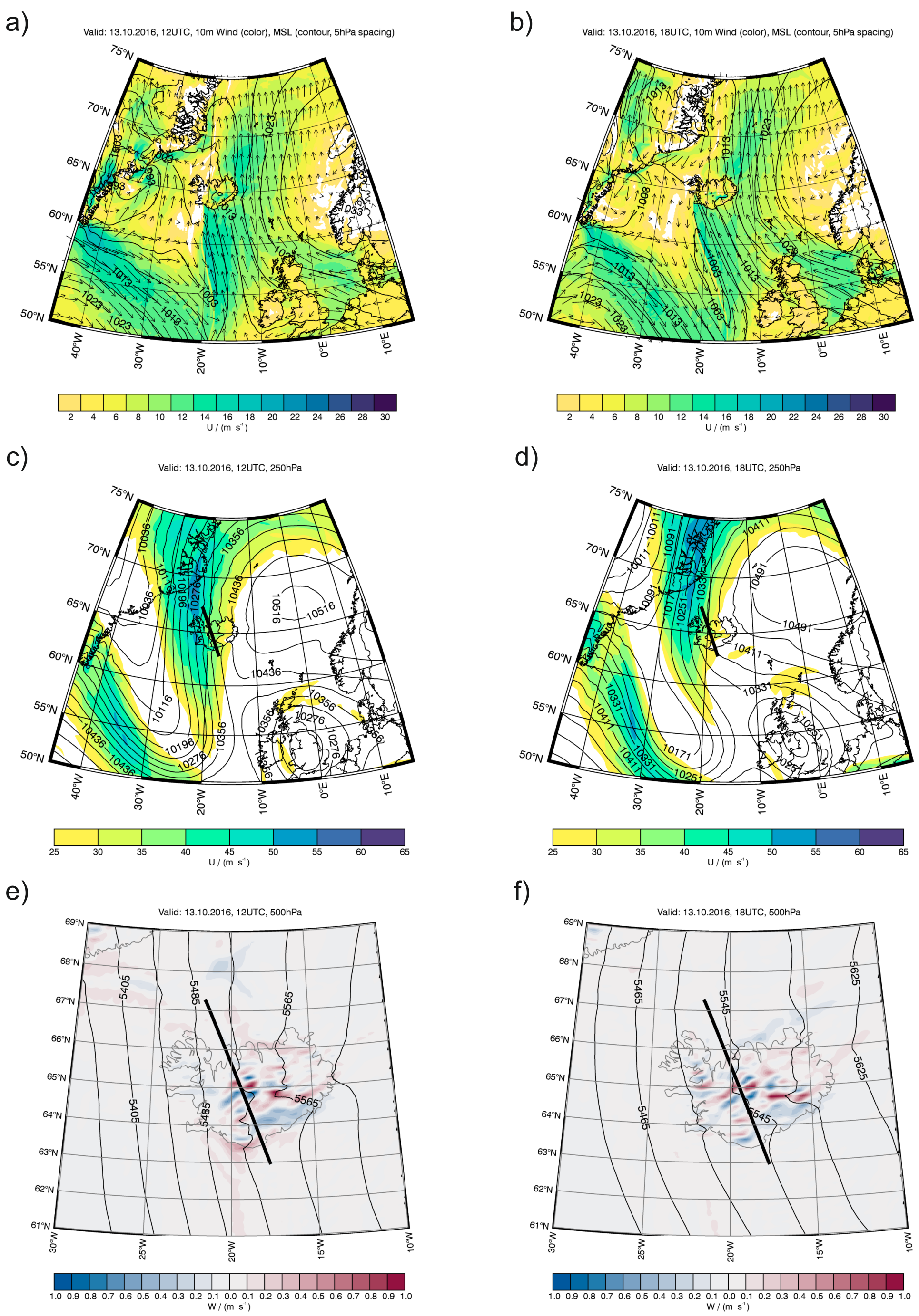

Figure 4.16: Horizontal wind speed at 10 m (a,b) and 250 hPa (c,d), and vertical wind speed at 500 hPa (e,f) as simulated by ECMWF operational analysis for 12 UTC (a,c,e) and 18 UTC (b,d,f). Thin black lines are the mean sea-level pressure in a) and b) and in figures c), d), e) and f) show the geopotential, respectively. Black arrows in a) and b) show wind speed and direction. The thick black line in c), d), e) and f) shows the flight-track of HALO.

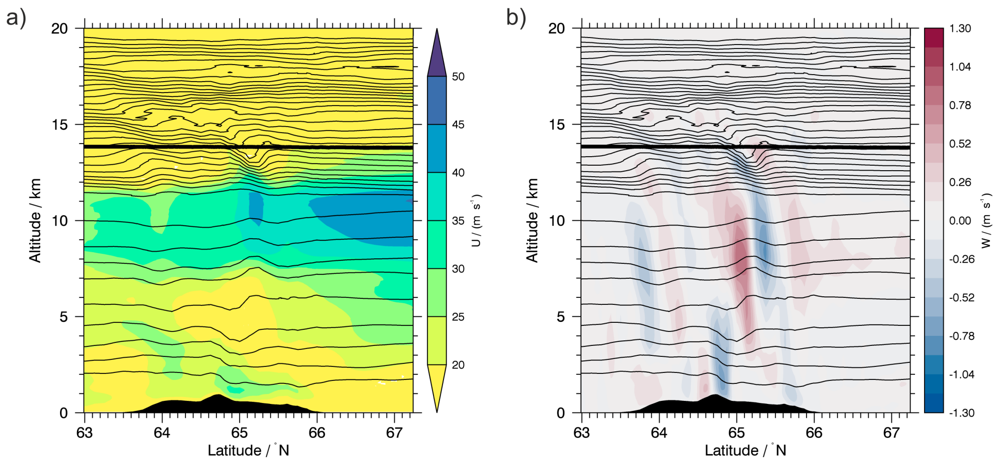

Figure 4.17: Vertical profiles of horizontal wind speed (a) and vertical wind speed (b) along the flight track. Thin black lines are isentropes with a spacing of 5 K and the thick black line shows the flight altitude of HALO, respectively.

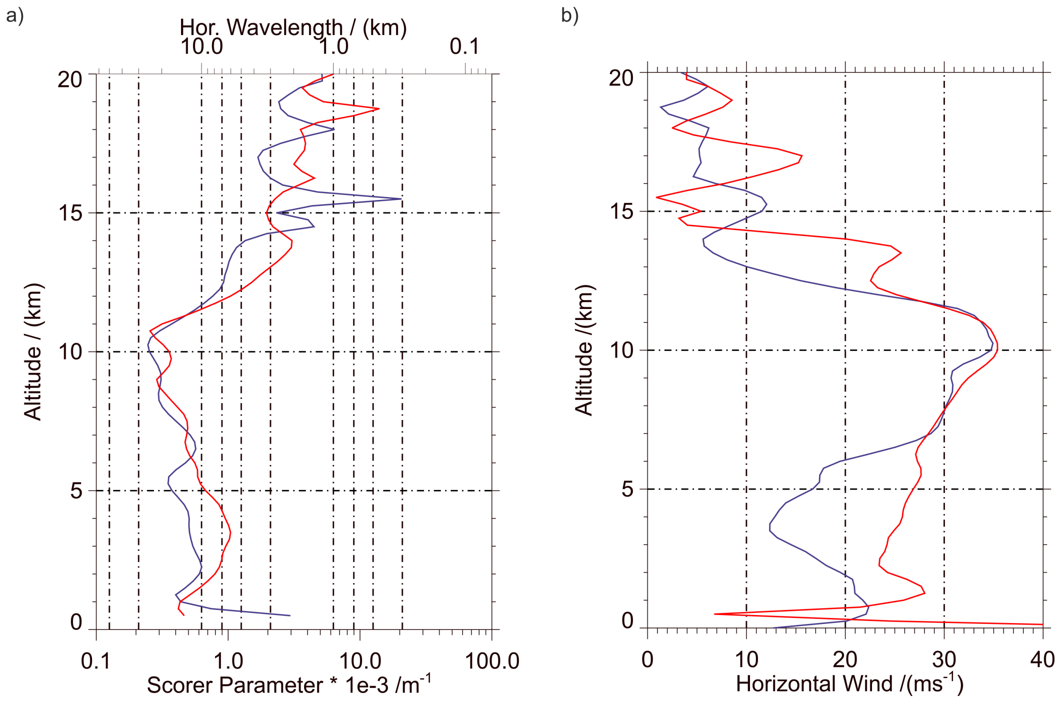

Figure 4.18: (a) Vertical profile of the Scorer parameter and (b) horizontal wind speed at the upstream location (63.14° N, -17.84° E, red line) and the location of the turbulence encounter (blue line). All profiles are based on ECMWF IFS operational analyses at 12 UTC.

The vertical profile of the Scorer parameter (see Sec.2.1 upstream of Iceland (63.14° N, -17.84° E) suggests that MWs with a horizontal wavelength (λ_h) larger than about 25 km are freely propagating through the troposphere into the lower stratosphere. Furthermore, MW modes with 7 km $\lesssim \lambda_h \lesssim$ 20 km reach their turning points ($k \sim l$) at 12 km where they are reflected downwards. MWs with $\lambda_h \lesssim$ 6 km are evanescent in the troposphere and should not reach the tropopause level. Above Iceland at the location of the turbulence event (64.97° N, -19.40° E), the Scorer profile is similar to the upstream profile except for the depth of the trapping layer. Here, this layer is thinner by 3 km covering an altitude range from 7 km to 12 km and consequently MWs with 11 km $\lesssim \lambda_h \lesssim$ 20 km are trapped.

Lidar and Radar Measurements

Downward looking airborne lidar and radar measurements are used to further classify ambient atmospheric conditions during HALO's overpass across Iceland (Fig. 4.19). Both measurements suggest that south of 65° N clouds prevailed in the troposphere with a cloud top height of about 7.5 km at maximum. Radar measurements further indicate that rainfall was present with decreasing intensity towards north (Fig. 4.19 c). Between 64° N and 64.8° N the relative humidity over ice reveals convex structures of alternating enhanced and reduced humidity in the troposphere possibly suggesting convective activity in this area (Fig. 4.19 b). Between an altitude of 10 km and the tropopause (about 11.5 km), humidity is advected from south to Iceland by the polar jet stream. In this region two distinct bands of enhanced humidity with values up to ≈ 85% are prominent. The vertical extent of these features almost doubles towards north from ≈ 500 m to about 1 km. At flightlevel, the relative humidity over ice and water (not shown) decrease to values less than 10% suggesting that dry dynamic processes are the dominant generation mechanisms of the encountered turbulence.

North of 65° N wavelike structures are superimposed on the signals of both, lidar and radar at an altitude ranging from 5 km to 12 km. In the troposphere radar measurements suggest that their horizontal wavelength is about 20 km and the amplitudes increase with altitude from approximately 700 m to 1 km. The upstream tilt (see purple lines in Fig. 4.19 c) revealed by the radar measurements suggests that these waves are vertically propagating. Further upwards, the lidar backscatter shows a larger-scale wave structure which extends from 65° N to about 65.5° N at an altitude of about 10.5 km. Downstream this wave structure horizontal wavelengths decrease to approximately 20 km. Above the tropopause (at about 12 km) from 65° N to 65.2° N, the lidar backscatter signal is superimposed by small-scale wave-like structures with a horizontal wavelength of about 3.5 km. According to the Scorer parameter analysis MWs of that scale are evanescent in the troposphere. Therefore their source can be attributed to local processes as e.g. MW breaking. However, as the Scorer parameter analysis is based on IFS operational

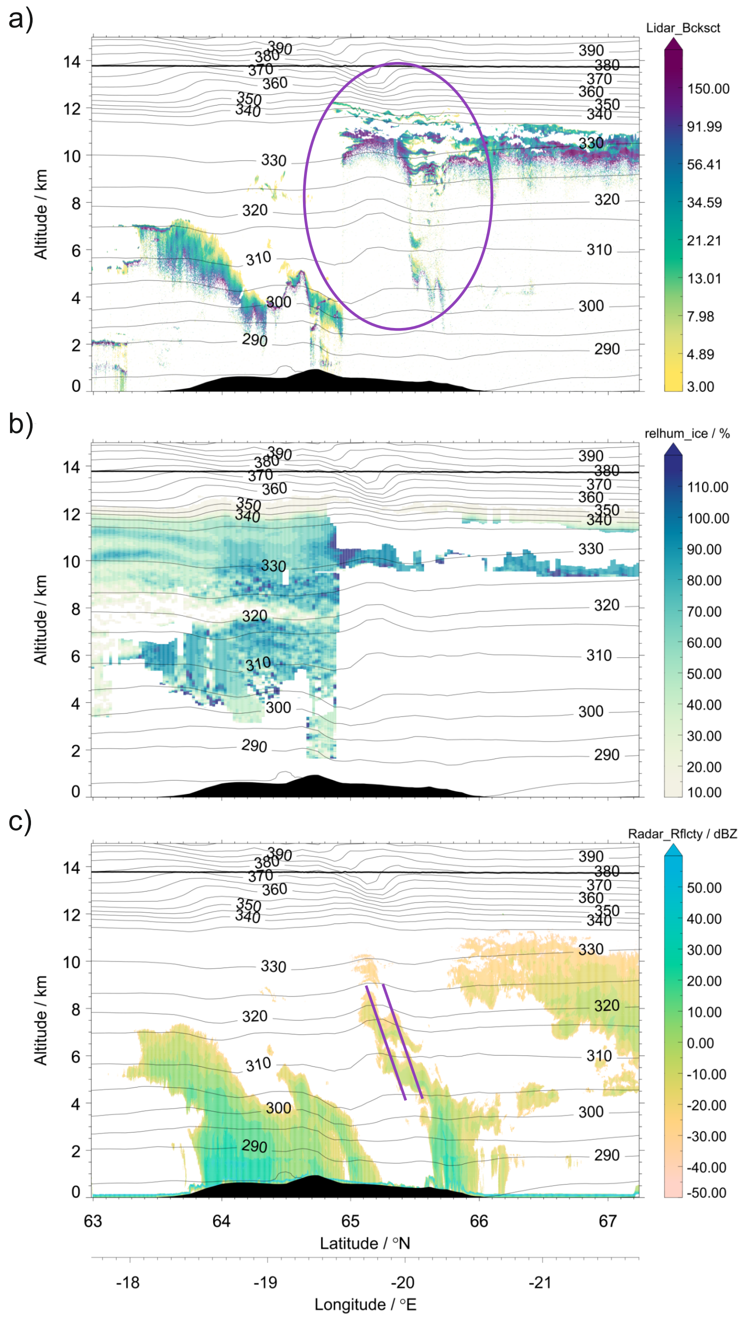

Figure 4.19: Downward looking airborne lidar (a, b) and radar measurements (c) along the flight track. Lidar backscatter is shown in (a) and relative humidity over ice derived from these lidar measurements using ECMWF's temperature in (b), respectively. Topography is the ECMWF topography along the flight track and black lines show isentropes interpolated to the flight track of ECMWF IFS forecasts. Purple ellipse in (a) highlights the analyzed waves on the lidar backscatter signal, while the purple lines mark phase lines in (c). (Data kindly provided by Florian Ewald)

analysis the observed waves can also be produced by processes not resolved by the IFS.

4.2.2 Analysis of Aircraft In situ Measurements

In order to get an overview on the structure of the flow field along the flighttrack and derive MW fluxes as well as turbulence parameters 10 Hz HALO in situ measurements are taken into account (see Fig. 4.20). Furthermore, this dataset is combined with 1 Hz French Falcon in situ measurements to additionally analyze the vertical extent and distribution of marked features of the flow field (Fig. 4.21).

HALO in situ observations reveal large peak-to-peak amplitudes in all presented meteorological parameters at ~65° N, the location of the turbulence encounter (see Fig. 4.20). Especially in the vertical wind speed large values up to 7.6 m s^{-1} are detected. These pronounced amplitudes possibly led to the encountered altitude changes of about 50 m within about 15 s of the research aircraft HALO in this area. Additionally, in this area both horizontal wind speed components decrease to values of about 0 m s^{-1} in the mean. Small-scale structures are superimposed on all presented meteorological parameters in this region. This might be due to turbulence induced by non-linear processes as e.g. breaking gravity waves. In general, both the horizontal wind and the potential temperature measurements are characterized by larger-scale wave patterns with a horizontal wavelength of about 60 km in contrast to the vertical wind which is dominated by small-scale waves.

North of this area starting at about 65.8° N laminar wave patterns without superimposed small-scale structures dominate in all parameters. While peak-to-peak amplitudes in the horizontal wind speed components remain small, they are more pronounced in the vertical wind with about 3 m s^{-1} at maximum and in the potential temperature with approximately 4 K. In this region no clear 90° phase shift between vertical wind and potential temperature can be detected which would indicate vertically propagating linear GWs.

South of Iceland (upstream), between about 63° N - 63.7° N, no pronounced amplitudes are detected in all presented parameters. Also in the vertical wind speed the amplitudes decrease to values smaller than about 0.5 m s^{-1}. Consequently, no significant wave or small-scale structures can be found suggesting calm atmospheric flight conditions as reported by the pilots.

Comparison of HALO observations to the French Falcon in situ measurements reveals similar pattern in all meteorological parameters along the respective flight tracks (see Fig. 4.21). In the area of the turbulence encounter both measurements show enhanced vertical wind speeds where the French Falcon observed vertical wind speeds are with a maximum of about 3.4 m s^{-1} only approximately half of the HALO observed vertical

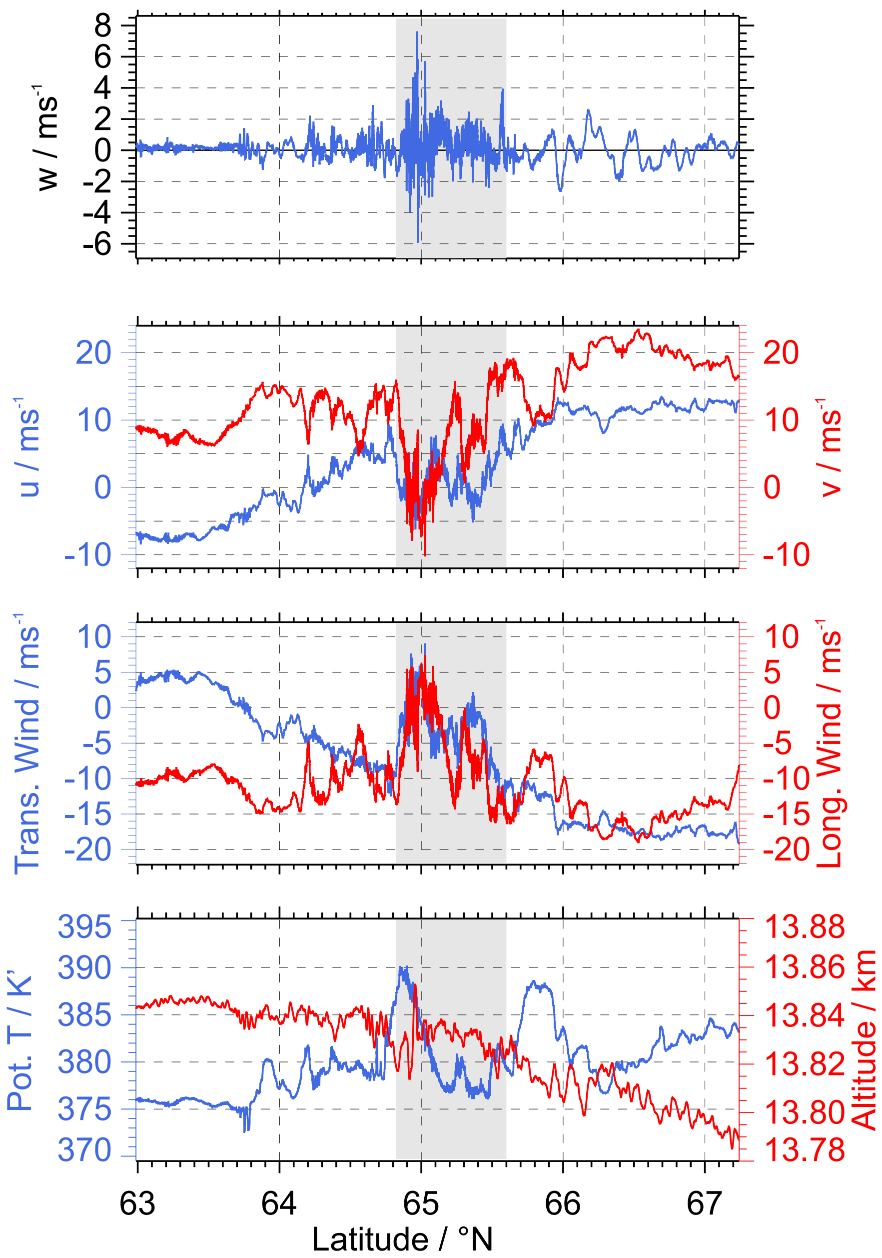

Figure 4.20: HALO 10 Hz in situ measurements of vertical wind speed (top panel), zonal and meridional wind speed (second panel from top), transverse and longitudinal wind speed within aircraft oriented coordinate system (third panel from top), potential temperature and altitude (lowest panel). The gray shading refers to the region of the turbulence encounter which coincides with the time where the autothrottle system of HALO was deactivated. (BAHAMAS data was kindly provided by Christian Mallaun.)

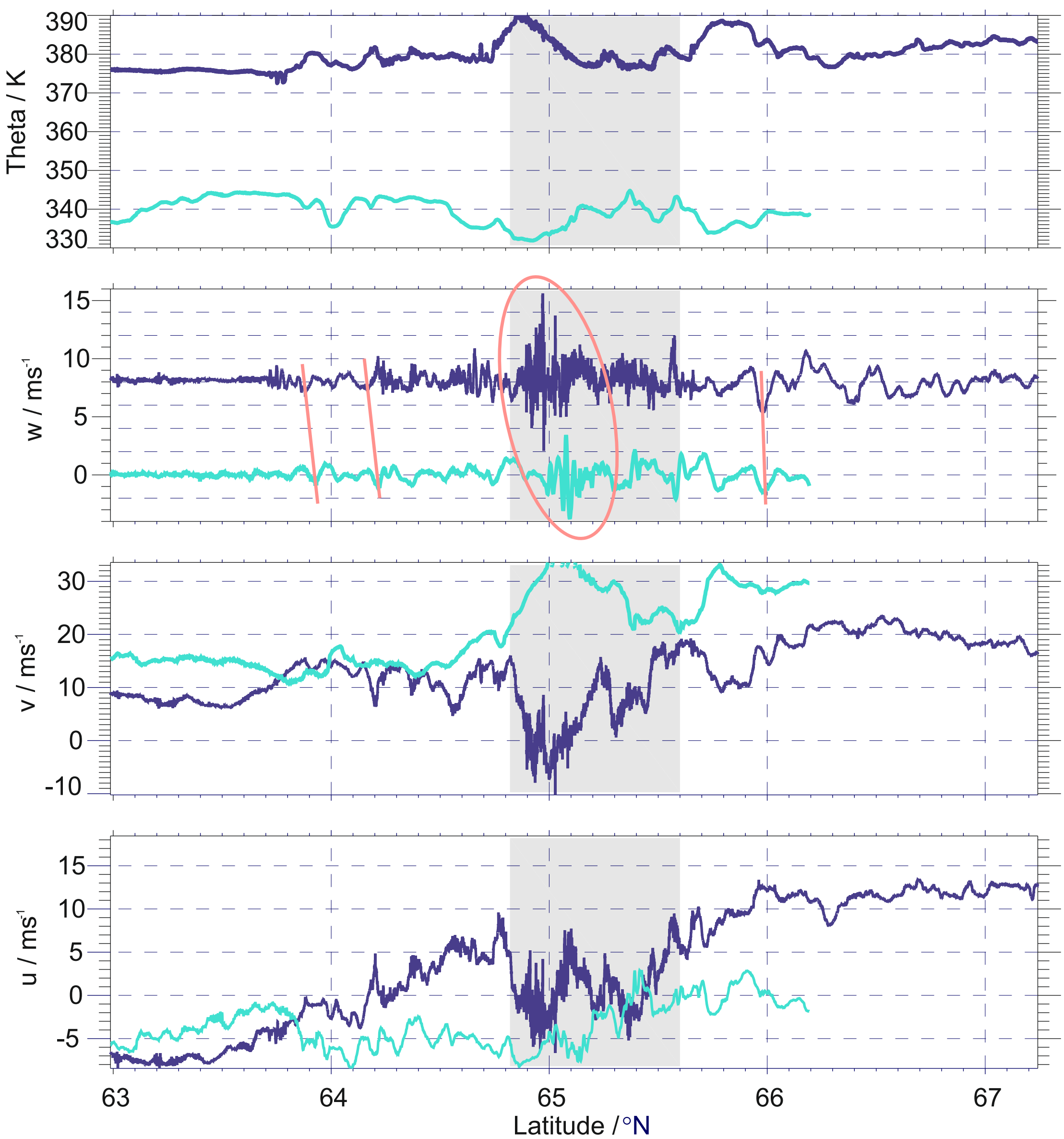

Figure 4.21: HALO 10 Hz in situ measurements (dark blue lines) of potential temperature (top panel), vertical wind speed (second panel from top), meridional and zonal wind speed (lowest two panels). The light blue lines refer to French Falcon 1 Hz in situ measurements. HALO measurements are located at 13.8 km and French Falcon observations at 11.8 km, respectively. Orange lines connect wave structures of the two measurements. The gray shading refers to the region of the turbulence encounter which coincides with the time where the autothrottle system of HALO was deactivated. For better comparison the vertical wind measurement of HALO is shifted by $7\,\mathrm{m\,s^{-1}}$ in the second panel from top. (French Falcon data was kindly provided by Thomas Spengler.)

wind maximum. When connecting the maximum vertical wind speeds of the two measurements, an upstream vertical tilt of the turbulent region reveals (see ellipse in Fig. 4.21, flight altitudes of HALO and the French Falcon are 13.8 km and 11.8 km, respectively). At this location where the maximum vertical wind is encountered, the meridional wind speed observed by the French Falcon increases to about 30 m s^{-1}. This suggests that a negative vertical shear of the horizontal wind was present in this area.

Upstream of the turbulence encounter at around 64°N coherent wave structures are present in both measurements with a horizontal wavelength of about 20 km to 30 km. When again connecting these structures an upstream vertical tilt appears indicating vertically upwards propagating MWs (see orange lines in Fig. 4.21).

Downstream the turbulence encounter both measurements reveal a wave-like pattern at about 66 °N where the phase line is almost vertical. At about 65.5° N a sequence of distinct down- and updrafts is present in the French Falcon measured vertical wind speed.

Analysis of Mountain Waves in the Lower Stratosphere

To determine the linearity of the observed MWs, the Eliassen-Palm relation is tested (see also Sec. 3.1.3). Figure 4.22 shows the result of this analysis where an almost perfectly linear wave signature can be seen when both curves match each other closely. Deviations can have different reasons as discussed below. Analyzing these Eliassen-Palm fluxes derived from HALO in situ measurements reveals a complicated situation regarding MW propagation along the flighttrack (see Fig. 4.22).

Analysis of the fluxes integrated over the complete flight leg suggests upward propagating MWs with a positive EF_z of 1.26 W m^{-2} and $-UMF$ of 2.07 W m^{-2} (not shown). However, these values are low and the magnitude of EF_z is reduced by 40% compared to $-UMF$ indicating that also non-linear processes are present.

When taking into account the scale-separated energy fluxes upstream the turbulence encounter relatively small large-scale energy and heat-fluxes are detected (see Fig. 4.22 a and blue line in c). While south of Iceland no pronounced values were detected, these increase gradually towards north until they reach values of up to about 2 W m^{-2} for the energy flux and 100 W m^{-2} for the vertical heat flux in the lee of Myrdalsjökull. Starting at about 64° N the energy fluxes EF_z and UMF are very well aligned and the heat flux is almost equal to 0 W m^{-2}. Thus the observations suggest linearly upwards propagating MWs in this region (see Fig. 4.22 a, c). At turbulent scales (see Fig. 4.22 b and orange line in panel c) no pronounced values were observed in the energy and heat fluxes upstream the turbulence encounter.

At the location of the turbulence event (gray shaded area in Fig. 4.22) the energy- and heat-fluxes at all scales show pronounced peaks. In this region the linear relationship

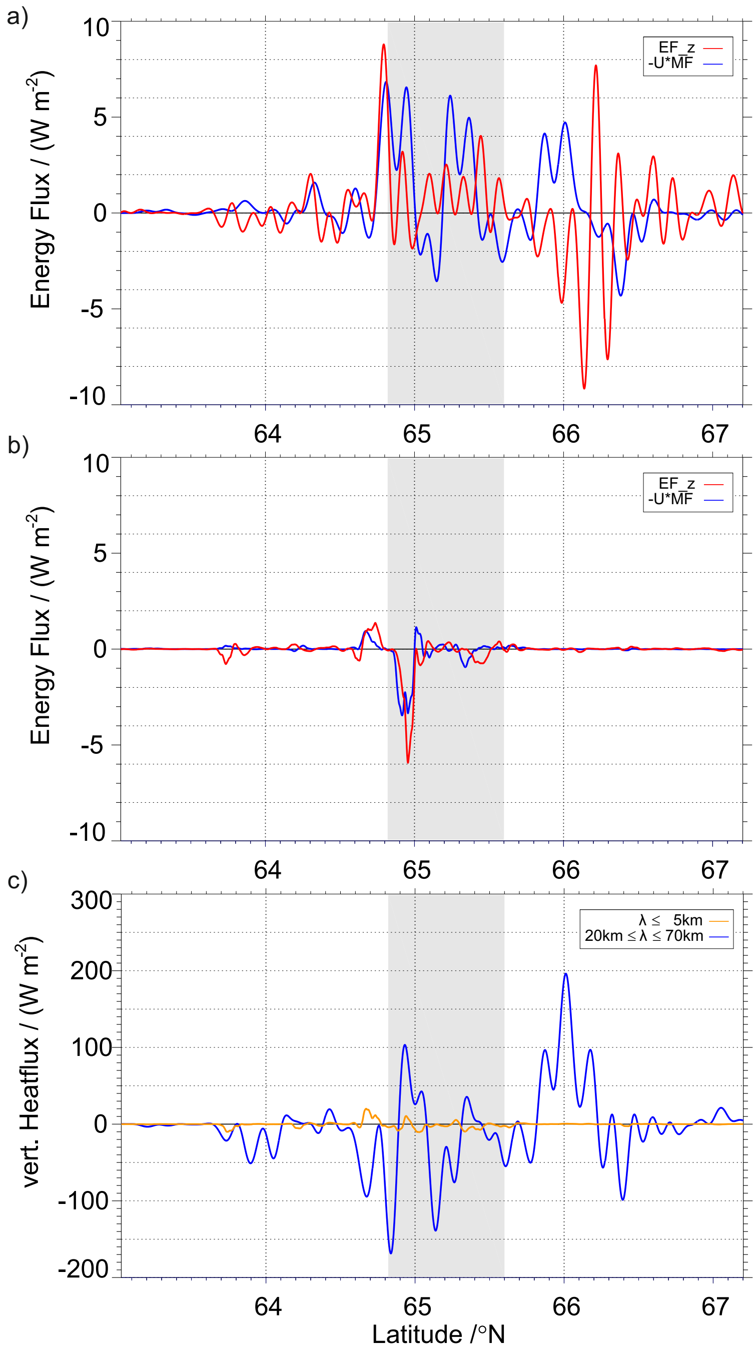

Figure 4.22: Scale separated vertical energy flux (EFz, red), energy flux derived from horizontal momentum fluxes (UMF, blue, a and b) and vertical heat flux (c) along the complete flight leg. Panel a) shows fluxes related to 20 km $\leq \lambda_h \leq$ 70 km and b) the fluxes derived for the turbulent scale ($\lambda_h \leq$ 5 km). The orange line in panel c) shows the heat flux for the turbulent scale and the blue line refers to the heat flux of the propagating MW scales, respectively. The gray shaded area highlights the turbulent region.

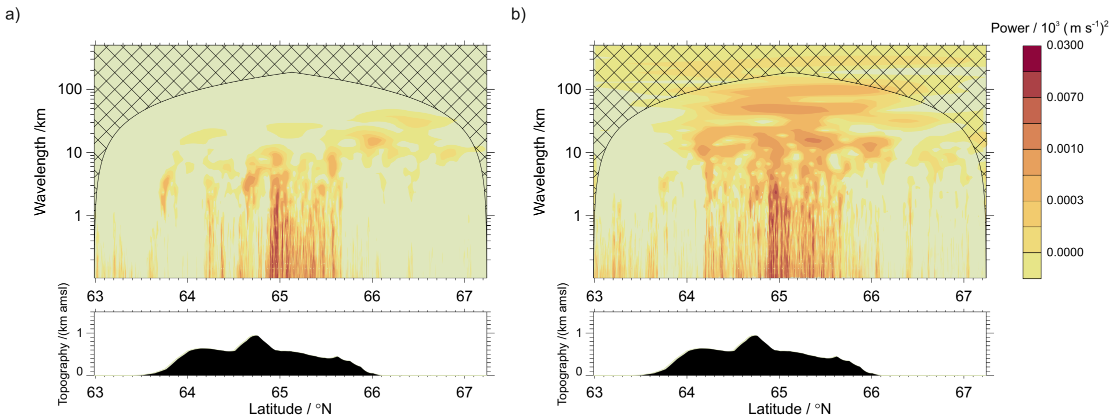

Figure 4.23: Power spectral density of the (a) vertical wind speed and (b) the longitudinal component of the horizontal wind speed of in situ HALO measurements. Presented topography is the ECMWF topography underneath the flight-track.

EF_z and UMF breaks down completely and even an anticorrelation of the two fluxes evolves (see Fig. 4.22 a,b). Together with the finding of the differing leg-integrated fluxes, the structure of these fluxes suggests the presence of non-linear processes. In this region the large-scale fluxes increase up to 4 W m^{-2} of the EF_z and about 6 W m^{-2} of UMF, respectively. At turbulent scales, the values of EF_z decrease from about +1.5 W m^{-2} to about -6 W m^{-2} and for UMF from approximately +1 W m^{-2} to about -3.5 W m^{-2}, respectively. Furthermore, the vertical heat flux at both scale ranges reveals pronounced peaks around 65° N (blue line in Fig. 4.22 c). In agreement with the analysis of the energy fluxes this indicates the presence of non-linearly propagating MWs. Additionally, the sign of the heat flux changes twice in this region while positive values of up to about 100 W m^{-2} at large scales and up to about 10 W m^{-2} at turbulent scales are present at 64.9° N. These positive heat fluxes suggest the presence of convective instability for a wide range of scales at this location (Jiang and Doyle 2004).

Downstream the turbulence encounter (north of 65.6° N) the fluxes generally decrease to smaller values. In particular at turbulent scales no pronounced energy- and heat-fluxes were observed in this area (see Fig. 4.22 b and orange line in panel c). However, around 66.2° N enhanced values of large-scale EFz and vertical heat-fluxes were detected (see Fig. 4.22 a and blue line in panel c). Here, the large-scale EFz and vertical heat-flux increase up to about 8 W m^{-2} and 200 W m^{-2}, respectively. As EFz and UMF are not aligned in this area these observations indicate the presence of non-linearly propagating MWs in the Eliassen-Palm framework.

Taking into account wavelets of the vertical wind speed (Fig. 4.23 a) and the longitudinal (along-track) wind component (Fig. 4.23 b), in the area of the turbulence encounter most wavelet power is contained in small scales of less than 10 km. North of the turbulent area, the situation changes for the longitudinal wind and the power is largely distributed in horizontal wavelengths between 10 km to 20 km.

The cospectra analysis of EF_z and MF_y shows that the majority of significantly energy-containing fluxes have horizontal wavelengths (λ_h) less than 10 km (see Fig. 4.24 a and b). These are located at and north of the region of the turbulence encounter. Here, we particularly show the meridional component of the momentum flux as the main wind direction was mainly meridionally oriented. The observed range of scales can be attributed to the small-scale and turbulent range as defined in Smith et al. (2016). In the scales larger than 10 km little energy up to 0.003 W m^{-2} is contained. Taking into account the Scorer parameter, the found GW scales cannot be attributed to small-scale MWs excited at the surface but rather to breaking MWs or secondary GWs.

Further downstream at about 66° N the vertical energy flux suggests the presence of propagating waves with a horizontal wavelength of about 30 km to 60 km (see Fig. 4.24 c). However, in this region no anti-correlation between EF_z and MF_y is present and additionally the cospectrum of the meridional component of the momentum flux does not show significant fluxes in that region. Additionally the vertical heat flux reveals enhanced magnitudes for these scales at the same location. Therefore, these signatures cannot be attributed to linearly propagating MWs in the framework of the Eliassen-Palm theory.

Turbulence Analysis

Fig. 4.25 a shows the along-track profiles of TKE calculated from in situ wind measurements on different subleg lengths (see also Sec. 3.1.4). The presented subleg lengths range from 4 km to 16 km. The magnitude of TKE decreases with decreasing subleg length, as is expected and shown in Sect. 4.1. Turbulent scales affecting aircraft the most range from 300 m to 1 km (MacCready 1964, Vinnichenko et al. 1980, Hoblit 1988, Sharman et al. 2014). As we are mainly interested in these scales, we analyse the turbulence on the 4 km sublegs in the following. Note, that the spectra of the three wind components are presented in appendix A.1.

Here, the largest variance in the wind speed was observed at 64.9° N, the location of the turbulence encounter. In this area the TKE is enhanced by a factor of about 10 compared to the rest of the leg. Values increase to $\approx 11\,\mathrm{m^2\,s^{-2}}$ in the maximum in this region suggesting pronounced atmospheric turbulence. Enhanced TKE magnitudes larger than $1\,\mathrm{m^2\,s^{-2}}$ are present between about 64.8° N to 65.7° N. South and north of the location of the turbulence encounter almost no TKE is contained in the 4 km sublegs. TKE values in these regions are smaller than the nominal threshold value of 0.6 used by Strauss et al. (2015) indicating calm atmospheric flight conditions for HALO.

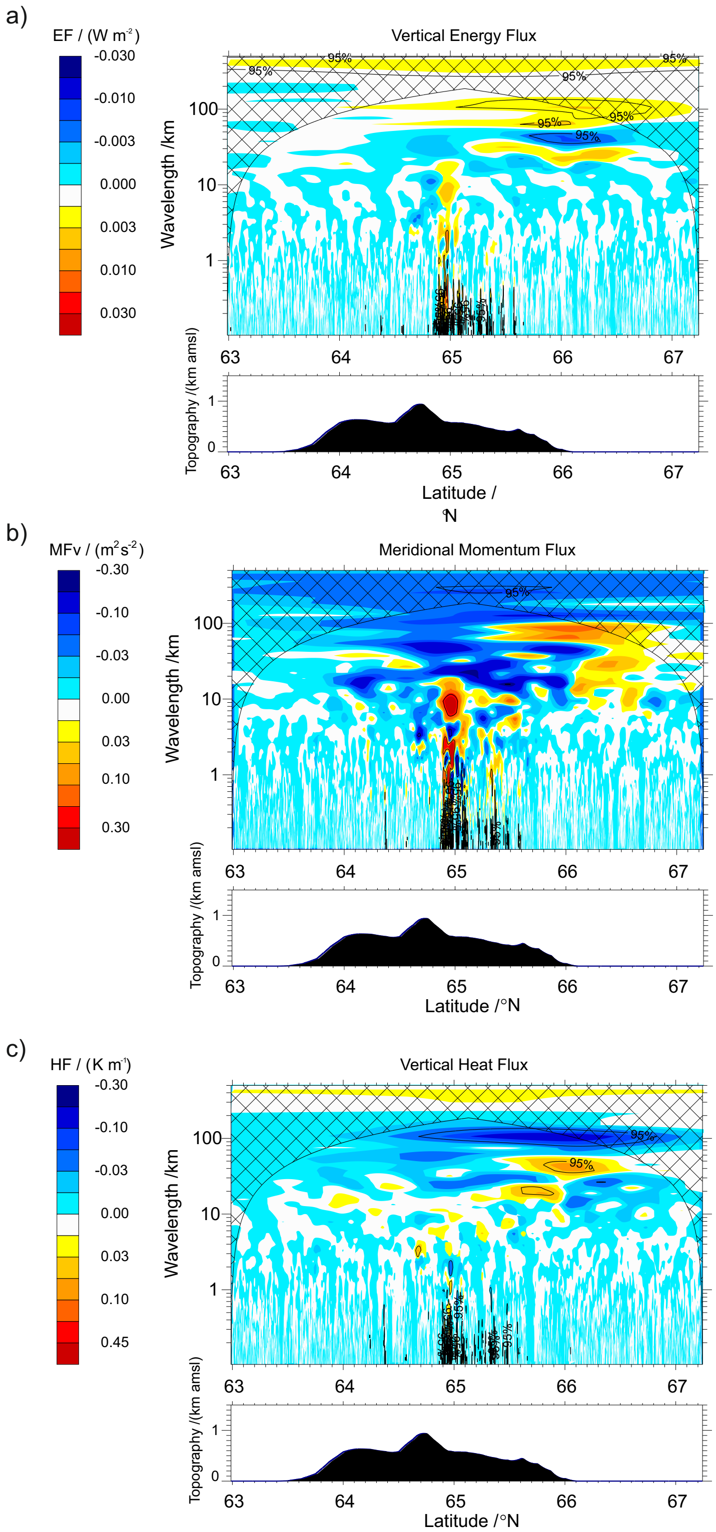

Figure 4.24: Co-spectra of vertical energy flux (EF_z, a), meridional momentum flux (MFy, b) and vertical heat flux (VHF, c).

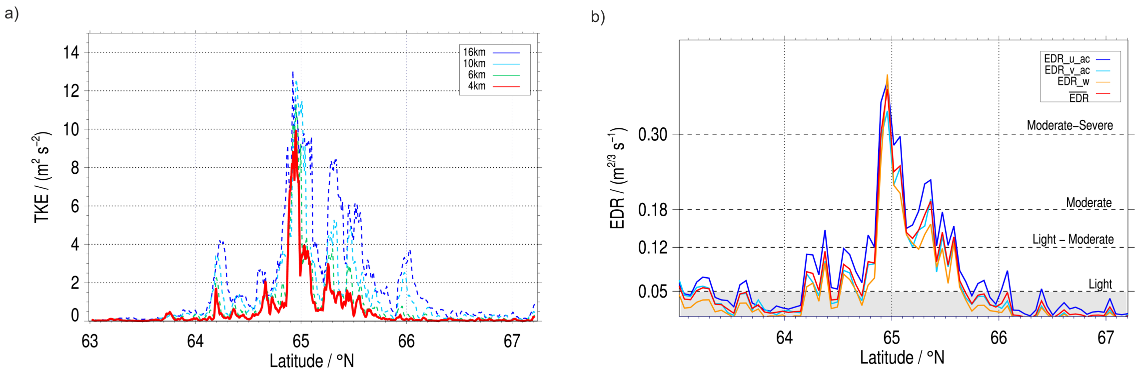

Figure 4.25: (a) Turbulent kinetic energy (TKE) derived from different subleg lengths. (b) Energy dissipation rate (EDR) for all wind components in an aircraft related coordinate system and the log-mean $\overline{EDR}$ calculated from all wind components.

As already suggested by the TKE analysis, also the distribution of EDR along the flighttrack indicates that the turbulence encounter was a localized event where the maximum turbulence covers a distance of about 20 km (Fig. 4.25 b). While south of 64.8° N at maximum light turbulence was detected, EDR increases abruptly by a factor of ≈ 3 within about 0.1° latitude in all three wind components. Here, moderate-to-severe EDR values are present at about 65° N with a maximum of $0.39\,\mathrm{m}^{2/3}\,\mathrm{s}^{-1}$. North of this turbulent area, EDR decreases gradually until calm atmospheric flight conditions prevail again north of 65.7° N.

Individual EDR_i values scatter around the geometric mean $\overline{EDR}$ indicating mostly anisotropic turbulent conditions due to e.g. the high stratification in the stratosphere (see also appensix A.1). In the area of the turbulence encounter conditions are more isotropic as $EDR_{u_{ac}}$ and EDR_w are almost equal.

4.2.3 ECMWF and GTG Predictions of the Event

Generally, the spatially and temporally interpolated ECMWF IFS forecasts agree well with the in situ measurements and reproduce the measured mesoscale structures (see Fig. 4.26). Here, the largest differences are found in the temperature and vertical wind speed. On the one hand, the forecasted temperature is on average lower by about 2 K and the measured large amplitudes at about 65.8° N are not predicted. The simulated vertical wind speed, on the other hand, shows only small amplitudes with a maximum of about $0.4\,\mathrm{m\,s}^{-1}$ which is in contrast to the measured maximum of $7.6\,\mathrm{m\,s}^{-1}$. Wavelets of the potential temperature as well as the zonal and meridional wind speed further indicate that largest power is contained in scales larger than about 40 km (see Fig. 4.27).

Table 4.1: Overview on the mean difference between HALO in situ measurements and ECMWF data along the complete leg for the different meteorological parameters and the respective standard deviation.

	Mean Diff. (ECMWF-in situ)
Temperature	-2.01 $\pm$ 1.91 K
Potential Temp.	-2.38 $\pm$ 3.33 K
Vertical Wind	-0.09 $\pm$ 0.80 m s^{-1}
Meridional Wind	0.76 $\pm$ 4.26 m s^{-1}
Zonal Wind	1.41 $\pm$ 3.92 m s^{-1}

In the area of the turbulence encounter, the large gradients in the potential temperature, meridional and zonal wind are well reproduced. However, the location of these gradients are predicted further to the north by about 0.15° compared to the in situ measurements. Additionally, the decrease of the zonal wind speed is overestimated by the ECMWF IFS by up to about 4 m s^{-1}, while the potential temperature increase is smaller by about 2 K in the forecast. The detected large amplitudes of the vertical wind speed are not predicted.

Table 4.2: Overview on the mean difference between French Falcon in situ measurements and ECMWF data along the complete leg for the different meteorological parameters and the respective standard deviation.

	Mean Diff. (ECMWF-in situ)
Temperature	-0.71 $\pm$ 1.52 K
Potential Temp.	3.59 $\pm$ 2.38 K
Vertical Wind	-0.39 $\pm$ 0.64 m s^{-1}
Meridional Wind	3.89 $\pm$ 2.30 m s^{-1}
Zonal Wind	-0.50 $\pm$ 1.75 m s^{-1}

The comparison between French Falcon in situ observations and ECMWF forecasts reveals a similar situation to the comparison with the HALO measurements (see Fig.4.28). Again, the large-scale structures are reproduced very well while the amplitudes in the vertical wind are underestimated. Here, the best agreement is found in the zonal wind and the potential temperature measurements.

To forecast aviation turbulence, the GTG combines CAT and MWT predictions by taking the maximum value at a time of either one diagnostic. Analysis of this

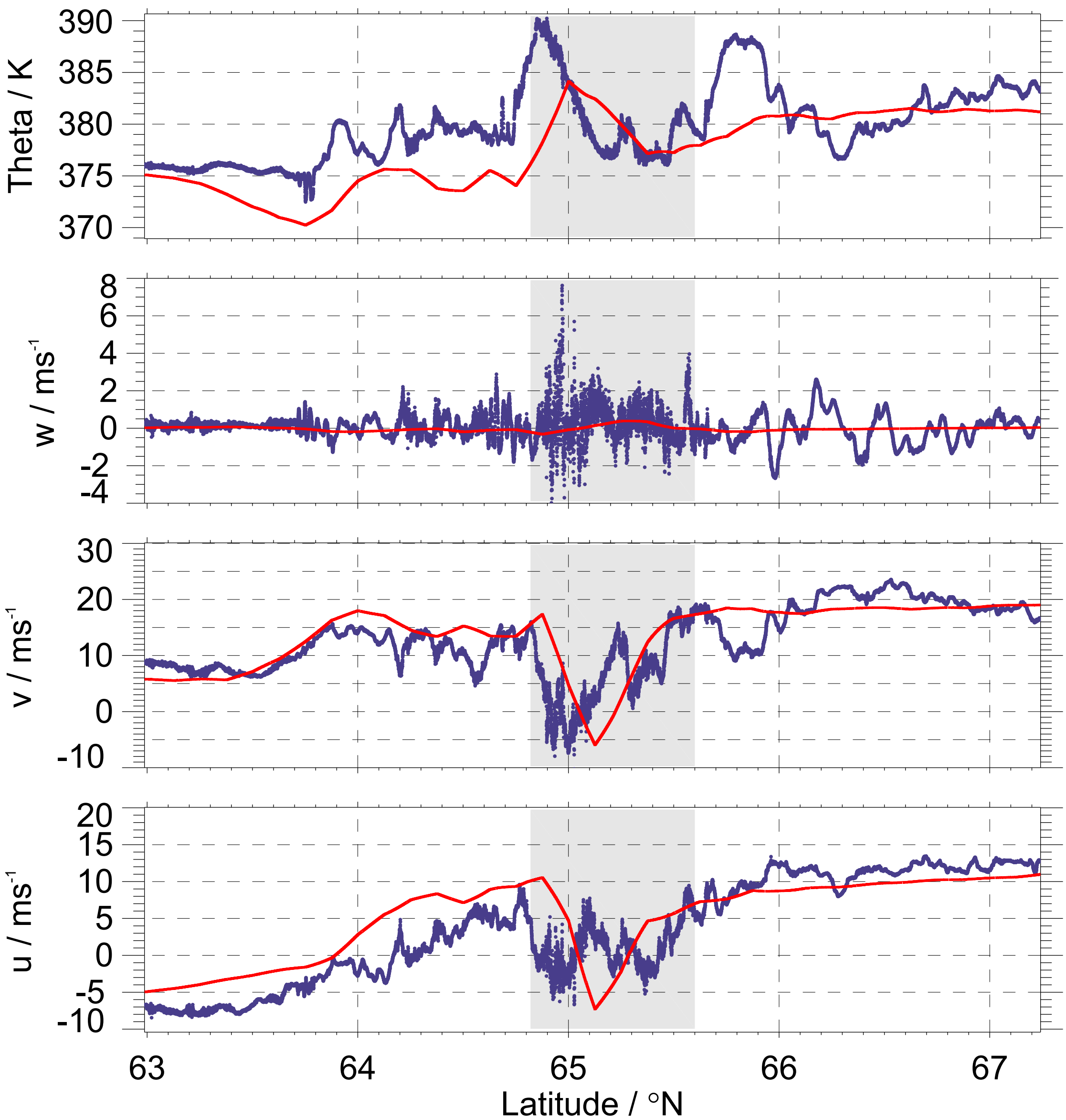

Figure 4.26: HALO in situ measurements (blue lines) of potential temperature (top panel), vertical wind speed (second panel from top), meridional and zonal wind speed (lowest two panels). The red lines refer to ECMWF IFS forecasts interpolated spatially and temporally to the flighttrack. The gray shading highlights the region of the turbulence encounter.

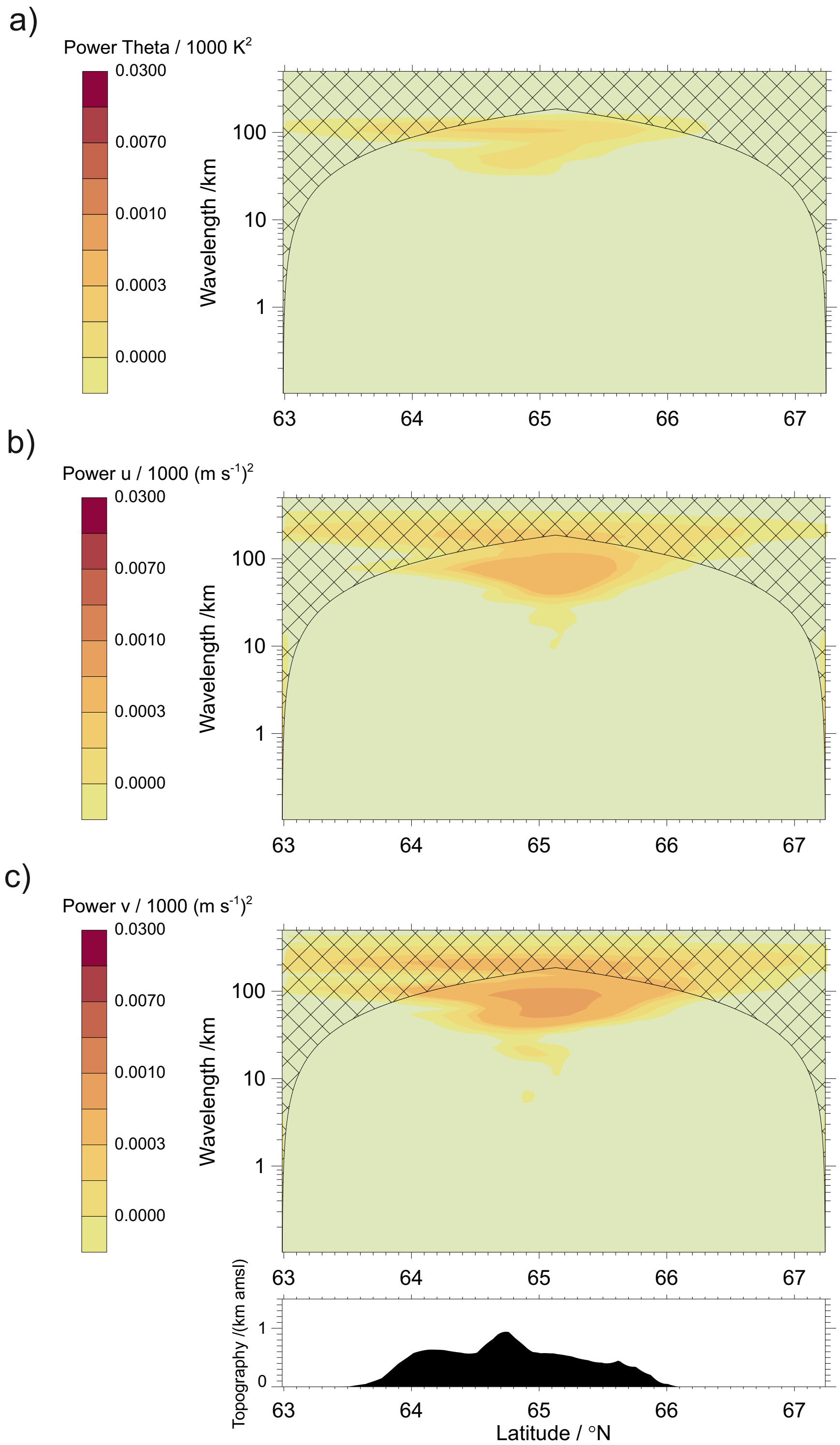

Figure 4.27: Wavelets of ECMWF forecasts of the potential temperature (a), zonal wind speed (b) and meridional wind speed (c). All data is interpolated spatially and temporally to the flighttrack of HALO.

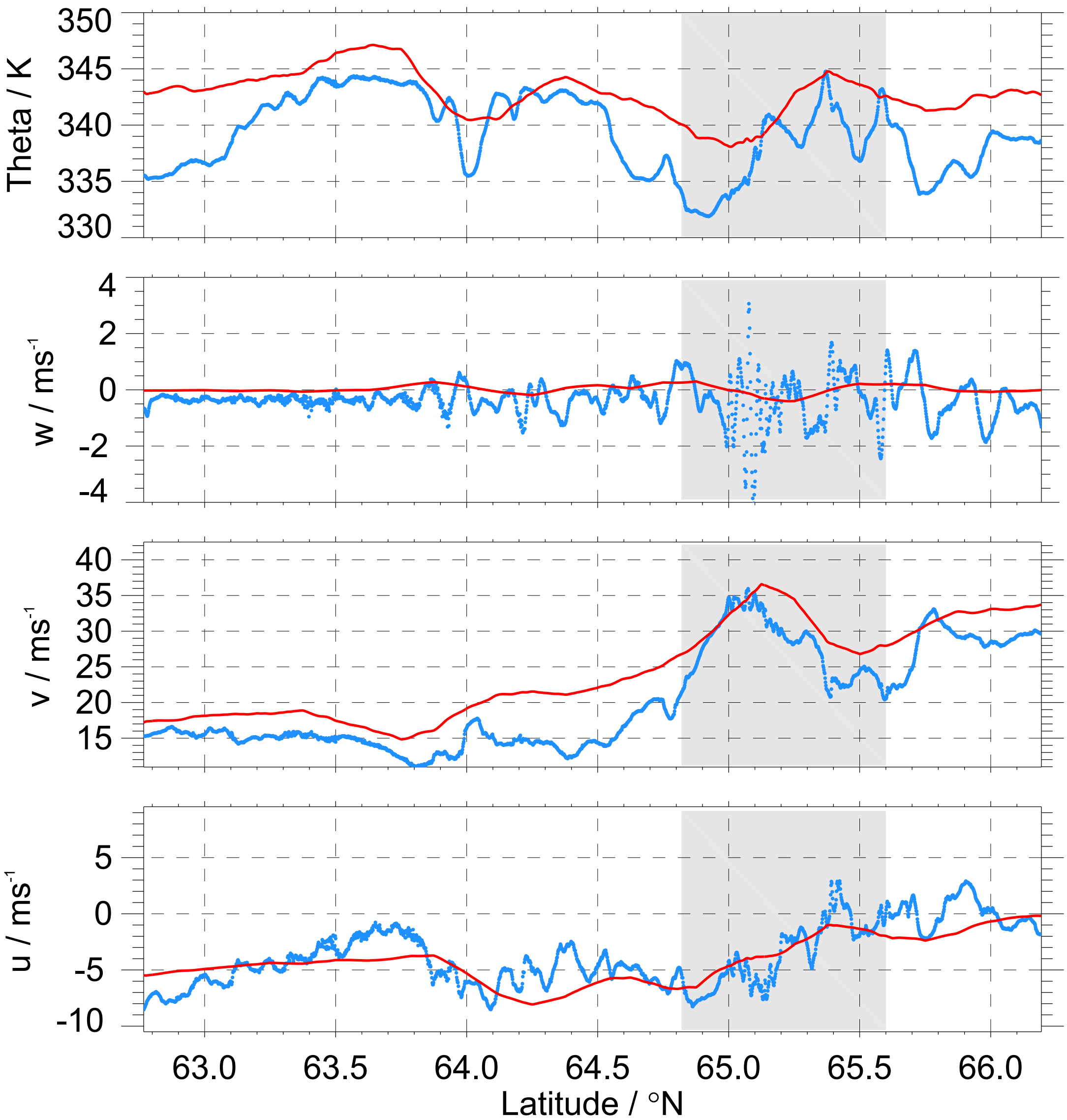

Figure 4.28: French Falcon in situ measurements (blue lines) of potential temperature (top panel), vertical wind speed (second panel from top), meridional and zonal wind speed (lowest two panels). The red lines refer to ECMWF IFS forecasts interpolated spatially and temporally to the flighttrack. The gray shading highlights the region of the turbulence encounter.

combination reveals that the magnitude and location of maximum encountered turbulence was forecasted correctly. However, in general the GTG has a clear tendency to overpredict the magnitude of turbulence for most part of the flight track (see Fig. 4.29 a). Here, the mean difference between forecasted and measured EDR is about $0.17\,\mathrm{m}^{2/3}\,\mathrm{s}^{-1}$ (see Fig. 4.29 c). Additionally, the detected turbulent intermittency is not captured in the forecasts.

Comparison of the MWT to the CAT diagnostic (see Fig. 4.29 c) reveals that the correct forecast of the maximum turbulence magnitude is due to the MWT forecast. Interpolation of the GTG data to the flight track (Fig. 4.29 c) shows that the general shape of the MWT diagnostic also approximately follows the measured EDR, yet with values that are mostly larger than the measured EDR. The mean difference between MWT and measured EDR is smaller by about $0.02\,\mathrm{m}^{2/3}\,\mathrm{s}^{-1}$ compared to the GTG combination.

4.2.4 2D EULAG Simulations

2D EULAG simulations are used to study the generation mechanism of the turbulence encountered by HALO and were kindly provided by Henrike Wilms (Fig. 4.30 and Fig. 4.31, see Sec. 3.2.3 for information regarding the model setup). At first, the evolution of the simulated MW is studied with the help of the vertical wind speed (Fig. 4.30). After one hour simulation time, a coherent pattern of up- and downdrafts has developed above the highest elevation between -50 km to the center of the domain (Fig. 4.30 a). This structure can be related to a hydrostatic MW propagating through the troposphere into the lower stratosphere. Its horizontal wavelength is about 50 km and the maximum amplitude in the vertical wind is $\approx 0.75\,\mathrm{m\,s}^{-1}$. Due to the strongly decreasing horizontal wind speed together with increasing stability in the stratosphere phase lines tilt upstream in the lower stratosphere between an altitude of 12.5 km and 15 km which is in concurrence with the results of the analysis of the ECMWF IFS data.

One simulation hour later (Fig. 4.30 b,d), the maximum amplitude of the pronounced MW increases to about $1\,\mathrm{m\,s}^{-1}$ in the troposphere. In the lower stratosphere between an altitude of about 12 km to 14 km isentropic surfaces steepen and the static stability becomes negative (Fig. 4.30 d). Underneath this region, in an altitude range from $\approx$10 km to 12 km, the hydrostatic MW steepens and breaks. As the numerical simulations are 2D and due to their horizontal resolution of 200 m they do not resolve turbulence explicitly, the simulated structures appear at the grid scale (Fig. 4.30 c). The Nonoscillatory Forward-in-Time (NFT) numerics ensures that the model simulations maintain numerical stability. According to the Scorer parameter the small-scale wave structures cannot origin from the ground due to filtering effects in the troposphere and tropopause. Therefore the steepening isentropes and small-scale wave structures are a)

b)

c)

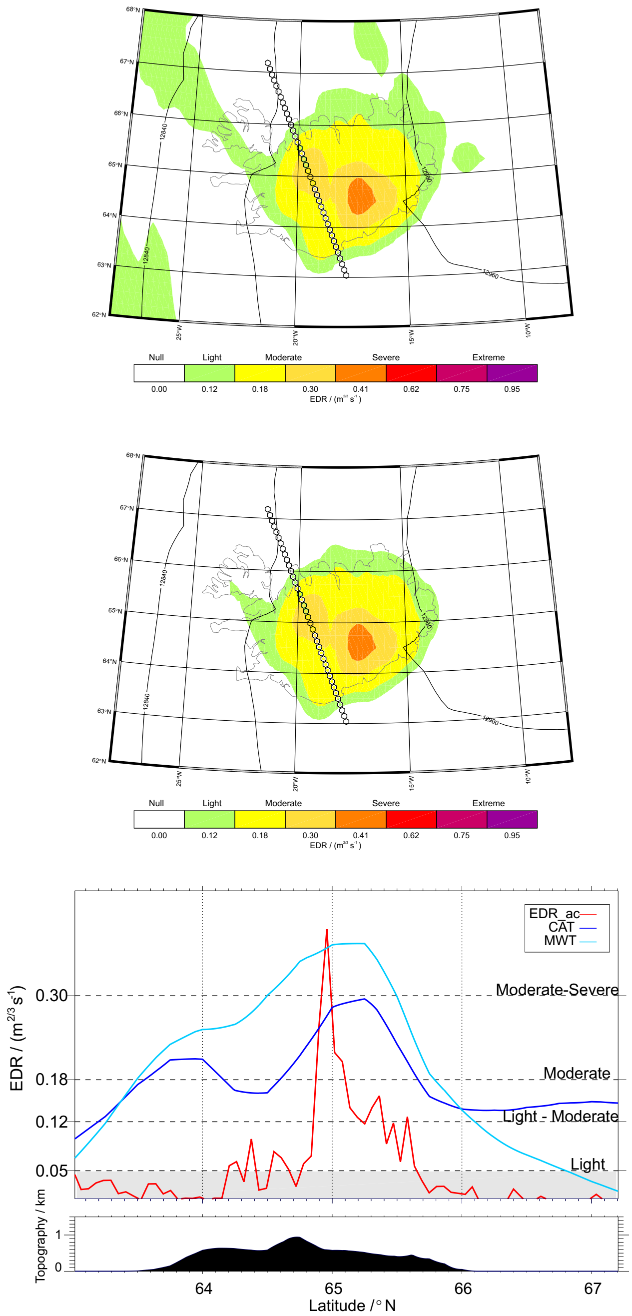

Figure 4.29: GTG turbulence prediction for FL430 above Iceland based on ECMWF forecasts valid at 15 UTC together with the geopotential height (black solid lines). Panel (a) shows the GTG combination of MWT and CAT forecasts and (b) only the MWT forecast, respectively. The colored dotted line presents the in situ measured EDRs where the color coding refers to the turbulent severity resulting from the maximum value over a timeframe of about one minute. (c) Comparison of in situ measured EDR derived from vertical wind speed to MWT and CAT interpolated to the flight track.

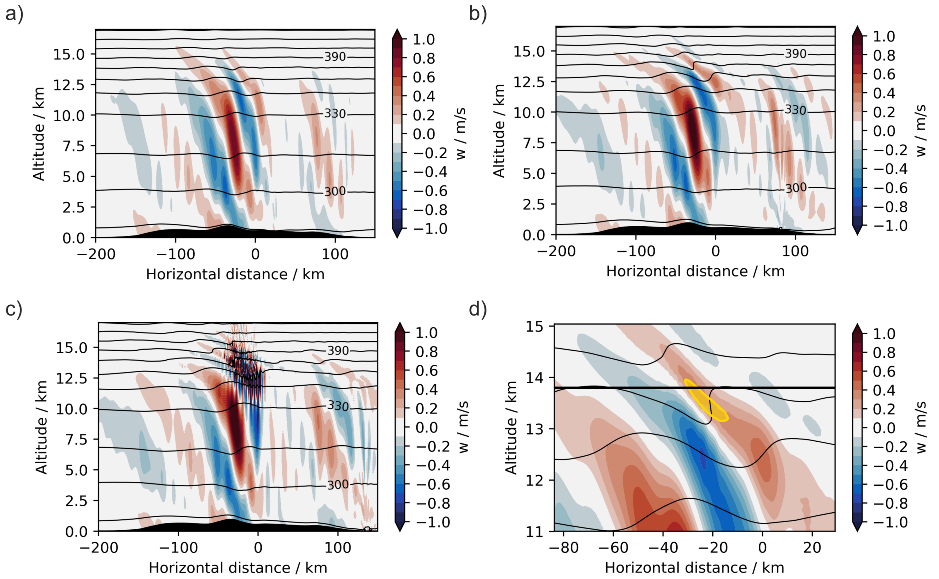

Figure 4.30: Idealized EULAG simulations depicting the vertical wind speed after (a) one simulated hour, (b) two simulated hours and (c) three simulated hours. Black contour lines show isentropic surfaces. Panel (d) shows a zoom into the region where isentropes steepen at two simulated hours. The area of negative static stability is highlighted in orange.

a first indication of MW steepening and breaking in the area of pronounced negative vertical shear in the horizontal wind speed.

After three simulated hours (Fig. 4.30 c and Fig. 4.31), EULAG simulations reveal the evolution of a pronounced MW breaking region in the lower stratosphere above and downstream of the mountain. In this region the values of the MW induced perturbations of the horizontal wind and the magnitude of the background horizontal wind itself are almost equal (see Fig. 4.32). As the direction of the horizontal wind perturbation is opposite to the direction of the background horizontal wind the two wind components cancel each other out and a local critical level for MWs evolves (see Fig. 4.32 a). In this region, isentropes steepen and, eventually overturn during convective instability. Turbulent mixing due to this overturning is reflected by nearly vertical isentropic surfaces suggesting locally neutral stratification. Consequently, small-scale wave structures with amplitudes in the vertical wind up to about 6.6 $\mathrm{m\,s^{-1}}$ evolve. Furthermore, the observed downstream shift of the turbulent region found in the French Falcon data at 11.8 km altitude is reproduced by EULAG.

In accordance with the observations, EULAG simulations reveal that small-scale disturbances are superimposed also on the horizontal wind and the temperature in the MW breaking region (Fig. 4.31 b and d). Additionally, in this region EULAG reproduces in the horizontal wind the deceleration observed by HALO and the acceleration measured

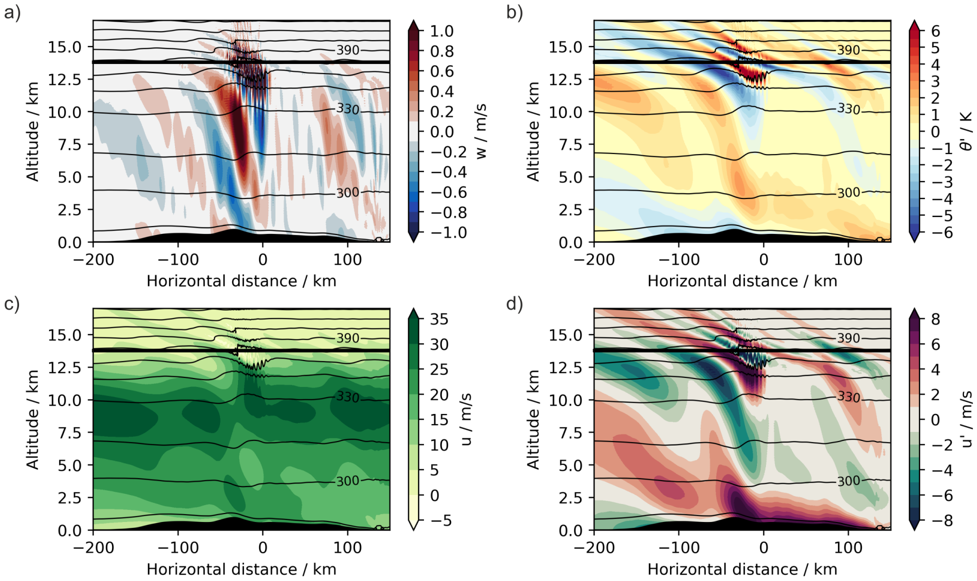

Figure 4.31: Idealized EULAG simulations after 3 h of the (a) vertical wind speed, (b) potential temperature fluctuations, (c) horizontal wind speed and (d) perturbation of the horizontal wind speed. Black contour lines are isentropic surfaces and the thick black line shows the altitude of HALO's flightrack.

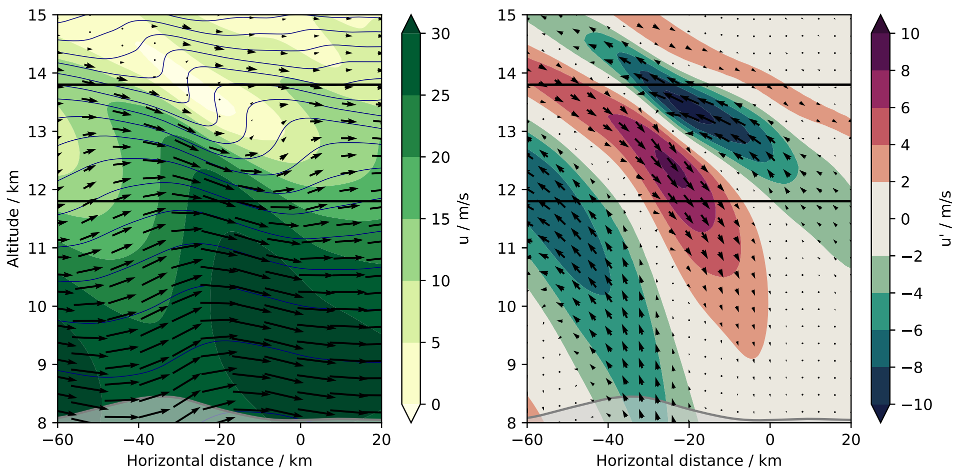

Figure 4.32: Zoom into the total horizontal wind field (a) and the perturbations of the horizontal wind (b) after 2 h. Black arrows refer to the direction and magnitude of the respective horizontal wind speed parameter. Dark blue contour lines are isentropic surfaces and the thick black line shows the altitude of the flightracks of HALO and the French Falcon, respectively. The light gray shaded area indicates the location of the maximum elevation of the topography.

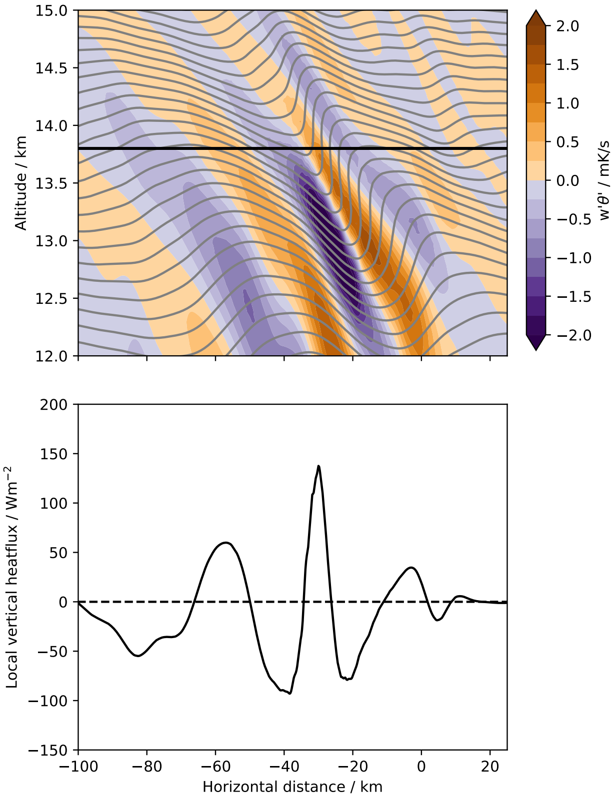

Figure 4.33: Vertical heat flux after 2 h (top panel). Black contour lines are isentropic surfaces and the thick black line shows the altitude of HALO's flight track. The bottom panel shows the local vertical heat flux along the flight track.

by the French Falcon (Fig. 4.32 b). Here, the simulations indicate that these observed changes of the horizontal wind are due to the wave-induced perturbations where the acceleration observed by the French Falcon can be explained with a summation of the wave-induced perturbation and the background horizontal wind due to their similar orientation (Fig. 4.32).

When taking into account the vertical heat flux derived from the simulated vertical wind speed and potential temperature perturbations a pattern of up- and downwards directed heat fluxes associated with the hydrostatic MW is revealed (see Fig 4.33 top panel). Values of the vertical heat flux are maximum in an area characterized by steepening isentropes where the evolution of convective instability is furthered by warm updrafts. At the altitude region of the flight track the simulated heat flux shows a similar pattern between -40 km and -20 km as observed at the turbulence encounter of HALO around 65° N (see Fig 4.33 bottom panel).

Furthermore, EULAG simulations suggest that the observed large-scale perturbations in horizontal wind speed and temperature at and downstream (up to about 66° N) the turbulence encounter are related to MW activity. The perturbation of the horizontal wind speed reveals a pattern of accelerated and decelerated regions related to the large-scale hydrostatic MW along the flight track which are also found in the in situ observations of both aircraft. Also in the fluctuation of the potential temperature large-scale cold and warm anomalies are present due to the described hydrostatic MWs (Fig. 4.31 b).

4.2.5 Discussion

This case study analyzes the dominant processes involved to generate the turbulence encountered by HALO on 13 October 2016 during NAWDEX and their prediction by a global NWP model. Here, 2D idealized simulations proved to sufficiently reproduce essential features of the in situ measurements as e.g. the horizontal scales and the large amplitudes in the vertical wind speed. Also Doyle et al. (2000) were able to simulate the upper-level breaking of MWs with 2D non-hydrostatic models. By using the presented results, the observed turbulence can be attributed to breaking MWs in the lower stratosphere.

Here, a pronounced hydrostatic MW is excited at the mountainous terrain underneath the flighttrack. This MW propagates through the troposphere across the tropopause into the lower stratosphere. In the lower stratosphere the negative vertical shear of the ambient flow causes upstream tilting of the associated phase lines (Fig. 4.31). Additionally, the wave-induced fluctuations in the horizontal wind speed reach similar magnitudes as the decreased ambient wind (Fig 4.32). As the ratio of perturbation to background wind approaches unity, convective instability is likely to produce a self-induced critical level for MWs because their ground-based phase speed is equal to zero (cf. Fritts and Alexander (2003), equation (58)). Therefore, mountain wave breaking occurs even though no ambient critical layer for the stationary MWs exists. In the idealized EULAG simulations these turbulent spots can be identified as regions were locally large positive heat fluxes are present in conjunction with steepening isentropes suggesting wave overturning and turbulent mixing. Furthermore, the large positive vertical heat fluxes derived from HALO in situ observations indicate the presence of convective instability at a comparable location where the maximum turbulence was encountered. Here, the simulated heat fluxes have a similar magnitude as the observed ones. Together, the observations and the simulations suggest that HALO encountered a breaking MW field where the horizontal extent of the observed overturning MW is about 10 km to 20 km. Lidar measurements revealing less than 10% relative humidity over ice close to the flighttrack (Fig. 4.19 b) further support the hypothesis that dry adiabatic processes dominantly caused the observed turbulence.

The presence of strong turbulence is estabilshed by the high magnitudes of the TKE and EDR derived from the in situ observations. Especially the EDR indicates that 'moderate-to-severe' turbulence was encountered by the aircraft in agreement with the pilot report (see also spectra in appendix A.1). The observed encounter was a localized event related to vertically propagating MWs. The maximum turbulence covered a flight distance of about 20 km corresponding to $\approx 5\%$ of the complete flight leg. Light-to-moderate turbulence was detected on about 15% of the leg. Here, the main flight direction was approximately against the mean wind and the longitudinal component of EDR is on average larger compared to the transverse components. In the stall warning study (see Sec. 4.1) the flight direction was transverse to the mean wind and the mean horizontal transverse EDR component was larger. Therefore, the studies indicate that the magnitude of the horizontal EDR component depends on the orientation of the flight with respect to the phase lines of the encountered MWs. This is consistent with Clodman (1957) who analyzed flights passing through turbulent fields at different headings.

With the knowledge of the idealized EULAG simulations, the large amplitudes in the vertical wind speed and the small scale fluctuations superimposed on all measured meteorological parameters of HALO in situ measurements can be related to the breaking MW. Here, the amplitudes of the vertical wind speed are with values of about 6.6 $\mathrm{m\,s^{-1}}$ in the EULAG simulations only $\approx 13\%$ smaller than observed ones. In the simulation domain, also the location of the MW breaking is at a comparable location as the observed turbulence. However, with 50 km the horizontal extent of the simulated breaking region and the resulting downstream trail is only about half the size compared to the measurements. This might be due to the smoothed ECMWF topography used in EULAG simulations in which the slopes are not as steep as in reality and therefore MWs with smaller amplitudes are excited which in turn decreases the potential of breaking. Another possible explanation for this gap might be related to the simplified nature of 2D simulations.

Taking into account French Falcon in situ measurements reveals additional features of the observed atmospheric structures. Upstream of the turbulence encounter the meteorological parameters show similar wave-like structures with a comparable amplitude where the phase lines are tilted upstream when combining the observations. At the turbulence encounter, the temperature and horizontal wind suggest an anti-correlated structure. While the meridional wind increases to about 30 $\mathrm{m\,s^{-1}}$ in the French Falcon observations, it decreases to 0 $\mathrm{m\,s^{-1}}$ in the HALO observations. Together with the EULAG simulations this observation suggests that the two aircraft encountered a breaking MW field. HALO thereby flew through the center of the MW breaking region and the French Falcon through the lower end of this area, respectively. Here, the observations and simulations indicate that the vertical extent of the breaking region is about 2 km. Considering the maximum vertical wind speeds, the breaking area at around 65° N appears to be tilted upstream with altitude. This tilting is also reproduced in the idealized EULAG 2D simulations. The decrease of the maximum observed vertical wind from about 7.6 m s^{-1} to about 3.4 m s^{-1} indicates that the turbulence is reduced at the lower end of the breaking region compared to the center.

Analysis of the Eliassen-Palm relation based on the in situ measurements suggests that HALO was passing through a region dominated by non-linear processes in several ways. On the one hand, the leg-integrated EF_z is by 40% smaller than the respective UMF. On the other hand, an anti-correlation of EF_z and UMF was observed at and downstream the turbulence encounter. In the framework of the Eliassen-Palm theory the energy fluxes EF_z and UMF are equal for freely vertically upward propagating MWs in steady flow with no critical layers. Furthermore, the change in sign in the turbulent-scale energy fluxes (Fig. 4.22 b) indicates the observation of an overturning wave. That way these results are further evidence for the prevailence of non-linear processes in this altitude region (see also the spectra in appendix A.1).

Most of the detected significant energy fluxes are contained in scales which are referred to as the small and turbulent scales (Smith et al. 2016). In agreement with Smith et al. (2016) the detected energy fluxes are rather small with 1 W m^{-2} to 2 W m^{-2} and are less than half of the typical energy fluxes observed during DEEPWAVE (4 W m^{-2}). Therefore these are referred to as fluxless waves. In fact, Smith et al. (2016) argue that EF_z of about 1 W m^{-2} are at the detection threshold of in situ instrumentation. As the measurement uncertainty of HALO is similar to the NSF/NCAR GV, the same threshold can be assumed in this study. During GW-LCYCLE I also so-called fluxless waves were observed (Wagner et al. 2017), however the dominant scales of the horizontal wavelengths are with 15-20 km larger than the ones observed here.

The analyzed turbulence event took place in an atmospheric layer above the tropopause which is characterized by a rapdily decreasing horizontal wind with altitude until a wind minimum is reached. This layer called the "valve layer" (Kruse and Smith 2015) was observed on numerous occasions in New Zealand during DEEPWAVE as well as above Japan in middle and upper (MU) atmosphere-radar measurements (Sato 1990). Satomura and Sato (1999) showed in their numerical study that such a layer is prone to GW breaking due to convective instabilities. Also Doyle et al. (2000) found most pronounced GW breaking in an altitude region from 13 km to 16 km and 18 km to 20 km. Together with the results of this study the questions may be raised if such layers generally enhance occurrence of non-linear processes, how these layers depend on the forcing at ground levels and if consequently those altitude regions are more hazardous to aviation.

Surprisingly, it was rather the larger-scale GWs with a horizontal wavelength of about 20 km downstream of the turbulent region that caused the necessity of pilot's intervention than the turbulence encounter itself. In this region the autopilot could not automatically control the changes in horizontal wind speed any more. As the actual flown Ma depends on the ambient wind speed (Eq. 2.27 and 2.32), it directly impacts the aircraft speed. Autopilots are programmed in a way that aircraft fly at constant Ma at these high altitudes. Aircraft are especially sensitive to speed changes in these regions as air density is low (limiting lift and thrust, see also Sec. 2.2.2 and 2.2.3). Due to the changes in the horizontal wind speed the autothrottle system either fully accelerated or decelerated. Therefore, the pilot had to switch off the auto-throttle system when entering this region. The main scale of the longitudinal wind speed component is about 10 km to 20 km which indicates that aircraft at this altitude region might react especially sensitive to atmospheric modulations at this scale. The breaking at about 65° N with large amplitudes in the vertical wind caused altitude changes of the aircraft of about ± 50 m within approximately 15 s.

Forecasts of the ECMWF IFS reproduce the observed mesoscale structures very well. With a mean difference of about $1\,\mathrm{m\,s^{-1}}$ the horizontal wind forecasts agree in the mean almost perfectly with the measurements. However, when considering the differences in the vertical wind speeds the small-scale structures due to the MW breaking and the consequent turbulence are not captured in the ECMWF IFS forecasts. This is further highlighted when comparing the wavelets of the forecasted and observed horizontal wind speeds. While most of the energy flux is contained in scales $\lesssim 5$ km in the observations, there is almost no energy present in this scale range for the forecasted horizontal wind speeds. As the ECMWF IFS is setup with a horizontal resolution of about 8 km it cannot resolve the dominating small-scales of this event probably leading to the found discrepancy.

Already Doyle et al. (2011) found that prediction of MW breaking and the consequence turbulence is challenging even for numerical models with a horizontal resolution of 1 km. For this case, the largely empirical GTG turbulence forecasts predicted the magnitude of the detected turbulence at the right location. This correct forecast is achieved through the MWT parameter as the CAT parameter underpredicts the turbulence magnitude as was also found by Sharman and Pearson (2017). However, in this study the GTG forecasts show a tendency to overpredict the turbulence magnitude for large areas. Additionally, the observed intermittency of the turbulent field is not reproduced as forecasted turbulent areas are too large due to either inadequate resolution of the input NWP or smoothing of GTG diagnostics.

5 Discussion

In the following the raised hypotheses from section 1.4 are discussed.

5.1 Wind is the dominant atmospheric parameter impacting aircraft speed

An important atmospheric parameter determining aircraft performance is the temperature. Equations 2.33 and 2.34 relate the available lift and thrust of an aircraft to the ambient density. The higher the density the more lift and thrust are available. Through the ideal gas law the density of air depends on the air temperature meaning that the lower the temperature the higher the density and vice versa (at constant pressure). As density generally decreases with altitude in the atmosphere it increasingly limits thrust and lift for aircraft with altitude. Therefore, pilots keep an eye on the temperature display.

Also the aircraft speed can be related to temperature. Depending on altitude and speed different kinds of speeds are used to determine the aircraft speed. At ground level the IAS is used. However, as compressibility effects become more important at higher altitudes and higher speeds, modern aircraft fly according to constant Ma. That way information on the physical characteristics of the flow regime in which the aircraft is moving is retained (Corda 2017).

The analysis presented in section 4.1.6 suggests that it is the horizontal wind speed rather than the temperature that dominantly impacts the aircraft speed. There is no access to the equations programmed to control the autopilot and autothrottle in HALO. However, here the derived correlations are used as experimental evidence that changes of the along track wind are the key driver for changes in Ma.

The found dependence of aircraft Ma to the ambient horizontal wind raises the question, on which scales the ambient horizontal wind changes do affect aircraft the most? So far, the common approach takes into account that aircraft response to changes of atmospheric state parameters depends largely on aircraft parameters such as e.g. size, weight, cruise speed and flight altitude (Sharman et al. 2014). For the majority of commercial aircraft the scales affecting aircraft the most range from 10 m to 1 km

(MacCready 1964, Vinnichenko et al. 1980, Hoblit 1988). However, this approach focuses on the ”bumpiness” felt by an aircraft due to turbulence eddies (Sharman et al. 2014) and is furthermore confined to only vertical motions as aircraft response is considered to be more sensitive in the vertical direction (Hoblit 1988).

As part of the avionic system the autothrottle is designed to automatically control the speed of an aircraft by either reducing or increasing the thrust of the aircraft engines. Due to the dependence of aircraft speed on the ambient horizontal wind and as the aircraft is flying horizontally through this wind field it is especially the horizontal change in horizontal wind to which the autothrottle reacts. Both case studies reveal situations in which HALO was flying through an atmospheric flow field which was modulated by gravity waves with horizontal wavelengths of about 20 km. In these regions the autothrottle system was unable to control the rapid changes of horizontal wind speed and in both cases action of the pilot was required to regain safe flying conditions. That way the case studies suggest that it is horizontal changes on the scale of about 20 km that affect the autothrottle of the avionic system the most. Flying at true air speeds of about 230 m s^{-1} the time it takes to fly through this flow field is less than 90 s which might not be enough time for the avionic system to react appropriately to changes in the ambient conditions. Therefore, the scales affecting the avionic system the most under such circumstances might also depend on the speed of the aircraft and the response time of the avionic system.

5.2 Breaking as well as propagating mountain waves can pose hazards to high-flying aircraft

Turbulence is well recognized as a hazard to commercial aviation especially in the UTLS where most cruising altitudes are located (e.g. Kim and Chun 2010, Kim et al. 2011, Sharman et al. 2012b). At these altitudes passengers and crew are most likely unbuckled (Lester 1994) and therefore turbulence encounters can result in serious injuries (Kim and Chun 2010, Sharman et al. 2012b). Further implications of turbulence on aviation can comprise structural damage of aircraft, fuel losses and flight delays (Kim and Chun 2010).

Turbulence encounters in the UTLS are often related to CAT and therefore difficult to avoid due to their unexpected occurrence without visual indications (Kim et al. 2011, Sharman et al. 2012b). One well acknowledged mechanism leading to CAT is the breaking of MWs (e.g. Clark et al. 2000, Lin 2007, Lane et al. 2009, Ólafsson and Ágústsson 2009, Kim and Chun 2010, Sharman et al. 2012b). Furthermore, Wolff and Sharman (2008) found that preferred regions of turbulence encounter above the United States of America (USA) are located above complex mountainous terrain.

Encountering severe turbulence can lead to structural damage of aircraft frame (e.g. Clark et al. 2000). In the presented study the moderate-to-severe turbulence encountered above Iceland led to altitude changes of the aircraft and passenger discomfort as well as equipment being tossed around. Additionally, the autothrottle could not control the rapid speed changes in horizontal wind speeds located downstream of the breaking MW region.

However, as presented in section 4.1 it is not only the turbulence of breaking MWs leading to hazardous flight conditions. In this study, it was possible to relate the reactions of the autopilot system to modulations of the ambient atmospheric conditions caused by propagating MWs.

Large changes in the horizontal wind speed and temperature field on relatively small horizontal scales of about 20 km were encountered on this flight. The modulation of the horizontal wind speed lead to a deceleration of the aircraft close to the stall speed. Although decreased temperatures increase air density and consequently thrust and lift of the aircraft, the loss of speed could not be compensated by means of full engine thrust and increasing angle of attack. As a last consequence the atmospheric variations lead to the stall warning event of HALO. With analysis of in situ HALO measurements and 3D EULAG simulations the observed atmospheric variations could be related to propagating MWs containing large energy- and momentum fluxes.

A similar effect was observed on the turbulent flightleg above Iceland. Downstream of the MW breaking region HALO encountered changes in the horizontal wind speed in the order of about 5 m s^{-1} to 10 m s^{-1} also with a horizontal scale of approximately 20 km. This time the autothrottle part of the avionic system was affected. The encountered changes were too large for the autothrottle system to properly control the aircraft speed as it issued either full thrust or no thrust at all to keep aircraft speed constant. Therefore, the commanding pilot had to switch off the autothrottle system in the course of the event. As the vertical heat flux and the vertical energy flux EF_z indicate the presence of propagating GWs of similar scale as the undulations in the horizontal wind in this region the observed changes in horizontal wind can again be attributed to propagating GWs.

The case studies indicate that the effects of propagating MWs are especially important for aircraft flying at high altitudes (i.e. z > FL 200). At these altitudes air density is decreased which affects aircraft flying conditions in two ways: on the one hand, thrust and lift are reduced as these depend on the density of ambient air (see Eq. 2.33 and Eq. 2.34) which in turn limits the possibilities to react rapidly to changing atmospheric conditions by means of e.g. issuing full thrust. On the other hand, the maximum and minimum possible aircraft speeds come closer together in the flight envelope which in turn reduces the margin under which safe flying conditions are established (therefore pilots call this "coffin corner"). In the case study described in section 4.1 it was the combination of both effects that lead to the encountered stall warning.

Furthermore the case studies suggest that turbulence generated by breaking MWs and propagating MWs affect high-flying aircraft in different ways. Breaking MWs and its associated turbulence seem to have a more "outside" effect on the aircraft as e.g. structural damage (e.g. Clark et al. 2000, Kim and Chun 2010). Propagating MWs and the associated modulation of the horizontal wind speed and temperature field on the other hand affect more the avionic system on the "inside" of the aircraft. As the avionic system is responsible to ensure safe flight conditions by e.g. keeping the aircraft speed inside the limits prescribed by the flight envelope, it is of equal importance.

5.3 Current forecast tools do not accurately predict the observed incidents

5.3.1 ECMWF Forecasts and Operational Analyses

Forecasts and operational analyses of the ECMWF IFS are widely used for operational weather forecasts as well as scientific studies. This dataset was for example employed to extract ambient atmospheric conditions for excitation and propagation conditions of GWs (e.g. Blum et al. 2004, Ehard et al. 2017).

However, on the other side it is also used to directly compare resolved GWs with measurements. In this context ECMWF data were compared to radiosonde observations (Plougonven and Teitelbaum 2003) and satellite observations (Wu and Eckermann 2008, Schroeder et al. 2009). In these studies both an underestimation of GW amplitudes and a misrepresentation of horizontal wavelengths was found (Plougonven and Teitelbaum 2003).

In 2016 a major update of the operational system of the ECMWF, the cycle 41r2 was introduced. In this course the horizontal grid resolution was increased from 16 km to 9 km (Malardel and Wedi 2016). That way GWs are now better resolved leading to enhanced agreements of observed and forecasted mesoscale temperature anomalies (Dörnbrack et al. 2017).

In both presented case studies ECMWF IFS forecasts reproduce the observed large-scale structures very well. Here, the best agreement was found for the components of the horizontal wind with a mean difference of about 1 m s^{-1}. Also for the large-scale pattern of the temperature very good agreement was found.

However, in areas dominated by large gradients and small-scale structures (i.e. area of stall warning event and turbulence encounter) the observations cannot be reproduced due to inadequate resolution of the ECMWF IFS. In concurrence with Plougonven and Teitelbaum (2003), Wu and Eckermann (2008), Schroeder et al. (2009), the forecasts underestimate the amplitudes in these regions compared to the measured ones. For the stall warning event the gradients are underestimated by about 18% of the observation for the temperature and by -6% of the meridional wind. During the strong turbulence encounter the temperature gradient is underestimated by about 50 % of the observations while the gradients of the meridional wind is reproduced in a similar order of magnitude. The underestimation of amplitudes and gradients in these areas may be related to the limited resolution of the ECMWF IFS.

5.3.2 GTG Turbulence Forecasts

State of the art operational NWP models are not capable to explicitly resolve turbulence due to limited horizontal resolution (Sharman et al. 2006, Kim et al. 2011, Sharman and Pearson 2017, Kim et al. 2018). Therefore, the turbulent potential of the atmosphere is derived from current NWP models by assuming that a downward energy cascade from resolved large-scale atmospheric motions to the unresolved turbulent scales exists (Sharman et al. 2006, Kim et al. 2011, Sharman and Pearson 2017).

To ackowledge that turbulence generation is related to various atmospheric processes as e.g. convection, shear instability, MW breaking, different diagnostics are used to derive the turbulent potential of the atmosphere. In the GTG different diagnostics and approaches are applied to forecast CAT and MWT.

In the turbulence case study above Iceland (Sec. 4.2), the magnitude and region of the maximum observed turbulence was forecasted correctly due to the use of the MWT parameter. However, when combining the two analysed studies, the GTG shows a clear tendency to overpredict turbulence for large areas which is in agreement with Sharman and Pearson (2017). Additionally, in both studies the observed intermittency was not reproduced by the forecasts. Thus large turbulent areas are predicted where actually no aviation related turbulence was encountered. This might be due to the limited resolution of the input NWP or due to smoothing effects within the GTG. That way the ability of the GTG to correctly predict turbulence also depends on the input NWP (e.g. ECMWF vs. WRF). Therefore, overall limited capability to accurately forecast the turbulence encounters was found with the GTG.

6 Summary and Conclusion

In this thesis two case studies are presented in which variations of the atmospheric state parameters temperature and horizontal wind speed affected aircraft performance in different ways. The cause of these variations is attributed to enhanced mountain wave (MW) activity in the respective regions. While in the first study a stall warning event is analyzed, the second case study addresses a strong turbulence encounter. An extensive data set comprising high-resolution in situ aircraft measurements, data of the quick access recorder of the High Altitude LOng Range Research Aircraft (HALO), high-resolution 2D and 3D Eulerian semi-Lagrangian fluid solver (EULAG) simulations, European Centre for Medium-Range Weather Forecasts (ECMWF) Integrated Forecast System (IFS) forecasts and operational analyses as well as turbulence predictions of the Graphical Turbulence Guidance Tool (GTG), is available for the case studies. Therefore these case studies provide a unique opportunity to study in detail what atmospheric processes caused the respective event and how these affected the research aircraft as well as their predictability by conventional forecasting methods.

The analyzed case studies reveal different mechanisms how MW activity impacts high flying aircraft. During the stall warning event, large variations in the horizontal wind speed and temperature were encountered by HALO when laterally entering a propagating large amplitude MW above the Apennines, Italy. The sequence of these variations was distributed along the flight track in such a way that the aircraft speed reduced to values close to the stall speed. Consequently the commanding pilot had to switch off the autopilot system and descend to lower flight levels. In the second case a strong turbulence event was encountered above Iceland where during it's course the autothrottle system had to be deactivated and altitude changes of about 50 m were experienced. In both cases the research aircraft HALO was affected by enhanced MW activity, however in different ways. While the first case is dominated by nearly propagating MWs in the latter case non-linear processes as MW breaking played an essential role.

In general, it is both temperature and the horizontal wind speed that affect aircraft performance. While it is well established that temperature variations impact aircraft performance parameters such as lift and thrust the question was addressed which atmospheric parameters dominantly influences aircraft speed. The speed of aircraft flying at high speeds and high altitudes ($z > 5\,\mathrm{km}$) is determined by the Ma where fundamentally Ma depends on the temperature. However, combining the data set of the two studies revealed that it is the horizontal wind speed in the direction of the flight track which impacts the aircraft speed the most. Here, the horizontal scale of the horizontal wind variations was about 20 km - 30 km in both studies.

Furthermore, the presented case studies suggest that the impact of horizontal speed variations on aircraft can differ from each other. In the analyzed stall warning event the encountered variations lowered the aircraft speed towards the minimum needed speed to avoid a stall situation. Above Iceland on the other side, the changes in horizontal wind speed became uncontrollable to the auto-throttle system of HALO as the system either initiated full thrust or no thrust at all. Therefore, the pilot had to deactivate this system in the course of this encounter although the actual aircraft speed was still well above the stall speed.

The encountered variations in horizontal wind speed leading to the deactivation of the auto-throttle system were attributed to turbulence by the pilot. However, analysis of the distribution of turbulence along the flight leg shows no indication of enhanced turbulence in this region. Taking into account high-resolution EULAG simulations the associated changes are located outside the turbulent region where possibly secondary gravity waves (GWs) prevail. This raises the question how many Pilot Reports (PIREPs) regarding turbulence are in reality related to GW activity.

Up to today in aviation propagating MWs are considered mainly as a source generating atmospheric hazards to aviation such as e.g. rotors or down-slope windstorms. Furthermore special attention is payed to the breaking of MWs because it is one mechanism responsible for the production of Clear Air Turbulence (CAT). However, in both presented case studies aircraft speed was primarily affected by variations in the atmospheric state on horizontal length scales of about 20 km to 30 km which are too large to be attributed to turbulence. Taking into account idealized high-resolution EULAG simulations these variations could be attributed to propagating MWs in the stall warning case study. By that way it was found that also nearly linearly propagating MWs can pose potential hazard to high flying aircraft. Together, the case studies imply that both breaking and propagating MWs can cause hazardous flight situations. Therefore, this result suggests that also propagating MWs should be taken into account in flight planning procedures especially for high-flying aircraft where the margin between stall speed and maximum possible aircraft speed is small.

The predictability of the two described events was validated with ECMWF IFS forecasts and operational analyses as well as GTG turbulence predictions. While the general large scale trend is reproduced very well by ECMWF predictions, the small scale variations especially during the turbulence encounter are not captured. Generally, predictions show more skill in forecasting the temperature and horizontal wind speed than in predicting amplitudes in the vertical wind speed which are largely underestimated. This might be related to the insufficient horizontal resolution. Turbulence forecasts of the GTG accurately predicted the magnitude and location of the maximum encountered turbulence in the second case study. However, taking both case studies together a general trend to overprediction is found for the turbulence forecasts where also the observed intermittency is not reproduced.

Altogether in this thesis the impact of turbulence and propagating MWs on high flying aircraft could be quantified for the first time. Additionally this thesis revealed that in flight planning of high altitude flights it is advisable to also consider propagating MW as a potential hazard. Furthermore the presented analysis reveals that still the turbulence potential needs to be derived from large NWPs using empirical diagnostics as their setup and resolution is not sufficient to capture atmospheric processes on these small scales.

A Appendix

A.1 Spectra

The influence of different atmospheric processes on the shape of spectra is studied with data of the turbulent flight leg above Iceland. For this analysis the flightleg of the turbulence case study is subdivided into different parts with regard to the Eliassen-Palm fluxes. That way three different parts of the flight are identified where either GW structures or turbulence dominate. Upstream of Iceland a so-called "calm" area is defined where neither of the mentioned processes in particular take effect. Table A.1 gives an overview on the extent the respective areas cover.

Table A.1: Overview on the extent of the four denoted regions.

	Latitude
Calm	63° N - 64° N
Wave I	64° N - 64.8° N
Turbulence	64.8° N - 65.8° N
Wave II	65.8° N - 67.3° N
Zonal Wind	$1.41 \pm 3.92\,\mathrm{m\,s^{-1}}$

Overall, relatively good agreement with the Kolmogorov slope of -5/3 is found in the parts where wave activity or turbulence dominate for all three wind components. Surprisingly, it is the "wave I" part which agrees on average best with the Kolmogorov -5/3 spectrum with a mean slope of about -1.76. However, confining the analysis to a maximum horizontal wavelength of about 10 km the slope in the turbulent region follows the Kolmogorov -5/3 slope best without any significant peaks. The "calm" area on the other hand, reveals least agreement with the Kolmogorv -5/3 slope and even undulates around this slope especially in the vertical wind component. The mean slope in the calm area is about -2.

As expected highest energies are found in the turbulent section of the flight leg. The energy levels in the "wave II" and calm parts are similar. This might be due to the fact

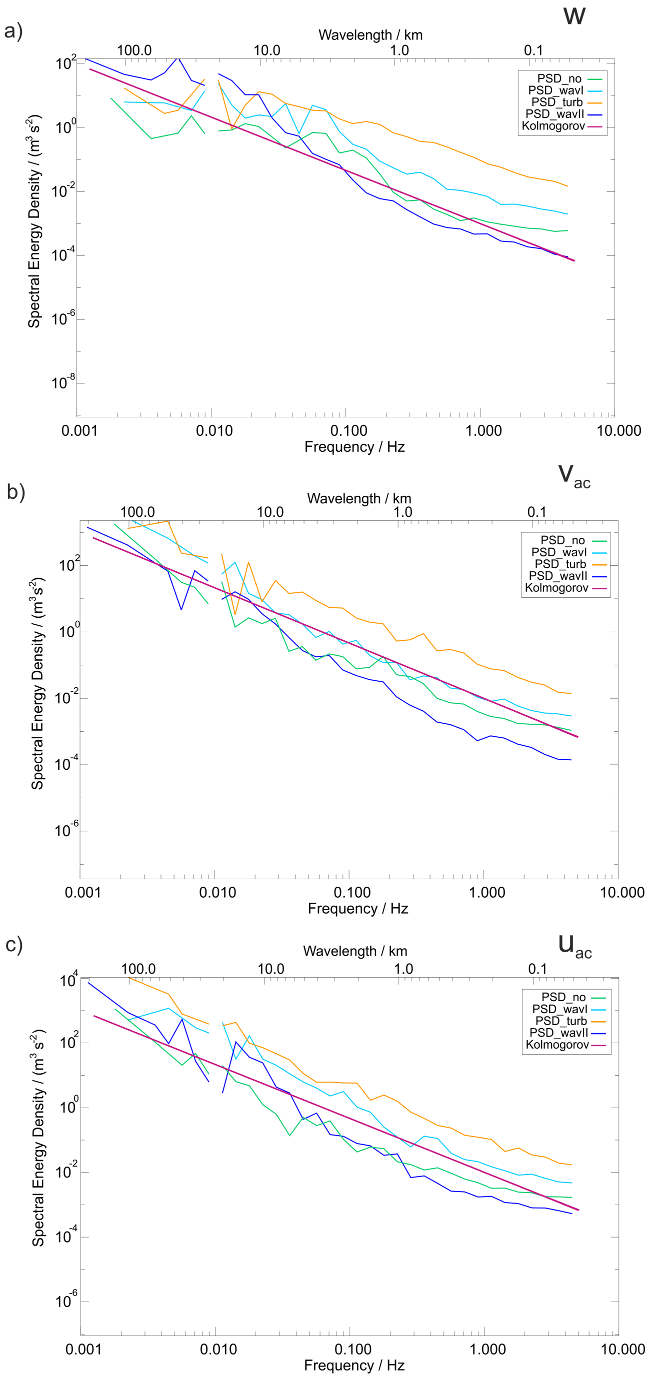

Figure A.1: Power Spectral Density of the vertical wind (a), the horizontal transverse wind (b) and the horizontal longitudinal wind, respectively. The color coding refers to the part of the leg over which the spectra is calculated while the red line refers to the Kolmogorov -5/3 spectrum. Data have been linearly detrended before applying discrete Fourier transformation. Additionally, smoothing through equal log intervals was used.

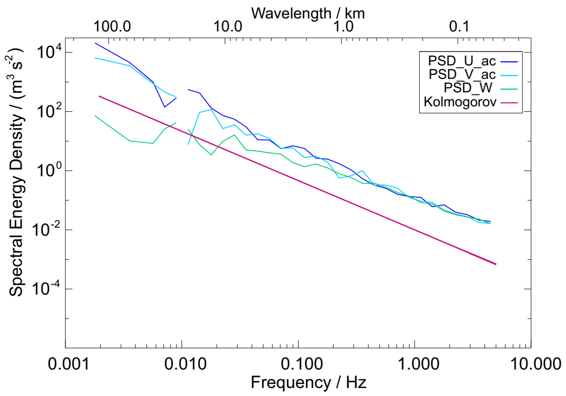

Figure A.2: Power Spectral Density of the vertical wind (green), the horizontal transverse wind (light blue) and the horizontal longitudinal wind (dark blue) in the turbulent region of the flight leg. The red line refers to the Kolmogorov -5/3 spectrum. Data have been linearly detrended before applying discrete Fourier transformation. Additionally, smoothing through equal log intervals was used.

that the ”wave II” part also contains regions without significant wave energy especially north of Iceland.

The vertical wind spectrum reveals peaks for horizontal wavelengths smaller than about 10 km while in the ”wave I” part peaks at a horizontal wavelength of about 3 km and 8 km are present. These peaks are probably related to GW activity. However, in the spectra of the horizontal wind components such peaks are present only at horizontal wavelengths larger than 10 km. Therefore, the spectra of the two horizontal wind components show the best agreement with the Kolmogorov -5/3 slope up to a horizontal wavelength of about 10 km in particular in the turbulent region.

Thus, this analysis suggests that the different processes observed along the flight can affect the shape of the spectrum in different ways.

A.2 GTG Diagnostics

The GTG uses a different set of diagnostics depending on the altitude region. In the following an overview on the different diagnostics employed in the respective altitudes for the ECMWF setup is given. Here, the term low levels refers to all flight levels $\leq$ FL100, mid levels enclose flight levels from FL100 to FL200 and high levels include flight levels from FL200 to FL500.

Table A.2: CAT diagnostics employed in the ECMWF setup of the GTG

Low levels	Mid levels	High levels
$U\cdot$ |Deformation|	$U\cdot$ |Deformation|	Ellrod 1
1/SATRi	EDR	Fth/Ri
LHFK/Ri	1/RiTw	DEFSQ
w^2	iawind/Ri	|Div|/Ri
SIGW/Ri	F3D/Ri	EDRRCH
		EDR
		SEDR/Ri
		1/RiTw
		$\mid \frac{\partial T}{\partial z} \mid x$ |deformation|/Ri
		EDRLun
		w^2/Ri
		SIGW/Ri
		F2D/Ri

Table A.3: MWT diagnostics employed in the ECMWF setup of the GTG

Low levels	Mid levels	High levels
$d_s\cdot$speed (MWT4)	$d_s\cdot$iawind/Ri (MWT9)	$d_s\cdot$CTsq (MWT2)
$d_s \cdot U\cdot$ |Deformation| (MWT6)	$d_s\cdot$ |TEMPG| (MWT12)	$d_s\cdot$F3D (MWT3)
$d_s\cdot$SIGW (MWT7)		

In this context SATRi is the Richardson number (Ri) calculated for saturated conditions, LHFK is the Lighthill Ford Knox Index (Knox et al. 2008), SIGW refers to the variance of the vertical wind speed w, EDR is the EDR calculated according to Frehlich and Sharman (2004), RiTw is the Richardson number where the vertical wind speed is derived from the thermal wind relation (Sharman et al. 2006), iawind is the inertial advective wind speed (McCann 2001), F3D refers to the 3D frontogenesis function $F = \frac{D}{Dt} \mid \bigtriangledown\theta \mid$, Ellrod 1 is the Ellrod index (Ellrod and Knapp 1992), Fth is the normalized 2D frontogenesis function computed on isentropic surfaces, DEFQ is the squared deformation, Div is the horizontal divergence, EDRRCH is the EDR derived from a simplified Richardson tendency equation (Roach 1970), SEDR is the EDR derived from the turbulent kinetic energy (Schumann 2012), EDRLun is the EDR derived from a simplified Richardson tendency function according to Gill and Buchanan (2014), F2D is the 2D frontogenesis function.

For the MWT prediction a subset of all available CAT diagnostics is used. Here, speed refers to the horizontal wind speed, TEMPG is the horizontal temperature gradient, CTsq is the temperature structure constant estimated from the average of the longitudinal and transverse second-order structure functions of the temperature (Frehlich et al. 2010) and d_s is the near-surface diagnostic (Sharman and Pearson 2017).

A.3 Derivation of Equation 2.28

The following derivation is based on Corda (2017). Starting with the conservation of energy equation for steady, inviscid and adiabatic flow

$$c_pT_s + \frac{v^2}{2} = c_pT_t = const.intheflowfield \tag{A.1}$$

where T_s is the static temperature, c_p the specific heat at constant pressure, v velocity of the flow and T_t the total temperature (Corda 2017).

Division with c_pT_s leads to

$$\frac{T_t}{T_s} = 1 + \frac{v^2}{2c_pT_s}. \tag{A.2}$$

Taking into account the relation of c_p to the specific gas constant R and the ratio of specific heats γ with $c_p = \frac{\gamma R}{\gamma-1}$ leads to

$$\frac{T_t}{T_s} = 1 + \frac{v^2}{\frac{2}{\gamma-1}\gamma RT_s}. \tag{A.3}$$

Using the definition of speed of sound $a = \sqrt{\gamma RT}$ and the definition of the Mach number $Ma = \frac{v}{a}$, the ratio of total-to-static temperature can be related to Ma with

$$\frac{T_t}{T_s} = 1 + \left(\frac{\gamma-1}{2}\right) Ma^2 \tag{A.4}$$

With the assumption of isentropic flow, Eq. A.4 the isentropic relation $\frac{p_2}{p_1} = \left(\frac{T_2}{T_1}\right)^{\gamma/(\gamma-1)}$ can be employed and an isentropic relation for the total-to-static pressure can be obtained with

$$\frac{p_t}{p_s} = \left[1 + \left(\frac{\gamma-1}{2}\right) Ma^2\right]^{\gamma/(\gamma-1)} \tag{A.5}$$

where p_t is the total pressure and p_s determines the static pressure. Solving Eq. A.5 for Ma yields

$$Ma = \sqrt{\frac{2}{\gamma - 1}\left[\left(\frac{p_t}{p_s}\right)^{(\gamma-1)/\gamma} - 1\right]}. \tag{A.6}$$

In terms of the pressure difference $\Delta p = p_t - p_s$ the above equation leads to

$$Ma = \sqrt{\frac{2}{\gamma - 1}\left[\left(\frac{\Delta p}{p_s} + 1\right)^{(\gamma-1)/\gamma} - 1\right]}. \tag{A.7}$$

Acronyms

AIRMET Airmen's Meteorological Information

AOA Angle of Attack

BAHAMAS Basic HALO Measurement and Sensor System

CAS Calibrated Airspeed

CAT Clear Air Turbulence

DEEPWAVE Deep Propagating gravity WAVe Experiment

DLR German Aerospace Center

EAS Equivalent Airspeed

ECMWF European Centre for Medium-Range Weather Forecasts

EDR eddy dissipation rate

EULAG Eulerian semi-Lagrangian fluid solver

EUMETNET European Meteorological Services Network

FAAM Facility for Airborne Atmospheric Measurements

FL flight level

GLORIA Gimballed Limb Observer for Radiance Imaging of the Atmosphere

GPS global positioning system

GTG Graphical Turbulence Guidance Tool

GW gravity wave

GW-LCYCLE Life Cycle of Gravity Waves

HALO High Altitude LOng Range Research Aircraft

IAS Indicated Airspeed

IFS Integrated Forecast System

ILES implicit large eddy simulation

MW mountain wave

MWT Mountain Wave Turbulence

NAWDEX North Atlantic Waveguide and Downstream Impact Experiment

NCAR National Center for Atmospheric Research

NFT Nonoscillatory Forward-in-Time

NWP Numerical Weather Prediction

PIREP Pilot Report

QAR Quick Access Recorder

Safire Service des Avions Francais Instrumentés pour la Recherche en Environnement

SIGMET Significant Meteorological Information

T-REX Terrain-Induced Rotor Experiment

TAS True Airspeed

TKE turbulent kinetic energy

USA United States of America

UTLS upper troposphere and lower stratosphere

Symbols

Sign	Description	Unit
A_θ	amplitude of potential temperature perturbation	K
A_p	amplitude of pressure perturbation	hPa
A_u	amplitude of zonal wind perturbation	m s^{-1}
A_v	amplitude of meridional wind perturbation	m s^{-1}
A_w	amplitude of vertical wind perturbation	m s^{-1}
A	area	m^2
C_L	lift coefficient	
EF_z	vertical energy flux	W m^{-2}
EF_{zM}	vertical energy flux derived from momentum fluxes	W m^{-2}
HF	vertical heat flux	W m^{-2}
H	density scale height	m
L	lift	kg m s^{-2}
MF_x	zonal component of the vertical momentum flux	Pa
MF_y	meridional component of the vertical momentum flux	Pa
Ma	Mach number	
N	Brunt-Väisälä frequency	s^{-1}
Ri	Richardson number	
R	ideal gas constant	J kg^{-1}K^{-1}
S_i	spectral energy density of respective wind component	m^3 s^{-2}
T'	temperature perturbation	K
Thr	thrust	kg m s^{-2}
T	temperature	K
U	background horizontal wind	m s^{-1}
V_∞	freestream velocity (aerodynamic)	m s^{-1}
V_{Ex}	flow velocity at exhaust of engine	m s^{-1}
V	flow velocity (aerodynamic)	m s^{-1}
Ω	intrinsic wave frequency	s^{-1}
α_i	Kolmogorov constant of respective wind component	
α	angle of attack	degree
$\bar{\rho}$	background density	kg m^{-3}
$\bar{\theta}$	background potential temperature	K

Sign	Description	Unit
$\bar{u}$	background zonal wind	m s^{-1}
$\bar{v}$	background meridional wind	m s^{-1}
$\dot{m}$	mass flow rate	kg s^{-1}
ℓ	Scorer parameter	m^{-1}
ϵ	energy dissipation rate	m^2 s^{-3}
γ	ratio of specific heats	
λ_x	zonal wavelength	m
λ_y	meridional wavelength	m
λ_z	vertical wavelength	m
ω	ground based frequency	s^{-1}
ρ'	density perturbation	kg m^{-3}
ρ_{SL}	density at standard sea level	kg m^{-3}
ρ	density	kg m^{-3}
σ_i	variance of respective wind component	m^2 s^{-1}
θ'	potential temperature perturbation	K
θ	potential temperature	K
$\widetilde{EF}_n$	cospectrum of vertical energy flux	W m^{-2}
$\widetilde{HF}_n$	cospectrum of vertical heat energy flux	W m^{-2}
$\widetilde{MF}_n$	cospectrum of vertical flux of horizontal momentum	W m^{-2}
a	speed of sound	m s^{-1}
c_p	specific heat at constant pressure	J kg^{-1}K^{-1}
c_{gx}	zonal ground based group velocity	m s^{-1}
c_{gy}	meridional ground based group velocity	m s^{-1}
c_{gz}	vertical group velocity	m s^{-1}
c_{ph}	horizontal phase velocity	m s^{-1}
c_{px}	zonal phase velocity	m s^{-1}
c_{py}	meridional phase velocity	m s^{-1}
c_{pz}	vertical phase velocity	m s^{-1}
f	Coriolis parameter	s^{-1}
g	gravitational acceleration	m s^{-2}
k_h	horizontal wavenumber	m^{-1}
k	zonal wavenumber	m^{-1}
l	meridional wavenumber	m^{-1}
m	vertical wavenumber	m^{-1}
p'	pressure perturbation	Pa
p_0	reference pressure (1000 hPa)	hPa
p_s	static pressure	Pa
p_t	total pressure	Pa
p	pressure	Pa
s	flight distance	m
t	time	s

Sign	**Description**	**Unit**
u'	zonal wind perturbation	m s^{-1}
u_{ac}	along-track wind component with respect to aircraft	m s^{-1}
u	zonal wind	m s^{-1}
v'	meridional wind perturbation	m s^{-1}
v_C	calibrated airspeed	m s^{-1}
v_E	equivalent airspeed	m s^{-1}
v_G	groundspeed	m s^{-1}
v_I	indicated airspeed	m s^{-1}
v_T	true airspeed	m s^{-1}
v_{ac}	hor. cross-track wind component with respect to aircraft	m s^{-1}
v_{rel}	relative speed between the aircraft and the horizontal wind speed v_{wind} in the direction along the aircraft	m s^{-1}
v_{wind}	wind speed	m s^{-1}
v	meridional wind	m s^{-1}
w	vertical wind perturbation	m s^{-1}

Bibliography

Amante, C., and B. W. Eakins, 2009: ETOPO1 Global Relief Model converted to PanMap layer format. PANGAEA, doi:10.7289/V5C8276M.

Bacmeister, J. T., M. R. Schoeberl, L. R. Lait, P. A. Newman, and B. Gary, 1990: ER-2 mountain wave encounter over Antarctica: Evidence for blocking. *Geophys. Res. Lett.*, **17 (1)**, 81–84, doi:10.1029/GL017i001p00081.

Baines, P., 1995: *Topographic Effects in Stratified Flows.* Cambridge Univ. Press, Cambridge, 482 pp.

Bauer, P., A. Thorpe, and G. Brunet, 2015: The quiet revolution of numerical weather prediction. *Nature*, **525**, 47–55, doi:10.1038/nature14956.

Blum, U., K. H. Fricke, G. Baumgarten, and A. Schöch, 2004: Simultaneous lidar observations of temperatures and waves in the polar middle atmosphere on the east and west side of the Scandinavian mountains: a case study on 19/20 January 2003. *Atmos. Chem. Phys.*, **4 (3)**, 809–816, doi:10.5194/acp-4-809-2004.

Bougeault, P., A. J. Clar, B. Benech, B. Carissimo, J. Pelon, and E. Richard, 1990: Momentum Budget over the Pyrénées: The PYREX Experiment. *Bull. Amer. Meteor. Soc.*, **71 (6)**, 806–818, doi:10.1175/1520-0477(1990)071⟨0806:MBOTPT⟩2.0.CO;2.

Bougeault, P., A. Jansa, J. Attié, I. Beau, B. Benech, R. Benoit, P. Bessemoulin, J. Caccia, J. Campins, B. Carissimo, J.-L. Champeaux, M. Crochet, A. Druilhet, P. Durand, A. Elkhalfi, P. Flamant, A. Genovés, M. Georgelin, K. Hoinka, V. Klaus, E. Koffi, V. Kotroni, C. Mazaudier, J. Pelon, M. Petitdidier, Y. Pointin, D. Puech, E. Richard, T. Satomura, J. Stein, and D. Tannhauser, 1993: The Atmospheric Momentum Budget over a major mountain range : first results of the PYREX field program. *Ann. Geophys.*, **11**, 395–418.

Bougeault, P., P. Binder, A. Buzzi, R. Dirks, J. Kuettner, R. Houze, R. B. Smith, R. Steinacker, and H. Volkert, 2001: The MAP Special Observing Period. *Bull. Amer. Meteor. Soc.*, **82 (3)**, 433–462, doi:10.1175/1520-0477(2001)082⟨0433:TMSOP⟩2.3.CO;2.

Bramberger, M., A. Dörnbrack, H. Wilms, S. Gemsa, K. Raynor, and R. Sharman, 2018: Vertically Propagating Mountain Waves - A Hazard for High-Flying Aircraft? *J. Appl. Meteor. Climatol.*, **57 (9)**, 1957–1975, doi:10.1175/JAMC-D-17-0340.1.

Bramberger, M., A. Dörnbrack, K. Bossert, B. Ehard, D. C. Fritts, B. Kaifler, C. Mallaun, A. Orr, P.-D. Pautet, M. Rapp, M. J. Taylor, S. Vosper, B. P. Williams, and B. Witschas, 2017: Does Strong Tropospheric Forcing Cause Large-Amplitude Mesospheric Gravity Waves? A DEEPWAVE Case Study. *J. Geophys. Res. Atmos.*, **122 (21)**, 11,422–11,443, doi:10.1002/2017JD027371, 2017JD027371.

Brandt, S., 2004: *Introduction to Aeronautics: A Design Perspective*. AIAA education series, American Institute of Aeronautics & Astronautics.

Calmer, R., G. C. Roberts, J. Preissler, K. J. Sanchez, S. Derrien, and C. O'Dowd, 2018: Vertical wind velocity measurements using a five-hole probe with remotely piloted aircraft to study aerosol–cloud interactions. *Atmos. Meas. Tech.*, **11 (5)**, 2583–2599, doi:10.5194/amt-11-2583-2018.

Champagne, F. H., 1978: The fine-scale structure of the turbulent velocity field. *J. Fluid Mech.*, **86 (1)**, 67–108, doi:10.1017/S0022112078001019.

Chan, K. R., L. Pfister, T. P. Bui, S. W. Bowen, J. Dean-Day, B. L. Gary, D. W. Fahey, K. K. Kelly, C. R. Webster, and R. D. May, 1993: A case study of the Mountain Lee Wave Event of January 6, 1992. *Geophys. Res. Lett.*, **20 (22)**, 2551–2554, doi:10.1029/93GL01964.

Clark, T. L., W. D. Hall, R. M. Kerr, D. Middleton, L. Radke, F. M. Ralph, P. J. Neiman, and D. Levinson, 2000: Origins of Aircraft-Damaging Clear-Air Turbulence during the 9 December 1992 Colorado Downslope Windstorm: Numerical Simulations and Comparison with Observations. *J. Atmos. Sci.*, **57 (8)**, 1105–1131, doi:10.1175/1520-0469(2000)057⟨1105:OOADCA⟩2.0.CO;2.

Clark, T. L., and W. R. Peltier, 1984: Critical Level Reflection and the Resonant Growth of Nonlinear Mountain Waves. *J. Atmos. Sci.*, **41 (21)**, 3122–3134, doi:10.1175/1520-0469(1984)041⟨3122:CLRATR⟩2.0.CO;2.

Clodman, J., 1957: Anisotropic high-level turbulence. *Quart. J. Roy. Meteor. Soc.*, **83 (355)**, 116–120, doi:10.1002/qj.49708335511.

Coffel, E., and R. Horton, 2015: Climate change and the impact of extreme temperatures on aviation. *Wea. Climate Soc.*, **7 (1)**, 94–102, doi:10.1175/WCAS-D-14-00026.1.

Corda, S., 2017: *Introduction to Aerospace Engineering with a Flight Test Perspective*. Aerospace Series, Wiley.

Cornman, L. B., 2016: Airborne In Situ Measurements of Turbulence. *Aviation Turbulence*, R. Sharman, and T. Lane, Eds., Springer, Cham.

Cornman, L. B., C. S. Morse, and G. Cunning, 1995: Real-time estimation of atmospheric turbulence severity from in-situ aircraft measurements. *J Aircr*, **32 (1)**, 171–177, doi:10.2514/3.46697.

Delay, R. D., and J. A. Dutton, 1971: An Analysis of Conditions Associated with an Occurrence of Stratospheric CAT. *J. Atmos. Sci.*, **28 (7)**, 1272–1279, doi:10.1175/1520-0469(1971)028⟨1272:AAOCAW⟩2.0.CO;2.

Dörnbrack, A., 1998: Turbulent mixing by breaking gravity waves. *J. Fluid Mech.*, **375**, 113–141, doi:10.1017/S0022112098002833.

Dörnbrack, A., S. Gisinger, M. C. Pitts, L. R. Poole, and M. Maturilli, 2017: Multilevel Cloud Structures over Svalbard. *Mon. Wea. Rev.*, **145 (4)**, 1149–1159, doi:10.1175/MWR-D-16-0214.1.

Dörnbrack, A., R. Heise, and J. P. Kuettner, 2006: Wellen und Rotoren. *promet*, **32**, 18–24.

Doyle, J. D., M. A. Shapiro, Q. Jiang, and D. L. Bartels, 2005: Large-Amplitude Mountain Wave Breaking over Greenland. *J. Atmos. Sci.*, **62 (9)**, 3106–3126, doi:10.1175/JAS3528.1.

Doyle, J. D., D. R. Durran, C. Chen, B. A. Colle, M. Georgelin, V. Grubišić, W. R. Hsu, C. Y. Huang, D. Landau, Y. L. Lin, G. S. Poulos, W. Y. Sun, D. B. Weber, M. G. Wurtele, and M. Xue, 2000: An Intercomparison of Model-Predicted Wave Breaking for the 11 January 1972 Boulder Windstorm. *Mon. Wea. Rev.*, **128 (3)**, 901–914, doi:10.1175/1520-0493(2000)128⟨0901:AIOMPW⟩2.0.CO;2.

Doyle, J. D., S. Gaberšek, Q. Jiang, L. Bernardet, J. M. Brown, A. Dörnbrack, E. Filaus, V. Grubišić, D. J. Kirshbaum, O. Knoth, S. Koch, J. Schmidli, I. Stiperski, S. Vosper, and S. Zhong, 2011: An Intercomparison of T-REX Mountain-Wave Simulations and Implications for Mesoscale Predictability. *Mon. Wea. Rev.*, **139 (9)**, 2811–2831, doi:10.1175/MWR-D-10-05042.1.

Dutton, J. A., 1969: An Energy Budget for a Layer of Stratospheric CAT. *Radio Science*, **4 (12)**, 1137–1142, doi:10.1029/RS004i012p01137.

Eckermann, S. D., A. Dörnbrack, H. Flentje, S. B. Vosper, M. J. Mahoney, T. P. Bui, and K. S. Carslaw, 2006: Mountain Wave-Induced Polar Stratospheric Cloud Forecasts for Aircraft Science Flights during SOLVE/THESEO 2000. *Wea. Forecasting*, **21 (1)**, 42–68, doi:10.1175/WAF901.1.

Ehard, B., B. Kaifler, A. Dörnbrack, P. Preusse, S. D. Eckermann, M. Bramberger, S. Gisinger, N. Kaifler, B. Liley, J. Wagner, and M. Rapp, 2017: Horizontal propagation of large-amplitude mountain waves into the polar night jet. *J Geophys Res Atmos*, **122 (3)**, 1423–1436, doi:10.1002/2016JD025621, 2016JD025621.

Eliassen, A., and E. Palm, 1961: On the transfer of energy in stationary mountain waves. *Geofys. Publ.*, **22**, 1–23.

Ellrod, G. P., and D. I. Knapp, 1992: An Objective Clear-Air Turbulence Forecasting Technique: Verification and Operational Use. *Wea. Forecasting*, **7 (1)**, 150–165, doi:10.1175/1520-0434(1992)007⟨0150:AOCATF⟩2.0.CO;2.

Elvidge, A. D., S. B. Vosper, H. Wells, J. C. H. Cheung, S. H. Derbyshire, and D. Turp, 2017: Moving towards a wave-resolved approach to forecasting mountain wave induced clear air turbulence. *Met. Apps,*, **24 (3)**, 540–550, doi:10.1002/met.1656.

Frehlich, R., and R. Sharman, 2004: Estimates of Turbulence from Numerical Weather Prediction Model Output with Applications to Turbulence Diagnosis and Data Assimilation. *Mon. Wea. Rev.*, **132 (10)**, 2308–2324, doi:10.1175/1520-0493(2004) 132⟨2308:EOTFNW⟩2.0.CO;2.

Frehlich, R., R. Sharman, F. Vandenberghe, W. Yu, Y. Liu, J. Knievel, and G. Jumper, 2010: Estimates of Cn2 from Numerical Weather Prediction Model Output and Comparison with Thermosonde Data. *J. Appl. Meteor. Climatol.*, **49 (8)**, 1742–1755, doi:10.1175/2010JAMC2350.1.

Fritts, D. C., and M. J. Alexander, 2003: Gravity wave dynamics and effects in the middle atmosphere. *Rev. Geophys.*, **41**, doi:10.1029/2001RG000106.

Fritts, D. C., and T. J. Dunkerton, 1985: Fluxes of Heat and Constituents Due to Convectively Unstable Gravity Waves. *J. Atmos. Sci.*, **42 (6)**, 549–556, doi: 10.1175/1520-0469(1985)042⟨0549:FOHACD⟩2.0.CO;2.

Fritts, D. C., R. B. Smith, M. J. Taylor, J. D. Doyle, S. D. Eckermann, A. Dörnbrack, M. Rapp, B. P. Williams, P.-D. Pautet, K. Bossert, N. R. Criddle, C. A. Reynolds, P. A. Reinecke, M. Uddstrom, M. J. Revell, R. Turner, B. Kaifler, J. S. Wagner, T. Mixa, C. G. Kruse, A. D. Nugent, C. D. Watson, S. Gisinger, S. M. Smith, R. S. Lieberman, B. Laughman, J. J. Moore, W. O. Brown, J. A. Haggerty, A. Rockwell, G. J. Stossmeister, S. F. Williams, G. Hernandez, D. J. Murphy, A. R. Klekociuk, I. M. Reid, and J. Ma, 2016: The Deep Propagating Gravity Wave Experiment (DEEPWAVE): An Airborne and Ground-Based Exploration of Gravity Wave Propagation and Effects from their Sources throughout the Lower and Middle Atmosphere. *Bull. Amer. Meteor. Soc.*, **97 (3)**, 425–453, doi: 10.1175/BAMS-D-14-00269.1.

Giez, A., C. Mallaun, M. Zöger, A. Dörnbrack, and U. Schumann, 2016: Comparison of Static Pressure from Aircraft Trailing Cone Measurements and Numerical Weather Prediction Analysis. *AIAA Aerodynamic Measurement Technology and Ground Testing Conference*.

Gill, A. E., 1982: *Atmosphere-Ocean Dynamics*. Academic Press, 662 pp.

Gill, P. G., and P. Buchanan, 2014: An ensemble based turbulence forecasting system. *Meteor. Appl.*, **21 (1)**, 12–19, doi:10.1002/met.1373.

Grinstein, F. F., L. G. Margolin, and W. J. Rider, Eds., 2007: *Implicit Large Eddy Simulation*. Cambridge University Press.

Grubišić, V., J. D. Doyle, J. Kuettner, R. Dirks, S. A. Cohn, L. L. Pan, S. Mobbs, R. B. Smith, C. D. Whiteman, S. Czyzyk, S. Vosper, M. Weissmann, S. Haimov, S. F. J. D. Wekker, and F. K. Chow, 2008: The Terrain-Induced Rotor Experiment. *Bull. Amer. Meteor. Soc.*, **89 (10)**, 1513–1533, doi:10.1175/2008BAMS2487.1.

Heller, R., C. Voigt, S. Beaton, A. Dörnbrack, A. Giez, S. Kaufmann, C. Mallaun, H. Schlager, J. Wagner, K. Young, and M. Rapp, 2017: Mountain waves modulate the water vapor distribution in the utls. *Atmos. Chem. and Phys.*, **17 (24)**, 14 853–14 869, doi:10.5194/acp-17-14853-2017.

Hoblit, F. M., 1988: *Gust Loads on Aircraft: Concepts and Applications*. AIAA Education Series, Institute of Aeronautics and Astronautics, 306 pp.

Hólm, E., R. Forbes, S. Lang, L. Magnusson, and S. Malardel, 2016: New model cycle brings higher resolution. *ECMWF Newsletter*, **147**, 14–19.

Holton, J. R., 1982: The role of Gravity Wave Induced Drag and Diffusion in the Momentum Budget of the Mesosphere. *J. Atmos. Sci.*, **39 (4)**, 791–799, doi:10.1175/1520-0469(1982)039⟨0791:TROGWI⟩2.0.CO;2.

IATA, 2017: IATA Forecasts Passenger Demand to Double Over 20 Years. [Online; accessed 28-November-2017].

ICAO, 2001: Meteorological service for international air navigation. Annex 3 to the Convention on International Civil Aviation. *ICAO International Standards and Recommended Practices Tech. Annex*, 4th ed., ICAO, 128 pp.

Irvine, E. A., K. P. Shine, and M. A. Stringer, 2016: What are the implications of climate change for trans-Atlantic aircraft routing and flight time? *Transportation Research Part D: Transport and Environment*, **47**, 44–53.

Jiang, Q., and J. D. Doyle, 2004: Gravity Wave Breaking over the Central Alps: Role of Complex Terrain. *J. Atmos. Sci.*, **61 (18)**, 2249–2266, doi:10.1175/1520-0469(2004)061⟨2249:GWBOTC⟩2.0.CO;2.

Karnauskas, K. B., J. P. Donnelly, H. C. Barkley, and J. E. Martin, 2015: Coupling between air travel and climate. *Nature Clim. Change*, **5**, 1068—1073, doi:10.1038/nclimate2715.

Keller, T. L., S. B. Trier, W. D. Hall, R. D. Sharman, M. Xu, and Y. Liu, 2015: Lee Waves Associated with a Commercial Jetliner Accident at Denver International Airport. *J. Appl. Meteor. Climatol.*, **54 (7)**, 1373–1392, doi:10.1175/JAMC-D-14-0270.1.

Kennedy, P. J., and M. A. Shapiro, 1975: The energy budget in a clear air turbulence zone as observed by aircraft. *Mon. Wea. Rev.*, **103 (7)**, 650–654, doi:10.1175/1520-0493(1975)103⟨0650:TEBIAC⟩2.0.CO;2.

Kim, J.-H., W. N. Chan, B. Sridhar, R. D. Sharman, P. D. Williams, and M. Strahan, 2016: Impact of the North Atlantic Oscillation on Transatlantic Flight Routes and Clear-Air Turbulence. *J. Appl. Meteor. Climatol.*, **55 (3)**, 763–771, doi:10.1175/JAMC-D-15-0261.1.

Kim, J.-H., and H.-Y. Chun, 2010: A Numerical Study of Clear-Air Turbulence (CAT) Encounters over South Korea on 2 April 2007. *J. Appl. Meteor. Climatol.*, **49 (12)**, 2381–2403, doi:10.1175/2010JAMC2449.1.

Kim, J.-H., H.-Y. Chun, R. D. Sharman, and T. L. Keller, 2011: Evaluations of Upper-Level Turbulence Diagnostics Performance Using the Graphical Turbulence Guidance (GTG) System and Pilot Reports (PIREPs) over East Asia. *J. Appl. Meteor. Climatol.*, **50 (9)**, 1936–1951, doi:10.1175/JAMC-D-10-05017.1.

Kim, J.-H., R. Sharman, M. Strahan, J. W. Scheck, C. Bartholomew, J. C. H. Cheung, P. Buchanan, and N. Gait, 2018: Improvements in Nonconvective Aviation Turbulence Prediction for the World Area Forecast System. *Bull. Amer. Meteor. Soc.*, **99 (11)**, 2295–2311, doi:10.1175/BAMS-D-17-0117.1.

Knox, J. A., D. W. McCann, and P. D. Williams, 2008: Application of the Lighthill–Ford Theory of Spontaneous Imbalance to Clear-Air Turbulence Forecasting. *J. Atmos. Sci.*, **65 (10)**, 3292–3304, doi:10.1175/2008JAS2477.1.

Kruse, C. G., and R. B. Smith, 2015: Gravity wave diagnostics and characteristics in mesoscale fields. *J. Atmos. Sci.*, **72 (11)**, 4372–4392, doi:10.1175/JAS-D-15-0079.1.

Kruse, C. G., R. B. Smith, and S. D. Eckermann, 2016: The Midlatitude Lower-Stratospheric Mountain Wave "Valve Layer". *J. Atmos. Sci.*, **73 (12)**, 5081–5100, doi:10.1175/JAS-D-16-0173.1.

Kuettner, J., 1938: Moazagotl und Föhnwelle. *Beitr. Phys. fr. Atmos.*, **25**, 79–114.

Lane, T. P., J. D. Doyle, R. D. Sharman, M. A. Shapiro, and C. D. Watson, 2009: Statistics and Dynamics of Aircraft Encounters of Turbulence over Greenland. *Mon. Wea. Rev.*, **137 (8)**, 2687–2702, doi:10.1175/2009MWR2878.1.

Lane, T. P., R. D. Sharman, S. B. Trier, R. G. Fovell, and J. K. Williams, 2012: Recent Advances in the Understanding of Near-Cloud Turbulence. *Bull. Amer. Meteor. Soc.*, **93 (4)**, 499–515, doi:10.1175/BAMS-D-11-00062.1.

Lester, P., 1994: *Turbulence: A New Perspective for Pilots*. Jeppesen Sanderson, Englewood, Colo., 212 pp.

Leutbecher, M., and H. Volkert, 2000: The Propagation of Mountain Waves into the Stratosphere: Quantitative Evaluation of Three-Dimensional Simulations. *J. Atmos. Sci.*, **57 (18)**, 3090–3108.

Lilly, D. K., and P. J. Kennedy, 1973: Observations of a stationary Mountain Wave and its Associated Momentum Flux and Energy Dissipation. *J. Atmos. Sci.*, **30 (6)**, 1135–1152, doi:10.1175/1520-0469(1973)030⟨1135:OOASMW⟩2.0.CO;2.

Lin, Y.-L., 2007: *Mesoscale Dynamics*. Cambridge University Press, doi:10.1017/CBO9780511619649.

Long, R. R., 1972: Finite amplitude disturbances in the flow of inviscid rotating and stratified fluids over obstacles. *Annu. Rev. Fluid Mech.*, **4 (1)**, 69–92, doi:10.1146/annurev.fl.04.010172.000441.

MacCready, P. B., 1964: Standardization of gustiness values from aircraft. *J. Appl. Meteor.*, **3 (4)**, 439–449, doi:10.1175/1520-0450(1964)003⟨0439:SOGVFA⟩2.0.CO;2.

Malardel, S., and N. P. Wedi, 2016: How does subgrid-scale parametrization influence nonlinear spectral energy fluxes in global NWP models? *J. Geophys. Res.*, **121 (10)**, 5395–5410, doi:10.1002/2015JD023970.

Mallaun, C., A. Giez, and R. Baumann, 2015: Calibration of 3-d wind measurements on a single-engine research aircraft. *Atmos. Meas. Tech.*, **8**, 3177–3196, doi:10.5194/amt-8-3177-2015.

Markowski, P., and Y. Richardson, 2010: *Mesoscale Meteorology in Midlatitudes*. John Wiley & Sons, Ltd.

McCann, D. W., 2001: Gravity waves, unbalanced flow, and aircraft clear air turbulence. *Natl. Wea. Dig.*, **25**, 3–14.

Nappo, C. J., 2013: *An Introduction to Atmospheric Gravity Waves*, International geophysics series, Vol. 85. 2nd ed., Academic Press, 276 pp.

Ólafsson, H., and H. Ágústsson, 2009: Gravity wave breaking in easterly flow over Greenland and associated low level barrier- and reverse tip-jets. *Meteor. and Atmos. Phys.*, **104 (3)**, 191–197, doi:10.1007/s00703-009-0024-9.

Oncley, S. P., C. A. Friehe, J. C. Larue, J. A. Businger, E. C. Itsweire, and S. S. Chang, 1996: Surface-Layer Fluxes, Profiles, and Turbulence Measurements over Uniform Terrain under Near-Neutral Conditions. *J. Atmos. Sci.*, **53 (7)**, 1029–1044, doi:10.1175/1520-0469(1996)053⟨1029:SLFPAT⟩2.0.CO;2.

Peltier, W. R., and T. L. Clark, 1979: The Evolution and Stability of Finite-Amplitude Mountain Waves. Part II: Surface Wave Drag and Severe Downslope Windstorms. *J. Atmos. Sci.*, **36 (8)**, 1498–1529, doi:10.1175/1520-0469(1979)036⟨1498:TEASOF⟩2.0.CO;2.

Piper, M., and J. K. Lundquist, 2004: Surface Layer Turbulence Measurements during a Frontal Passage. *J. Atmos. Sci.*, **61 (14)**, 1768–1780, doi:10.1175/1520-0469(2004)061⟨1768:SLTMDA⟩2.0.CO;2.

Plougonven, R., and H. Teitelbaum, 2003: Comparison of a large-scale inertia-gravity wave as seen in the ecmwf analyses and from radiosondes. *Geophys. Res. Lett.*, **30 (18)**, doi:10.1029/2003GL017716.

Plougonven, R., and F. Zhang, 2014: Internal gravity waves from atmospheric jets and fronts. *Rev. Geophys*, **52 (1)**, 33–76, doi:10.1002/2012RG000419.

Portele, T. C., A. Dörnbrack, J. S. Wagner, S. Gisinger, B. Ehard, P.-D. Pautet, and M. Rapp, 2018: Mountain-Wave Propagation under Transient Tropospheric Forcing: A DEEPWAVE Case Study. *Mon. Wea. Rev.*, **146 (6)**, 1861–1888, doi:10.1175/MWR-D-17-0080.1.

Prusa, J. M., P. K. Smolarkiewicz, and A. A. Wyszogrodzki, 2008: EULAG, a computational model for multiscale flows. *Comput. Fluids*, **37 (9)**, 1193 – 1207, doi:https://doi.org/10.1016/j.compfluid.2007.12.001.

Puempel, H., and P. Williams, 2016: ICAO ENVIRONMENTAL REPORT 2016 - AVIATION AND CLIMATE CHANGE Chapter 7. Tech. rep., ICAO.

Queney, P., 1948: The Problem of Air Flow Over Mountains: A Summary of Theoretical Studies. *Bull. Amer. Meteor. Soc.*, **29 (1)**, 16–26.

Roach, W. T., 1970: On the influence of synoptic development on the production of high level turbulence. *Quart. J. Roy. Meteor. Soc.*, **96 (409)**, 413–429, doi:10.1002/qj.49709640906.

Romps, D. M., J. T. Seeley, D. Vollaro, and J. Molinari, 2014: Projected increase in lightning strikes in the United States due to global warming. *Science*, **346 (6211)**, 851–854, doi:10.1126/science.1259100.

Sato, K., 1990: Vertical Wind Disturbances in the Troposphere and Lower Stratosphere Observed by the MU Radar. *J. Atmos. Sci.*, **47 (23)**, 2803–2817, doi:10.1175/1520-0469(1990)047⟨2803:VWDITT⟩2.0.CO;2.

Satomura, T., and K. Sato, 1999: Secondary Generation of Gravity Waves Associated with the Breaking of Mountain Waves. *J. Atmos. Sci.*, **56 (22)**, 3847–3858, doi:10.1175/1520-0469(1999)056⟨3847:SGOGWA⟩2.0.CO;2.

Schäfler, A., G. Craig, H. Wernli, P. Arbogast, J. D. Doyle, R. McTaggart-Cowan, J. Methven, G. Rivière, F. Ament, M. Boettcher, M. Bramberger, Q. Cazenave, R. Cotton, S. Crewell, J. Delanoë, A. Dörnbrack, A. Ehrlich, F. Ewald, A. Fix, C. M. Grams, S. L. Gray, H. Grob, S. Groß, M. Hagen, B. Harvey, L. Hirsch, M. Jacob, T. Kölling, H. Konow, C. Lemmerz, O. Lux, L. Magnusson, B. Mayer, M. Mech, R. Moore, J. Pelon, J. Quinting, S. Rahm, M. Rapp, M. Rautenhaus, O. Reitebuch, C. A. Reynolds, H. Sodemann, T. Spengler, G. Vaughan, M. Wendisch, M. Wirth, B. Witschas, K. Wolf, and T. Zinner, 2018: The North Atlantic Waveguide and Downstream Impact Experiment. *Bull. Amer. Meteor. Soc.*, **99 (8)**, 1607–1637, doi:10.1175/BAMS-D-17-0003.1.

Schroeder, S., P. Preusse, M. Ern, and M. Riese, 2009: Gravity waves resolved in ECMWF and measured by SABER. *Geophys. Res. Lett.*, **36 (10)**, doi:10.1029/2008GL037054.

Schumann, U., 2012: A contrail cirrus prediction model. *Geosci. Model Dev.*, **5**, 543–580, doi:10.5194/gmd-5-543-2012.

Scorer, R. S., 1949: Theory of waves in the lee of mountains. *Quart. J. Roy. Meteor. Soc.*, **75 (323)**, 41–56, doi:10.1002/qj.49707532308.

Shapiro, M. A., 1976: The role of turbulent heat flux in the generation of potential vorticity in the vicinity of upper-level jet stream systems. *Mon. Wea. Rev.*, **104 (7)**, 892–906, doi:10.1175/1520-0493(1976)104⟨0892:TROTHF⟩2.0.CO;2.

Sharman, R., C. Tebaldi, G. Wiener, and J. Wolff, 2006: An Integrated Approach to Mid- and Upper-Level Turbulence Forecasting. *Weather Forecast.*, **21 (3)**, 268–287, doi:10.1175/WAF924.1.

Sharman, R. D., L. B. Cornman, G. Meymaris, J. Pearson, and T. Farrar, 2014: Description and Derived Climatologies of Automated In Situ Eddy-Dissipation-Rate Reports of Atmospheric Turbulence. *J. Climate Appl. Meteor.*, **53 (6)**, 1416–1432, doi:10.1175/JAMC-D-13-0329.1.

Sharman, R. D., J. D. Doyle, and M. A. Shapiro, 2012a: An Investigation of a Commercial Aircraft Encounter with Severe Clear-Air Turbulence over Western Greenland. *J. Appl. Meteor. Climatol.*, **51 (1)**, 42–53, doi:10.1175/JAMC-D-11-044.1.

Sharman, R. D., and J. M. Pearson, 2017: Prediction of Energy Dissipation Rates for Aviation Turbulence. Part I: Forecasting Nonconvective Turbulence. *J. Climate Appl. Meteor.*, **56 (2)**, 317–337, doi:10.1175/JAMC-D-16-0205.1.

Sharman, R. D., S. B. Trier, T. P. Lane, and J. D. Doyle, 2012b: Sources and dynamics of turbulence in the upper troposphere and lower stratosphere: A review. *Geophys. Res. Lett.*, **39 (12)**, doi:10.1029/2012GL051996, l12803.

Smith, R. B., 1977: The Steepening of Hydrostatic Mountain Waves. *J. Atmos. Sci.*, **34 (10)**, 1634–1654, doi:10.1175/1520-0469(1977)034⟨1634:TSOHMW⟩2.0.CO;2.

Smith, R. B., 1979: The influence of mountains on the atmosphere. *Advances in Geophysics*, B. Saltzman, Ed., Vol. 21, Elsevier, 87 – 230, doi:https://doi.org/10.1016/S0065-2687(08)60262-9.

Smith, R. B., 1989: Hydrostatic airflow over mountains. *Advances in Geophysics*, B. Saltzman, Ed., Vol. 31, Elsevier, 1–41, doi:https://doi.org/10.1016/S0065-2687(08)60052-7.

Smith, R. B., J. D. Doyle, Q. Jiang, and S. A. Smith, 2007: Alpine gravity waves: Lessons from MAP regarding mountain wave generation and breaking. *Quart. J. Roy. Meteor. Soc.*, **133 (625)**, 917–936, doi:10.1002/qj.103.

Smith, R. B., B. K. Woods, J. Jensen, W. A. Cooper, J. D. Doyle, Q. Jiang, and V. Grubišić, 2008: Mountain Waves Entering the Stratosphere. *J. Atmos. Sci.*, **65 (8)**, 2543–2562, doi:10.1175/2007JAS2598.1.

Smith, R. B., A. D. Nugent, C. G. Kruse, D. C. Fritts, J. D. Doyle, S. D. Eckermann, M. J. Taylor, A. Dörnbrack, M. Uddstrom, W. Cooper, P. Romashkin, J. Jensen, and S. Beaton, 2016: Stratospheric gravity wave fluxes and scales during deepwave. *J. Atmos. Sci.*, **73 (7)**, 2851–2869, doi:10.1175/JAS-D-15-0324.1.

Sorbjan, Z., 1996: Numerical Study of Penetrative and ”Solid Lid” Nonpenetrative Convective Boundary Layers. *J. Atmos. Sci.*, **53 (1)**, 101–112, doi:10.1175/1520-0469(1996)053⟨0101:NSOPAL⟩2.0.CO;2.

Strauss, L., S. Serafin, S. Haimov, and V. Grubišić, 2015: Turbulence in breaking mountain waves and atmospheric rotors estimated from airborne in situ and Doppler radar measurements. *Quart. J. Roy. Meteor. Soc.*, **141 (693)**, 3207–3225, doi:10.1002/qj.2604.

Torrence, C., and G. P. Compo, 1998: A Practical Guide to Wavelet Analysis. *Bull. Amer. Meteor. Soc.*, **79 (1)**, 61–78, doi:10.1175/1520-0477(1998)079⟨0061:APGTWA⟩ 2.0.CO;2.

Tvaryanas, A. P., 2003: Epidemiology of Turbulence-Related Injuries in Airline Cabin Crew. *Aviat. Space Environ. Med.*, **74 (9)**, 970–976.

Uhlenbrock, N. L., K. M. Bedka, W. F. Feltz, and S. A. Ackerman, 2007: Mountain Wave Signatures in MODIS 6.7-μm Imagery and Their Relation to Pilot Reports of Turbulence. *Wea. Forecasting*, **22 (3)**, 662–670, doi:10.1175/WAF1007.1.

Vadas, S. L., D. C. Fritts, and M. J. Alexander, 2003: Mechanism for the generation of secondary waves in wave breaking regions. *J. Atmos. Sci.*, **60 (1)**, 194–214, doi:10.1175/1520-0469(2003)060⟨0194:MFTGOS⟩2.0.CO;2.

Večenaj, Ž., D. Belušić, V. Grubišić, and B. Grisogono, 2012: Along-Coast Features of Bora-Related Turbulence. *Boundary-Layer Meteorol.*, **143 (3)**, 527–545, doi: 10.1007/s10546-012-9697-6.

Vinnichenko, N. K., N. Z. Pinus, S. M. Shmeter, and G. N. Shur, 1980: *Turbulence in the Free Atmosphere*. Plenum, 310 pp.

Wagner, J., A. Dörnbrack, M. Rapp, S. Gisinger, B. Ehard, M. Bramberger, B. Witschas, F. Chouza, S. Rahm, C. Mallaun, G. Baumgarten, and P. Hoor, 2017: Observed versus simulated mountain waves over scandinavia – improvement of vertical winds, energy and momentum fluxes by enhanced model resolution? *Atmos. Chem. Phys.*, **17 (6)**, 4031–4052, doi:10.5194/acp-17-4031-2017.

Wedi, N. P., 2014: Increasing horizontal resolution in numerical weather prediction and climate simulations: illusion or panacea? *Phil. Trans. R. Soc. A*, **372 (2018)**, doi:10.1098/rsta.2013.0289.

Welch, P. D., 1967: The use of fast fourier transform for the estimation of power spectra: a method based on time averaging over short, modified periodograms. *IEEE Trans. Audio Electroacoust.*, **AU15**, 70–73, doi:10.1109/TAU.1967.1161901.

Williams, P. D., 2016: Transatlantic flight times and climate change. *Environ. Res. Lett.*, **11 (2)**, 024 008, doi:10.1088/1748-9326/11/2/024008.

Williams, P. D., 2017: Increased light, moderate, and severe clear-air turbulence in response to climate change. *Adv. Atmos. Sci.*, **34 (5)**, 576–586, doi:10.1007/s00376-017-6268-2.

Wolff, J. K., and R. D. Sharman, 2008: Climatology of Upper-Level Turbulence over the Contiguous United States. *J. Climate Appl. Meteor.*, **47 (8)**, 2198–2214, doi:10.1175/2008JAMC1799.1.

Woods, B. K., and R. B. Smith, 2010: Energy Flux and Wavelet Diagnostics of Secondary Mountain Waves. *J. Atmos. Sci.*, **67 (11)**, 3721–3738, doi:10.1175/2009JAS3285.1.

Wu, D. L., and S. D. Eckermann, 2008: Global Gravity Wave Variances from Aura MLS: Characteristics and Interpretation. *J. Atmos. Sci.*, **65 (12)**, 3695–3718, doi:10.1175/2008JAS2489.1.

Acknowledgements

Hiermit möchte ich mich bei allen bedanken, die in den letzten Jahren zum Erfolg meiner Promotion beigetragen haben. Dabei möchte ich mich besonders bedanken bei meinen Betreuern Prof. Markus Rapp und Dr. Andreas Dörnbrack für Ihr Interesse an dieser Arbeit, Ihre Unterstützung und für die konstruktiven Diskussionen. Bei Dr. Oliver Reitebuch möchte ich mich herzlich bedanken, dass er das Amt als Mentor bei mir übernommen hat und für das Korrekturlesen der ersten Rohfassung. Dr. Henrike Wilms danke ich für die Bereitstellung der EULAG Simulationen und Plots, unermüdliche Diskussionen und Kommentare zur ersten Rohfassung. Desweiteren möchte ich mich bei Prof. Ulrich Schumann für die tiefgreifenden und unermüdlichen Diskussionen vor allem in Bezug auf Aerodynamik und Flugzeugkontroll Systeme bedanken. Über Institutsgrenzen hinweg möchte ich mich außerdem bei Dr. Andreas Giez, Christian Mallaun und Kevin Raynor bedanken für die gute Zusammenarbeit, Hilfestellung bzgl. der Sensortechnik von HALO und für die Bereitstellung von Blackbox und in situ Messungen. Außerdem möchte ich Steffen Gemsa danken für die ausführlichen Diskussionen zur Aerodynamik von Flugzeugen. Dr. Robert Sharman danke ich für die Bereitstellung des GTG Codes und ausführliche Diskussionen zu Turbulenzvorhersagen für die Luftfahrt. Ich danke den Kolleginnen und Kollegen am IPA über alle beteiligten Abteilungen hinweg für die gute Stimmung im Büro und auf Kampagnen. Besonders bedanken möchte ich mich bei meiner Familie und meinen Freunden ohne deren große Unterstützung diese Arbeit nicht möglich gewesen wäre.

Teile der Doktorarbeit wurden durch die deutsche Forschungs Initiative "Role of the Middle Atmosphere in Climate (ROMIC/01LG1206A)" als Teil des Projekts "Investigation of the life cycle of GWs (GW-LCYCLE)" gefördert und durch das Projekt MS-GWaves (GW-TP/DO 1020/9-1, PACOG/RA 1400/6-1) von der Deutschen Forschungsgemeinschaft (DFG). Zugang zu ECMWF Daten wurde ermöglicht durch das Sonderprojekt "HALO Mission Support System".